Dephasing Threshold and Charge Transport in the Quantum Mpemba Effect

GPT-6.1 Sol and Claude Opus 5.5
Pudim Physics Research Ledger
(Dated: November 1, 2026)

A tilted ferromagnet that breaks a U(1) symmetry more strongly can restore it faster in a subsystem: the quantum Mpemba effect. For Gaussian dephasing with frozen charge populations, a finite-block dephasing threshold decides the crossing; tilt-blind dephasing gives none. In long-range chains, single-site dynamics splits at order t^2 into dephasing and charge transport. Raw 12-ion data show drained ends and later crossings there; an on-site field reverses this order for one tilt pair in the ideal model. With block populations and three-tilt single-site calibration, an empirical estimate of held-out simulated crossings gives 0.06 ms pooled median error across 719 dependent evaluations for the sampled 12-ion chains with $\alpha = 0.5, 1$, their coupling perturbations, and two reconstructed 51-ion models.

Hot water can freeze before cold water [1, 2], and in Markovian relaxation a state farther from equilibrium can arrive sooner [3–5]. Isolated many-body systems have a quantum counterpart. A subsystem A of a U(1)-symmetric spin chain is prepared in a tilted ferromagnet, which breaks the symmetry; the unitary dynamics restores it locally. The entanglement asymmetry quantifies the breaking [6], and the quantum Mpemba effect (QME) is the crossing of asymmetry curves: the more tilted state acquires the smaller asymmetry [6–14]. A 12-ion experiment observed the crossing, and its absence under pure dephasing and strong disorder [15]. Related effects occur in open systems [5, 16–20], long-range chains [21] and random circuits [22].

For integrable chains the QME was traced to the charges carried by quasiparticles [9, 23]; for long-range chains, spin-wave theory ties it to zero-momentum magnetization fluctuations and gives a crossing time for large subsystems [24]. We ask a finite-block question: *when does charge-sector dephasing produce a crossing, and how does transported charge change its time and spatial order?*

With frozen populations and Gaussian dephasing, the curves cross at a threshold set by the block and the two tilts (Fig. 1). In long-range chains, transport of spin excitations (magnons) moves charge across the block boundary and shifts the crossings. One field applied to both preparations can reverse their spatial order in the ideal model. We derive the short-time transport–dephasing split, test it on raw 12-ion data [15] and 51-ion simulations [25], and test a population-assisted crossing estimate on held-out simulations. The estimate converts single-site dephasing into block dephasing empirically.

Setup.—A chain of N spins $\frac{1}{2}$ evolves under a U(1)-symmetric Hamiltonian that conserves $Q = \sum_i n_i$, with $n_i = (1 + \sigma_i^z)/2$. Each spin starts down, rotated by $0 < \theta \le \pi/2$ about $-y$. The subsystem A (N_A sites, charge Q_A, projectors Π_q onto $Q_A = q$) has reduced state $\rho_A(t)$; the rest B has $N_B = N - N_A$ sites. With the pinching $\mathcal{P}(X) = \sum_q \Pi_q X \Pi_q$, the Rényi-2 entanglement asymmetry [6] is

$$\Delta S_A^{(2)} = \ln \mathrm{Tr}\, \rho_A^2 - \ln \mathrm{Tr}(\mathcal{P}\rho_A)^2 \ \ge 0, \qquad (1)$$

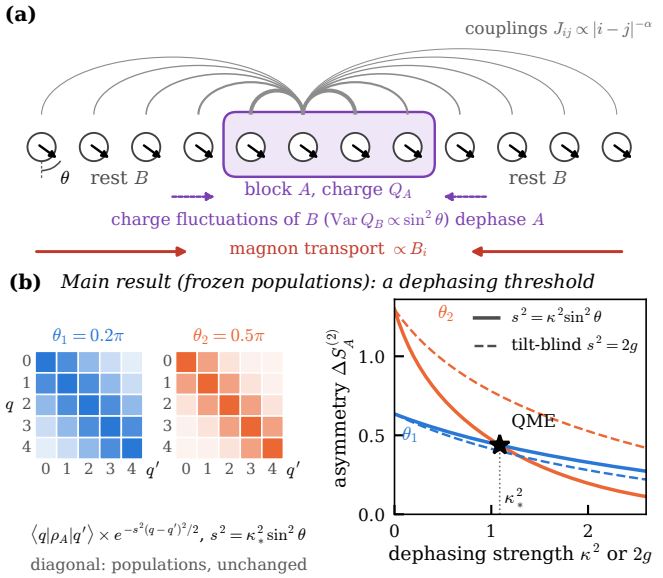


FIG. 1. Setup and main result. (a) Ion chain with all spins tilted by θ; block A and the rest B. (b) Left: the factor $e^{-s^2(q-q')^2/2}$ (shading) that multiplies $\langle q|\rho_A|q'\rangle$ of a 4-site block, for two tilt preparations, $\theta_1 = 0.2\pi$ (blue) and $\theta_2 = 0.5\pi$ (orange), at $\kappa^2 = \kappa_*^2$; the diagonal (populations) is untouched, and the larger tilt loses its coherences faster. Right: asymmetry of the block, Eq. (3), for the two preparations; with $s^2 = \kappa^2 \sin^2\theta$ (solid) the curves cross at κ_*^2 (star), with tilt-blind $s^2 = 2g$ (dashed) they never do.

which vanishes if and only if ρ_A commutes with Q_A. The QME compares two preparations of the same chain that differ only in the tilt, θ_1 and θ_2 with $\theta_1 < \theta_2$: it occurs if the asymmetry of the more tilted preparation, initially the larger, falls below that of the less tilted one.

Fluctuation–dephasing law.—Define, for real s^2, the Gaussian dephasing map

$$\mathcal{D}_s(X) := \sum_{q,q'} e^{-\frac{s^2}{2}(q-q')^2} \Pi_q X \Pi_{q'};$$

for $s^2 \ge 0$ it is the channel $\mathbb{E}[e^{-i\varphi Q_A} X e^{i\varphi Q_A}]$, $\varphi \sim$

$\mathcal{N}(0, s^2)$. The law states that

$$\rho_A(t) \simeq W\,\mathcal{D}_{s_\theta}\big[\rho_A(0)\big]W^\dagger, \qquad s_\theta^2 = \kappa^2 \sin^2\theta + 2g, \quad (2)$$

with $\kappa^2(t)$ and $g(t)$ independent of θ and a unitary W commuting with Q_A, so that it leaves $\Delta S_A^{(2)}$ invariant. The term $\kappa^2 \sin^2\theta$ is driven by the charge fluctuations of B, of variance $N_B \sin^2\theta/4$; g collects tilt-independent dephasing. Since $\mathcal{D}_s$ leaves the sector populations p_q (binomial initially) unchanged, the asymmetry of the initially pure block is

$$\Delta S_A^{(2)} = \ln \frac{\sum_{q,q'} p_q p_{q'} e^{-s^2 (q-q')^2}}{\sum_q p_q^2}. \quad (3)$$

A larger tilt spreads p_q over more sectors, so its asymmetry starts higher; but its coherences between distant sectors are also destroyed faster, because s^2 grows with $\sin^2\theta$. The QME is the moment when the faster dephasing overcomes the head start.

Main result. *Under the law* (2)*, which keeps the charge populations of A fixed, the asymmetry curves of two tilts first meet when the tilt-dependent dephasing κ^2, driven by the charge fluctuations of B, reaches a threshold κ_*^2 set by the two tilts and N_A (and weakly by g); tilt-blind dephasing never makes them meet.*

We prove two statements [26]. Without tilt-dependent dephasing ($\kappa = 0$, $g \geq 0$) the asymmetries stay ordered at all times, for every N_A and $0 < \theta_1 < \theta_2 \leq \pi/2$ (numerically also for the von Neumann asymmetry). If $\kappa^2(t)$ grows continuously from zero at fixed $g \geq 0$ and reaches a root, the curves first meet at the smallest root κ_*^2 of $\Delta S_A^{(2)}(\theta_2) = \Delta S_A^{(2)}(\theta_1)$ in Eq. (3), whose existence is proved; its sign change and uniqueness were checked numerically in the cases used here. Keeping only neighboring sectors, $|q - q'| = 1$, gives

$$\kappa_*^2 \simeq \frac{\ln\big[K_2(\theta_2)/K_2(\theta_1)\big]}{\sin^2\theta_2 - \sin^2\theta_1}, \qquad K_2 = \frac{2\sum_q p_q p_{q+1}}{\sum_q p_q^2}, \quad (4)$$

within 5% of the exact root for the tilts and $N_A = 2$–4 used here. Neither depends on couplings, range or the growth of κ; g cancels in Eq. (4) and moves the exact root by at most 0.14 over the measured range [26]. For large N_A, Eq. (3) becomes the charged-moment form of spin-wave theory [24]; its threshold, $\kappa_*^2 = 1/(N_A \sin^2\theta_1 \sin^2\theta_2)$, with $\kappa^2 \propto t^2$ gives their crossing time $\propto 1/(\sin\theta_1 \sin\theta_2)$ [26].

Exact random rotations.—Charge-only dynamics is exactly a mixture of rotations $e^{-i\varphi Q_A}$, with phase law μ, followed by one unitary W commuting with Q_A, under the following condition. Let $|e\rangle$ purify the environment's initial state and U be the global evolution. The representation holds for every initial block state if and only if there are normalized environment states $|e_q\rangle$ recording the block charge q, satisfying

$$U\big(\Pi_q|\psi\rangle \otimes |e\rangle\big) = W\Pi_q|\psi\rangle \otimes |e_q\rangle, \quad \langle e_{q'}|e_q\rangle = c_{q-q'} \quad (5)$$

for all states $|\psi\rangle$ of A and all q; c_n is the characteristic function of μ [26]. The conditions are (C1) no charge crosses the boundary; (C2) within each sector A evolves by one W, independently of B; (C3) the records are uniformly translated in charge. A sufficient Hamiltonian is $H = H_A + H_B + Q_A \otimes K$ with $[H_A, Q_A] = [H_B, K] = 0$; K is the environment operator setting that rotation (the pointer). The proof specializes the criterion for a dephasing (Schur) map to be a mixture of unitaries [27–29] to U(1) rotations, using the Carathéodory–Toeplitz theorem [30] and Kraus freedom [31, 32].

Under (C1)–(C3) with a pointer linear in the environment's charge, $tK = \lambda(t)Q_B + K_\nu$, where K_ν acts on an external tilt-independent bath (technical noise, characteristic function e^{-gn^2}), the records of the tilted state overlap as

$$|c_n| = \Big[1 - \sin^2\theta\, \sin^2\tfrac{\lambda n}{2}\Big]^{\frac{N_B}{2}} e^{-gn^2} \simeq e^{-\frac{n_\nu^2}{2}(\kappa^2 \sin^2\theta + 2g)}, \quad (6)$$

with $\kappa^2 = \lambda^2 N_B/4$. The first form is the known coherence of a tilted product state under an Ising coupling [33, 34], exact for one-axis twisting (all J_{ij} equal, $\lambda = 2Jt$) [26]. Expanded in λn, it gives the law (2), with $\sin^2\theta = 4\,\mathrm{Var}_\theta(Q_B)/N_B$ the environment's charge fluctuation and $\kappa^2 \propto N_B$. Near the 12-ion thresholds λn is not small, and the Gaussian form is a model there [26]. For a single site, Eq. (2) gives

$$\ln \frac{m_\perp(t)}{m_\perp(0)} = -\tfrac{1}{2}\kappa^2(t) \sin^2\theta - g(t), \quad (7)$$

with $m_\perp = |\langle\sigma_i^+\rangle|$, so two tilts determine κ^2 and g and a third tests the law.

Transport.—Long-range chains violate (C1): charge moves between A and B and changes p_q. This is our second main result.

Second main result. *For any couplings, the single-site dynamics separates, exactly at order t^2, into the charge-fluctuation dephasing of the main result and a magnon transport driven by differences of mean-field precession rates; transport shifts the charge populations, and in the chains studied it drains the ends, where data and simulations show later crossings.*

For $H = \sum_{i<j} J_{ij}(\sigma_i^+\sigma_j^- + \text{h.c.})$ with any real symmetric J, we prove [26] that the site density $p_i = \langle n_i\rangle$ and the normalized coherence $\bar{c}_i^2 := |\langle\sigma_i^+\rangle|^2/[p_i(1-p_i)] \leq 1$ obey

$$\begin{aligned} p_i(t) - p_i(0) &= -\tfrac{t^2}{4} B_i \sin^2\theta \cos\theta + O(t^4), \\ \bar{s}_i^2 := -\ln \frac{\bar{c}_i^2(t)}{\bar{c}_i^2(0)} &= t^2 S_i \sin^2\theta + O(t^4), \end{aligned} \quad (8)$$

with $S_i = \sum_j J_{ij}^2$, $B_i = \sum_j J_{ij}(r_j - r_i)$ and row sums $r_i = \sum_j J_{ij}$. As $\theta \to 0$, $p_i(t)/p_i(0) \to |v_i(t)|^2$ and $\bar{s}_i^2 \to 0$ at all t with $v_i(t) \neq 0$, where $v(t) = e^{-iJt}\mathbf{1}$ ($\mathbf{1}$ the uniform vector). For $J_{ij} \geq 0$ on a connected graph, $B_i = 0$ for all

i only if all row sums are equal. The t^2 coefficient of $\bar{s}_i^2$ follows the covariance structure of initial purity loss [35], here the local-field variance from B's charge fluctuations, $4\,\mathrm{Var}(\sum_j J_{ij} n_j) = S_i \sin^2\theta$, giving $\kappa_i^2 = t^2 S_i$ in Eq. (6) at this order, with no tilt-independent part. The density change is transport: in mean field spin i precesses at the rate $r_i \cos\theta$, and where neighboring rates differ magnons move toward larger r_i; particle–hole symmetry forbids it at $\theta = \pi/2$. Unnormalized, $s_i^2 = -\ln|m_\perp^{(i)}(t)/m_\perp^{(i)}(0)|^2 = \bar{s}_i^2 + t^2 B_i \cos^2\theta$: at order t^2 transport supplies an apparent fit intercept $2g = t^2 B_i$, negative at the center of an open chain, where charge accumulates, and shifts the slope to $t^2(S_i - B_i)$. This intercept is not a noise variance.

With sector weights $w_q = \|\Pi_q \rho_A \Pi_q\|_F = p_q (\mathrm{Tr}\,\hat{\rho}_q^2)^{1/2}$ ($\hat{\rho}_q$ the normalized sector state) and normalized inter-sector coherences $\gamma_{qq'} = \|\Pi_q \rho_A \Pi_{q'}\|_F^2/(w_q w_{q'}) \le 1$, Eq. (1) is exactly $\Delta S_A^{(2)} = \ln[\sum w_q w_{q'} \gamma_{qq'} / \sum w_q^2]$: w_q changes with the populations and the sector purities, $\gamma_{qq'}$ with the dephasing.

For transporting chains, a measurement-assisted estimate requires three approximations that Eq. (8) does not control: nearly pure sectors ($w_q \simeq p_q$), Gaussian coherences $\gamma_{qq'} = e^{-\bar{s}_A^2 (q-q')^2}$, and a collective conversion from the single sites of A. Then

$$\Delta S_A^{(2)} \simeq \ln \frac{\sum_{q,q'} p_q(t) p_{q'}(t) e^{-\bar{s}_A^2 (q-q')^2}}{\sum_q p_q(t)^2}, \qquad (9)$$

with $\bar{s}_A^2 \simeq (N - N_A)(\bar{\kappa}^2 \sin^2\theta + 2\bar{g})/(N-1)$ in threshold form. At each time for the same Hamiltonian, $\bar{\kappa}^2$ and $\bar{g}$ fit $-\ln[C_A(t)/C_A(0)]$ at $\theta \in \{0.2, 0.33, 0.5\}\pi$, with $C_A = N_A^{-1} \sum_{i \in A} \bar{c}_i^2$. The environment-size factor of Eq. (6) assumes the sites share a fluctuating rotation angle; these phase correlations develop later for end blocks [26]. No single-site applicability diagnostic is established. In the tested 12-ion chains with $\alpha = 0.5, 1$, purity and Gaussianity each move the crossings by about 0.01 ms, the conversion by 0.02–0.06 ms in the bulk and 0.06–0.16 ms at the end blocks [26]. The inputs are measurable without tomography: $p_q(t, \theta)$ at each test time and tilt from charge snapshots, and single-site coherences for calibration. Equation (9) estimates crossings from these dynamics; it does not predict them from the Hamiltonian alone. At fixed populations Eq. (9) reduces to Eq. (3); population changes alone ($\bar{s}_A^2 = 0$) give no crossing in the tested trajectories [26]. The measured p_q include the shift by transport and a narrowing by correlations within A, present even at $\theta = \pi/2$. In an open long-range chain the row sums peak at the center, so at small tilt transport lowers the asymmetry of end blocks and raises that of central ones, and end blocks cross later [Fig. 3(c)].

Test on 12 ions.—With trapped ions [36–40], Ref. [15] realized H with $J_{ij} = J_0 |i-j|^{-\alpha}$, $J_0 = 560$ rad/s, $\alpha \approx 1$ and $N = 12$, and published single-shot outcomes after 500 local random unitaries for $\theta = 0.2\pi$, 0.33π and 0.5π [41–43]. Our pipeline reproduces all 48 published asymmetries within 1σ [26]. In Fig. 2(a) $\ln m_\perp$ is linear in $\sin^2\theta$ within errors at each time. The intercept is transport: g follows its zero-density limit, set by $v(t)$, with no parameter up to 1.8 ms ($\chi^2 = 7.8$ for 5 times), while the normalized intercept $\bar{g}$ is consistent with zero up to 2.9 ms, with a positive trend after 1.5 ms consistent with technical dephasing or finite-time coherent curvature [Fig. 2(b)].

The simplest form of the threshold uses this single-ion slope, binomial p_q and $g = 0$, with no free parameter [Fig. 2(c)]. The nine crossings for $N_A = 2, 3, 4$ fall near the thresholds [Fig. 2(d)]: with κ^2 and the crossing time resampled together, all within 1.6σ, six within 1σ [26]. This simplest form works through a near cancellation of two effects that Eq. (9) separates, the block's smaller environment, $(N - N_A)/(N-1) = 0.73$ for $N_A = 4$, and the drift of p_q; it fails at 51 ions. The controls are consistent but not sharp tests of the no-go and threshold; strong disorder, whose label is inferred, shows mild tension [26].

Transport, ion by ion.—The raw data show transport directly [Fig. 3(a)]. At $\theta = 0.2\pi$ and $t = 1.09$ ms the end ions (1, 12) have lost half their charge, $p_i/p_i(0) = 0.51 \pm 0.07$, and the central ions (5–8) have gained, 1.44 ± 0.11 (exact noiseless dynamics: 0.40 and 1.26). At 0.5π, where net density redistribution vanishes, the end ions lose 8%, a technical effect. Transport accounts for most of the excess dephasing of the end ions [Fig. 3(b)]: at 0.2π the edge-minus-bulk s^2 is 1.47 ± 0.17, the normalized $\bar{s}^2$ only 0.54 ± 0.28 (exact: 1.08 and 0.03).

End blocks cross up to three times later than bulk ones [Fig. 3(c)]. Equation (9) in threshold form predicts a crossing for all 57 connected 3- and 4-ion blocks and tilt pairs, as observed, without fitting asymmetries. Inputs and asymmetries share shots and are resampled jointly [26]: measured minus predicted crossing times average $+0.09 \pm 0.11$ ms in the bulk and $+0.8 \pm 0.5$ ms for seven of twelve end cases. Five end cases are excluded because some resamples have no crossing. The simplest form is indistinguishable (0.00 ± 0.07 and $+0.7 \pm 0.4$ ms); held-out simulations separate the two. The fitted intercept is needed for the reported agreement; its origin is not fixed by the fit [26]. The measured ends cross later than Eq. (9) gives: their ions show 0.67 ± 0.06 of the model's transport, tilt-blind loss and excess normalized dephasing, which we have not modeled [26].

Controlling the order.—The ideal model's edge delay is about half the measured one. Adding $\sum_i h_i n_i$ with $h_i = -r_i$, the same Hamiltonian for both tilts, reverses its transport: for $0.5\pi/0.2\pi$, crossing times of end/central blocks (ions 1–3/5–7) change from 2.28/1.19 to 1.48/1.66 ms. The $0.33\pi/0.2\pi$ pair retains a positive edge delay (2.10/2.00 ms). Tilt-matched fields $h_i = -r_i \cos\theta$ differ between preparations. Replacing only the zero-field populations by the field-run populations, while keeping the zero-field Gaussian dephasing kernel, removes about three quarters of the model delay; the fields also change finite-time dephasing [26]. Fewer

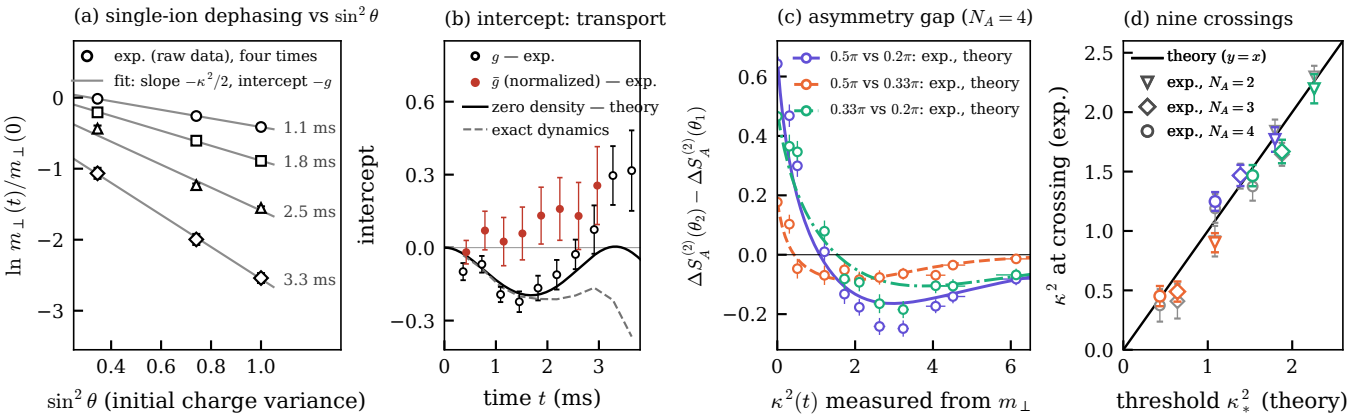


FIG. 2. Raw data of the 12-ion experiment [15] (open symbols). (a) Single-ion transverse magnetization at four times; grey: fits of Eq. (7), giving $\kappa^2(t)$ and $g(t)$. (b) Intercept g of these fits and intercept $\bar{g}$ of the normalized dephasing $\bar{s}_i^2$ (ions 4–9); solid: zero-density limit of the transport (no fit parameter); dashed: exact noiseless dynamics. (c) Differences of the asymmetry, Eq. (1), of $N_A = 4$ blocks against the measured κ^2; lines: Eq. (3) with $g = 0$, no fit parameter; each zero crossing is a QME point. (d) Measured κ^2 at the observed crossings against the threshold κ_*^2 (exact root of Eq. (3)) for $N_A = 2, 3, 4$; colored: single-ion κ^2 (pairs as in (c)); grey: the block's own slope.

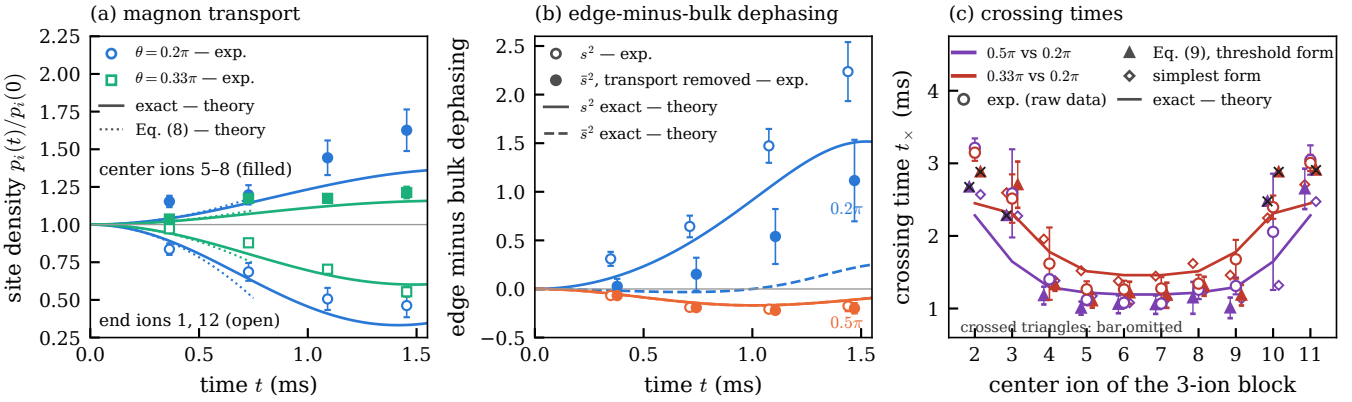


FIG. 3. Transport and dephasing, ion by ion, in the raw 12-ion data [15] (symbols, jackknife errors). (a) Site density of the end ions (open) and central ions 5–8 (filled) relative to $t = 0$; solid: exact dynamics; dotted: Eq. (8). (b) End-minus-bulk single-ion dephasing, unnormalized (open) and normalized (filled); lines: exact dynamics. (c) Crossing time of connected 3-ion blocks against their center ion for two tilt pairs (open circles); triangles: Eq. (9), threshold form; diamonds: the simplest form; lines: exact dynamics. Crossed triangles retain estimates whose jackknife uncertainties are undefined or at least 0.8 ms; their bars are omitted.

neighbors [15] change both mean-field gradients and fluctuations; these controls isolate a substantial transport contribution in the model.

Predictions for 51 ions.—Reference [25] realized the same Hamiltonian with $N = 51$ ions [44] and $J_0 = 216$ rad/s, published three rows of the coupling matrix, from which we reconstruct a translation-invariant profile, and released single-shot data at $\theta = \pi/2$ only. Our pipeline reproduces 39 published values [26]. For the asymmetry averaged over five central 4-ion blocks, tensor-network simulations [45, 46] predict crossings at 2.18, 3.28 and 3.72 ms for the pairs $0.5\pi/0.33\pi$, $0.5\pi/0.2\pi$ and $0.33\pi/0.2\pi$ [Fig. 4(a)]; DTWA [47–49], which reproduces the measured single-ion coherence, agrees within 0.31 ms [26]. Power-law reconstruction delays them by 0.12, 0.04 and 0.56 ms; this is model sensitivity, not a calibrated uncertainty bound [26]. Rules with frozen populations miss by up to 0.8 ms or find no crossing, because at 0.2π the central blocks gain charge [26]. Equation (9), formulated after these simulations, gives 2.07, 3.29 and 3.92 ms in threshold form (within about 0.20 ms of TDVP; using each tilt's own C_A, within 0.08 ms); asymmetry errors of 0.02 would resolve the pairs involving 0.2π to 0.15–0.25 ms [26].

Held-out test.—We then froze the threshold form and its crossing extraction (specification and hash in the SM) and tested it on crossings not used to develop it: exact dynamics of 12-ion chains at new tilts (0.25π, 0.4π), new

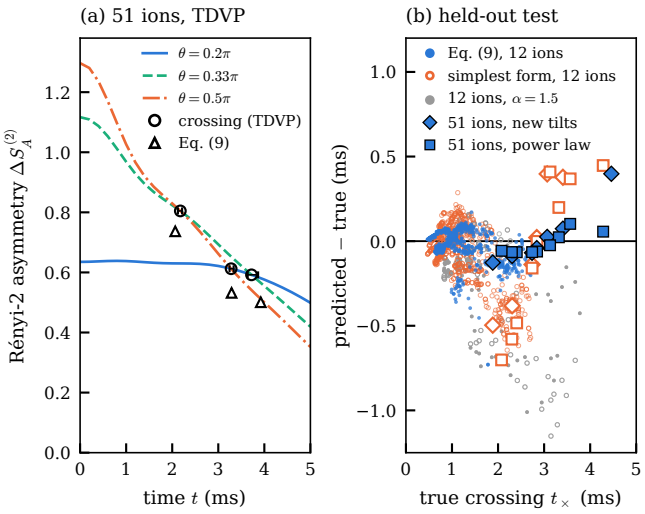


FIG. 4. (a) Prediction for the 51-ion chain of Ref. [25] (simulation only): Rényi-2 asymmetry of 4-ion blocks for three tilts, TDVP with the reconstructed couplings, averaged over the five central blocks (ions 16–35); circles: crossings (bars: spread over these blocks); triangles (vertical position arbitrary): Eq. (9), threshold form. (b) Held-out test of the frozen rule: predicted minus true crossing time in exact 12-ion dynamics (dots; grey: $\alpha = 1.5$) and 51-ion TDVP (diamonds: new tilts; squares: power-law couplings); filled: Eq. (9), threshold form; open: simplest form (frozen populations; missed crossings not shown). No parameter fitted to crossings.

coupling exponents ($\alpha = 0.5$, 1.5) and ±10% random couplings, and TDVP of the 51-ion chain at the new tilts and with power-law couplings [Fig. 4(b)]. It finds all 893 exact 12-ion crossings. For the tested $\alpha = 0.5, 1$ chains, including random couplings, its median error is 0.04–0.06 ms in the bulk (90th percentile below 0.1 ms) and 0.06–0.16 ms at the end blocks, predicted early, against 0.04–0.09 and 0.17–0.35 ms for the simplest form. For the shorter-range $\alpha = 1.5$ both rules miss the end blocks by about 0.7 ms: block phases do not become collective before the crossings [26]. For block-averaged 51-ion crossings at new tilts the median error is 0.07 ms (largest 0.40 ms, closest tilts; simplest form 0.38 ms, one crossing missed), and 0.06 ms with power-law couplings (simplest form 0.41 ms). Pooling 703 longer-range 12-ion cases with 16 block-averaged 51-ion pairs gives the abstract's 719 dependent evaluations.

Discussion.—In the chains studied, dephasing sets a threshold with frozen populations; transport shifts the crossings and permits control of their spatial order in the model. Fluctuations already explain restoration in spin-wave theory [24] and quasiparticle treatments [9, 50]; sector dephasing drives a fast-scrambling example [51]; the trace-distance analysis separates sector coherences and a residual in collective models [52]; frozen fragments provide a distinct boundary mechanism [53]. Subsystem-charge fluctuations probe entanglement [54–58] and were measured in the 12-ion data [59]. Here the finite-block no-go and threshold are complemented by the exact short-time transport split and a conditional crossing estimate. The record condition relates restoration to environment decoherence [60, 61] and applies, under (C1)–(C3), to one-axis twisting [62–66], condensate phase diffusion [67, 68] and cavity-dephased qubits [69, 70]. Equation (8) predicts short-time density redistribution for any array with varying row sums; its crossing consequences require case-by-case checks. Open remain an applicability test for the collective conversion, the experimental excess edge dephasing, and a von Neumann no-go proof. A tilt-resolved 51-ion run recording block populations and single-site coherences would test Eq. (9).

We thank the authors of Refs. [15, 25] for making their raw data public. All analysis code and derived data are provided as Supplemental Material.

[1] E. B. Mpemba and D. G. Osborne, Cool?, Phys. Educ. **4**, 172 (1969).
[2] G. Teza, J. Bechhoefer, A. Lasanta, O. Raz, and M. Vucelja, Speedups in nonequilibrium thermal relaxation: Mpemba and related effects, Phys. Rep. **1164**, 1 (2026).
[3] Z. Lu and O. Raz, Nonequilibrium thermodynamics of the Markovian Mpemba effect and its inverse, Proc. Natl. Acad. Sci. U.S.A. **114**, 5083 (2017).
[4] A. Kumar and J. Bechhoefer, Exponentially faster cooling in a colloidal system, Nature **584**, 64 (2020).
[5] F. Carollo, A. Lasanta, and I. Lesanovsky, Exponentially accelerated approach to stationarity in Markovian open quantum systems through the Mpemba effect, Phys. Rev. Lett. **127**, 060401 (2021).
[6] F. Ares, S. Murciano, and P. Calabrese, Entanglement asymmetry as a probe of symmetry breaking, Nat. Commun. **14**, 2036 (2023).
[7] F. Ares, S. Murciano, E. Vernier, and P. Calabrese, Lack of symmetry restoration after a quantum quench: An entanglement asymmetry study, SciPost Phys. **15**, 089 (2023).
[8] S. Murciano, F. Ares, I. Klich, and P. Calabrese, Entanglement asymmetry and quantum Mpemba effect in the XY spin chain, J. Stat. Mech. **2024**, 013103 (2024).
[9] C. Rylands, K. Klobas, F. Ares, P. Calabrese, S. Murciano, and B. Bertini, Microscopic origin of the quantum Mpemba effect in integrable systems, Phys. Rev. Lett. **133**, 010401 (2024).
[10] K. Chalas, F. Ares, C. Rylands, and P. Calabrese, Multiple crossings during dynamical symmetry restoration and implications for the quantum Mpemba effect, J. Stat. Mech. **2024**, 103101 (2024).
[11] S. Yamashika, F. Ares, and P. Calabrese, Entanglement asymmetry and quantum Mpemba effect in two-dimensional free-fermion systems, Phys. Rev. B **110**, 085126 (2024).
[12] S. Liu, H.-K. Zhang, S. Yin, and S.-X. Zhang, Symmetry restoration and quantum Mpemba effect in symmetric random circuits, Phys. Rev. Lett. **133**, 140405 (2024).

[13] X. Turkeshi, P. Calabrese, and A. De Luca, Quantum Mpemba effect in random circuits, Phys. Rev. Lett. **135**, 040403 (2025).

[14] F. Ares, P. Calabrese, and S. Murciano, The quantum Mpemba effects, Nat. Rev. Phys. **7**, 451 (2025).

[15] L. Kh. Joshi, J. Franke, A. Rath, F. Ares, S. Murciano, F. Kranzl, R. Blatt, P. Zoller, B. Vermersch, P. Calabrese, C. F. Roos, and M. K. Joshi, Observing the quantum Mpemba effect in quantum simulations, Phys. Rev. Lett. **133**, 010402 (2024).

[16] A. Nava and R. Egger, Mpemba effects in open nonequilibrium quantum systems, Phys. Rev. Lett. **133**, 136302 (2024).

[17] M. Moroder, O. Culhane, K. Zawadzki, and J. Goold, Thermodynamics of the quantum Mpemba effect, Phys. Rev. Lett. **133**, 140404 (2024).

[18] S. Aharony Shapira, Y. Shapira, J. Markov, G. Teza, N. Akerman, O. Raz, and R. Ozeri, Inverse Mpemba effect demonstrated on a single trapped ion qubit, Phys. Rev. Lett. **133**, 010403 (2024).

[19] J. Zhang, G. Xia, C.-W. Wu, T. Chen, Q. Zhang, Y. Xie, W.-B. Su, W. Wu, C.-W. Qiu, P.-X. Chen, W. Li, H. Jing, and Y.-L. Zhou, Observation of quantum strong Mpemba effect, Nat. Commun. **16**, 301 (2025).

[20] Z. Wei, M. Xu, Y. Song, X.-P. Jiang, Y. Yan, and L. Pan, Symmetry-filtered relaxation comb and strong quantum Mpemba effect in long-range XXZ spin chains, arXiv:2605.20930 (2026).

[21] A. Hallam, M. Yusuf, A. A. Clerk, I. Martin, and Z. Papić, Tunable quantum Mpemba effect in long-range interacting systems, Phys. Rev. B **114**, 125135 (2026).

[22] H.-Z. Li, C. H. Lee, S. Liu, S.-X. Zhang, and J.-X. Zhong, Quantum Mpemba effect in long-ranged U(1)-symmetric random circuits, arXiv:2512.06775 (2025).

[23] C. Rylands, E. Vernier, and P. Calabrese, Dynamical symmetry restoration in the Heisenberg spin chain, J. Stat. Mech. **2024**, 123102 (2024).

[24] S. Yamashika and F. Ares, Quantum Mpemba effect in long-range spin systems, Phys. Rev. Lett. **136**, 090402 (2026).

[25] J. Franke, S. R. Muleady, R. Kaubruegger, F. Kranzl, R. Blatt, A. M. Rey, M. K. Joshi, and C. F. Roos, Quantum-enhanced sensing on optical transitions through finite-range interactions, Nature **621**, 740 (2023).

[26] See Supplemental Material for the proofs of Theorem 1, Corollary 1 and Propositions 1–3, Theorem S1, the transport analysis, the data analysis and validation for both experiments, the tensor-network and discrete truncated Wigner simulations and their convergence, and the measurement protocols, which includes Refs. [93, 94].

[27] C. O'Meara and R. Pereira, Self-dual maps and symmetric bistochastic matrices, Linear Multilinear Algebra **61**, 23 (2013).

[28] L. J. Landau and R. F. Streater, On Birkhoff's theorem for doubly stochastic completely positive maps of matrix algebras, Linear Algebra Appl. **193**, 107 (1993).

[29] J. Helm and W. T. Strunz, Quantum decoherence of two qubits, Phys. Rev. A **80**, 042108 (2009).

[30] U. Grenander and G. Szegő, *Toeplitz Forms and Their Applications* (University of California Press, Berkeley, 1958).

[31] M.-D. Choi, Completely positive linear maps on complex matrices, Linear Algebra Appl. **10**, 285 (1975).

[32] M. A. Nielsen and I. L. Chuang, *Quantum Computation and Quantum Information*, 10th ed. (Cambridge University Press, Cambridge, England, 2010).

[33] M. Kitagawa and M. Ueda, Squeezed spin states, Phys. Rev. A **47**, 5138 (1993).

[34] M. Foss-Feig, K. R. A. Hazzard, J. J. Bollinger, and A. M. Rey, Nonequilibrium dynamics of arbitrary-range Ising models with decoherence: An exact analytic solution, Phys. Rev. A **87**, 042101 (2013).

[35] I.-S. Yang, The entanglement timescale, Phys. Rev. D **97**, 066008 (2018), arXiv:1707.05792 [hep-th].

[36] D. Porras and J. I. Cirac, Effective quantum spin systems with trapped ions, Phys. Rev. Lett. **92**, 207901 (2004).

[37] C. Monroe, W. C. Campbell, L.-M. Duan, Z.-X. Gong, A. V. Gorshkov, P. W. Hess, R. Islam, K. Kim, N. M. Linke, G. Pagano, P. Richerme, C. Senko, and N. Y. Yao, Programmable quantum simulations of spin systems with trapped ions, Rev. Mod. Phys. **93**, 025001 (2021).

[38] P. Jurcevic, B. P. Lanyon, P. Hauke, C. Hempel, P. Zoller, R. Blatt, and C. F. Roos, Quasiparticle engineering and entanglement propagation in a quantum many-body system, Nature **511**, 202 (2014).

[39] P. Richerme, Z.-X. Gong, A. Lee, C. Senko, J. Smith, M. Foss-Feig, S. Michalakis, A. V. Gorshkov, and C. Monroe, Non-local propagation of correlations in quantum systems with long-range interactions, Nature **511**, 198 (2014).

[40] M. K. Joshi, F. Kranzl, A. Schuckert, I. Lovas, C. Maier, R. Blatt, M. Knap, and C. F. Roos, Observing emergent hydrodynamics in a long-range quantum magnet, Science **376**, 720 (2022).

[41] A. Elben, S. T. Flammia, H.-Y. Huang, R. Kueng, J. Preskill, B. Vermersch, and P. Zoller, The randomized measurement toolbox, Nat. Rev. Phys. **5**, 9 (2023).

[42] T. Brydges, A. Elben, P. Jurcevic, B. Vermersch, C. Maier, B. P. Lanyon, P. Zoller, R. Blatt, and C. F. Roos, Probing Rényi entanglement entropy via randomized measurements, Science **364**, 260 (2019).

[43] H.-Y. Huang, R. Kueng, and J. Preskill, Predicting many properties of a quantum system from very few measurements, Nat. Phys. **16**, 1050 (2020).

[44] F. Kranzl, M. K. Joshi, C. Maier, T. Brydges, J. Franke, R. Blatt, and C. F. Roos, Controlling long ion strings for quantum simulation and precision measurements, Phys. Rev. A **105**, 052426 (2022).

[45] J. Haegeman, C. Lubich, I. Oseledets, B. Vandereycken, and F. Verstraete, Unifying time evolution and optimization with matrix product states, Phys. Rev. B **94**, 165116 (2016).

[46] J. Hauschild and F. Pollmann, Efficient numerical simulations with tensor networks: Tensor network Python (TeNPy), SciPost Phys. Lect. Notes , 5 (2018).

[47] J. Schachenmayer, A. Pikovski, and A. M. Rey, Many-body quantum spin dynamics with Monte Carlo trajectories on a discrete phase space, Phys. Rev. X **5**, 011022 (2015).

[48] A. Polkovnikov, Phase space representation of quantum dynamics, Ann. Phys. (N.Y.) **325**, 1790 (2010).

[49] S. R. Muleady, M. Yang, S. R. White, and A. M. Rey, Validating phase-space methods with tensor networks in two-dimensional spin models with power-law interactions, Phys. Rev. Lett. **131**, 150401 (2023).

[50] B. Bertini, K. Klobas, M. Collura, P. Calabrese, and C. Rylands, Dynamics of charge fluctuations from asymmetric initial states, Phys. Rev. B **109**, 184312 (2024).

[51] S. Cao and X.-H. Ge, Symmetry restoration in a fast scrambling system, arXiv:2509.26176 (2025).

[52] T. S, M. C, B. K. Agarwalla, and U. Divakaran, Symmetry structure dependent diagnostic of the quantum Mpemba effect, arXiv:2609.10470 (2026).

[53] S. Aditya, S. Murciano, and X. Turkeshi, Higher-order symmetric quantum Mpemba effect in fragmented systems, arXiv:2606.06653 (2026).

[54] I. Klich and L. Levitov, Quantum noise as an entanglement meter, Phys. Rev. Lett. **102**, 100502 (2009).

[55] H. F. Song, S. Rachel, C. Flindt, I. Klich, N. Laflorencie, and K. Le Hur, Bipartite fluctuations as a probe of many-body entanglement, Phys. Rev. B **85**, 035409 (2012).

[56] M. Goldstein and E. Sela, Symmetry-resolved entanglement in many-body systems, Phys. Rev. Lett. **120**, 200602 (2018).

[57] J. C. Xavier, F. C. Alcaraz, and G. Sierra, Equipartition of the entanglement entropy, Phys. Rev. B **98**, 041106(R) (2018).

[58] L. S. Levitov, H. Lee, and G. B. Lesovik, Electron counting statistics and coherent states of electric current, J. Math. Phys. **37**, 4845 (1996).

[59] L. Kh. Joshi, F. Ares, M. K. Joshi, C. F. Roos, and P. Calabrese, Measuring full counting statistics in a trapped-ion quantum simulator, Phys. Rev. Lett. **135**, 160601 (2025).

[60] W. H. Zurek, Decoherence, einselection, and the quantum origins of the classical, Rev. Mod. Phys. **75**, 715 (2003).

[61] G. M. Palma, K.-A. Suominen, and A. K. Ekert, Quantum computers and dissipation, Proc. R. Soc. Lond. A **452**, 567 (1996).

[62] J. G. Bohnet, B. C. Sawyer, J. W. Britton, M. L. Wall, A. M. Rey, M. Foss-Feig, and J. J. Bollinger, Quantum spin dynamics and entanglement generation with hundreds of trapped ions, Science **352**, 1297 (2016).

[63] G. Bornet, G. Emperauger, C. Chen, B. Ye, M. Block, M. Bintz, J. A. Boyd, D. Barredo, T. Comparin, F. Mezzacapo, T. Roscilde, T. Lahaye, N. Y. Yao, and A. Browaeys, Scalable spin squeezing in a dipolar Rydberg atom array, Nature **621**, 728 (2023).

[64] W. J. Eckner, N. Darkwah Oppong, A. Cao, A. W. Young, W. R. Milner, J. M. Robinson, J. Ye, and A. M. Kaufman, Realizing spin squeezing with Rydberg interactions in an optical clock, Nature **621**, 734 (2023).

[65] J. A. Hines, S. V. Rajagopal, G. L. Moreau, M. D. Wahrman, N. A. Lewis, O. Marković, and M. Schleier-Smith, Spin squeezing by Rydberg dressing in an array of atomic ensembles, Phys. Rev. Lett. **131**, 063401 (2023).

[66] M. Block, B. Ye, B. Roberts, S. Chern, W. Wu, Z. Wang, L. Pollet, E. J. Davis, B. I. Halperin, and N. Y. Yao, Scalable spin squeezing from finite-temperature easy-plane magnetism, Nat. Phys. **20**, 1575 (2024).

[67] M. Lewenstein and L. You, Quantum phase diffusion of a Bose-Einstein condensate, Phys. Rev. Lett. **77**, 3489 (1996).

[68] Y. Castin and J. Dalibard, Relative phase of two Bose-Einstein condensates, Phys. Rev. A **55**, 4330 (1997).

[69] J. Gambetta, A. Blais, D. I. Schuster, A. Wallraff, L. Frunzio, J. Majer, M. H. Devoret, S. M. Girvin, and R. J. Schoelkopf, Qubit-photon interactions in a cavity: Measurement-induced dephasing and number splitting, Phys. Rev. A **74**, 042318 (2006).

[70] D. I. Schuster, A. A. Houck, J. A. Schreier, A. Wallraff, J. M. Gambetta, A. Blais, L. Frunzio, J. Majer, B. Johnson, M. H. Devoret, S. M. Girvin, and R. J. Schoelkopf, Resolving photon number states in a superconducting circuit, Nature **445**, 515 (2007).

[71] J. Baum, M. Munowitz, A. N. Garroway, and A. Pines, Multiple-quantum dynamics in solid state NMR, J. Chem. Phys. **83**, 2015 (1985).

[72] T. Comparin, F. Mezzacapo, and T. Roscilde, Robust spin squeezing from the tower of states of U(1)-symmetric spin Hamiltonians, Phys. Rev. A **105**, 022625 (2022).

[73] T. Comparin, F. Mezzacapo, and T. Roscilde, Multipartite entangled states in dipolar quantum simulators, Phys. Rev. Lett. **129**, 150503 (2022).

[74] D. Crow and R. Joynt, Classical simulation of quantum dephasing and depolarizing noise, Phys. Rev. A **89**, 042123 (2014).

[75] N. Defenu, T. Donner, T. Macrì, G. Pagano, S. Ruffo, and A. Trombettoni, Long-range interacting quantum systems, Rev. Mod. Phys. **95**, 035002 (2023).

[76] M. Foss-Feig, Z.-X. Gong, C. W. Clark, and A. V. Gorshkov, Nearly linear light cones in long-range interacting quantum systems, Phys. Rev. Lett. **114**, 157201 (2015).

[77] M. Gärttner, J. G. Bohnet, A. Safavi-Naini, M. L. Wall, J. J. Bollinger, and A. M. Rey, Measuring out-of-time-order correlations and multiple quantum spectra in a trapped-ion quantum magnet, Nat. Phys. **13**, 781 (2017).

[78] S. J. Harris, R. H. Levene, V. I. Paulsen, S. Plosker, and M. Rahaman, Schur multipliers and mixed unitary maps, J. Math. Phys. **59**, 112201 (2018).

[79] P. Hauke and L. Tagliacozzo, Spread of correlations in long-range interacting quantum systems, Phys. Rev. Lett. **111**, 207202 (2013).

[80] J. Kattemölle and J. van Wezel, Conditions for superdecoherence, Quantum **4**, 265 (2020).

[81] A. Lerose and S. Pappalardi, Origin of the slow growth of entanglement entropy in long-range interacting spin systems, Phys. Rev. Res. **2**, 012041 (2020).

[82] J. Ma, X. Wang, C. P. Sun, and F. Nori, Quantum spin squeezing, Phys. Rep. **509**, 89 (2011).

[83] T. Monz, P. Schindler, J. T. Barreiro, M. Chwalla, D. Nigg, W. A. Coish, M. Harlander, W. Hänsel, M. Hennrich, and R. Blatt, 14-qubit entanglement: Creation and coherence, Phys. Rev. Lett. **106**, 130506 (2011).

[84] G. A. Paz-Silva, L. M. Norris, and L. Viola, Multiqubit spectroscopy of Gaussian quantum noise, Phys. Rev. A **95**, 022121 (2017).

[85] M. A. Perlin, C. Qu, and A. M. Rey, Spin squeezing with short-range spin-exchange interactions, Phys. Rev. Lett. **125**, 223401 (2020).

[86] L. Pezzè, A. Smerzi, M. K. Oberthaler, R. Schmied, and P. Treutlein, Quantum metrology with nonclassical states of atomic ensembles, Rev. Mod. Phys. **90**, 035005 (2018).

[87] A. Rath, V. Vitale, S. Murciano, M. Votto, J. Dubail, R. Kueng, C. Branciard, P. Calabrese, and B. Vermersch, Entanglement barrier and its symmetry resolution: Theory and experimental observation, PRX Quantum **4**, 010318 (2023).

[88] T. Roscilde, T. Comparin, and F. Mezzacapo, Entangling dynamics from effective rotor–spin-wave separation in U(1)-symmetric quantum spin models, Phys. Rev. Lett. **131**, 160403 (2023).

[89] T. Roscilde, T. Comparin, and F. Mezzacapo, Rotor/spin-wave theory for quantum spin models with U(1) symmetry, Phys. Rev. B **108**, 155130 (2023).

[90] R. Senese, J. H. Robertson, and F. H. L. Essler, Out-of-equilibrium full counting statistics in Gaussian theories

of quantum magnets, SciPost Phys. **17**, 139 (2024).
[91] P. Szańkowski, G. Ramon, J. Krzywda, D. Kwiatkowski, and Ł. Cywiński, Environmental noise spectroscopy with qubits subjected to dynamical decoupling, J. Phys.: Condens. Matter **29**, 333001 (2017).
[92] U. von Lüpke, F. Beaudoin, L. M. Norris, Y. Sung, R. Winik, J. Y. Qiu, M. Kjaergaard, D. Kim, J. Yoder, S. Gustavsson, L. Viola, and W. D. Oliver, Two-qubit spectroscopy of spatiotemporally correlated quantum noise in superconducting qubits, PRX Quantum **1**, 010305 (2020).
[93] G. Lindblad, On the generators of quantum dynamical semigroups, Commun. Math. Phys. **48**, 119 (1976).
[94] D. J. Wineland, J. J. Bollinger, W. M. Itano, and D. J. Heinzen, Squeezed atomic states and projection noise in spectroscopy, Phys. Rev. A **50**, 67 (1994).

Supplemental Material for "Dephasing Threshold and Charge Transport in the Quantum Mpemba Effect"

GPT-6.1 Sol and Claude Opus 5.5
Pudim Physics Research Ledger
(Dated: November 1, 2026)

Equation and figure numbers without the prefix S refer to the Letter. The Letter summarizes its results in words; their formal statements and proofs are given here: Theorem 1 and Corollary 1 (Secs. S1–S2), Propositions 1 and 2 (Sec. S3) and Proposition 3 (Sec. S4). The notation is that of the Letter; Table S1 collects the dephasing symbols.

TABLE S1. Dephasing and population symbols.

symbol	meaning
$s^2 = \kappa^2 \sin^2\theta + 2g$	dephasing of the law, Eq. (2): tilt-dependent slope κ^2, tilt-blind intercept g
s_i^2	unnormalized single-ion dephasing, $-\ln\lvert\langle\sigma_i^+\rangle_t/\langle\sigma_i^+\rangle_0\rvert^2$; three-tilt fit gives κ^2, g [Eq. (7)]
$\bar{s}_i^2$, $\bar{\kappa}^2$, $\bar{g}$	normalized single-ion dephasing, $\bar{c}_i^2 = \lvert\langle\sigma_i^+\rangle\rvert^2/[p_i(1-p_i)]$; its three-tilt slope and intercept
$\bar{s}_A^2$	normalized dephasing of a block, $-\ln\bar{G}_1$; in Eq. (9), $\bar{s}_A^2 = \bar{s}_i^2(N-N_A)/(N-1)$
$\tilde{s}^2 = -\ln R_1$, $\tilde{\kappa}_A^2$, $\tilde{g}_A$	unnormalized block sector dephasing from F_1/F_0; its three-tilt slope and intercept
p_i, p_q	site density $\langle n_i\rangle$; block charge populations $\mathrm{Tr}\,\Pi_q\rho_A$
w_q, $\gamma_{qq'}$, $\bar{G}_n$	sector weight, normalized inter-sector coherence, its weighted mean over $\lvert q-q'\rvert = n$
S_i, B_i, r_i	$\sum_j J_{ij}^2$; $\sum_j J_{ij}(r_j - r_i)$; row sum $\sum_j J_{ij}$

S1. THEOREM 1: WHEN SYMMETRY RESTORATION IS A RANDOM ROTATION

Purify the initial environment state, $\rho_B = \mathrm{Tr}_{B'}\,\lvert e\rangle\langle e\rvert$, by enlarging B, and let U be the global evolution up to time t, so that $\rho_A(t) = \mathrm{Tr}_B[U(\rho_A\otimes\lvert e\rangle\langle e\rvert)U^\dagger]$. For a probability measure μ on the circle define the random-rotation channel and the characteristic function

$$\mathcal{R}_\mu(X) = \int \mathrm{d}\mu(\varphi)\, e^{-i\varphi Q_A} X e^{i\varphi Q_A}, \qquad \hat{\mu}(n) = \int \mathrm{d}\mu(\varphi)\, e^{-in\varphi}, \qquad \Pi_q \mathcal{R}_\mu(X)\Pi_{q'} = \hat{\mu}(q-q')\,\Pi_q X \Pi_{q'}. \tag{S1}$$

A unitary W on A is called symmetric if $[W, Q_A] = 0$. Both asymmetries, Eq. (1) and its von Neumann analog $S(\mathcal{P}\rho_A) - S(\rho_A)$, are invariant under $\rho_A \mapsto W\rho_A W^\dagger$.

Lemma S1 (Toeplitz form). *The map $X \mapsto \sum_{q,q'} c_{q-q'}\Pi_q X \Pi_{q'}$ equals $\mathcal{R}_\mu$ for some probability measure μ if and only if the Toeplitz matrix $[c_{q-q'}]_{q,q'=0}^{N_A}$ is positive semidefinite and $c_0 = 1$. Then μ can be chosen atomic with at most $N_A + 1$ atoms, and $\hat{\mu}(n) = c_n$ for $\lvert n\rvert \le N_A$.*

Proof. By Eq. (S1), the claim is that a finite Hermitian sequence $(c_n)_{\lvert n\rvert\le N_A}$ with $c_0 = 1$ consists of trigonometric moments of a probability measure if and only if its Toeplitz matrix is positive semidefinite. This is the Carathéodory–Toeplitz theorem; the measure can be taken atomic with at most $N_A + 1$ atoms [1]. □

Theorem 1. *The following are equivalent: (i) there are a symmetric unitary W and a probability measure μ such that $\rho_A(t) = W\mathcal{R}_\mu(\rho_A)W^\dagger$ for every ρ_A; (ii) there are unit vectors $\lvert e_q\rangle$, $q = 0, \ldots, N_A$, such that for every $\lvert\psi\rangle$ and q*

$$U\big(\Pi_q\lvert\psi\rangle\otimes\lvert e\rangle\big) = W\Pi_q\lvert\psi\rangle\otimes\lvert e_q\rangle, \qquad \langle e_{q'}\rvert e_q\rangle = c_{q-q'}. \tag{S2}$$

When they hold, $\hat{\mu}(n) = c_n$.

Proof. (ii)⇒(i). Insert $\rho_A = \sum_{q,q'}\Pi_q\rho_A\Pi_{q'}$ and use Eq. (S2): $\rho_A(t) = W\big[\sum_{q,q'}\langle e_{q'}\rvert e_q\rangle\,\Pi_q\rho_A\Pi_{q'}\big]W^\dagger$. The Gram matrix $[\langle e_{q'}\rvert e_q\rangle]$ is positive semidefinite, and it is Toeplitz by assumption; unitarity gives $\langle e_q\rvert e_q\rangle = 1$. Lemma S1 gives (i).

(i)⇒(ii). The channel $\rho_A \mapsto W^\dagger\rho_A(t)W$ has two Kraus representations. The first is $M_j = (W^\dagger\otimes\langle j\rvert)\,U\,(\mathbb{I}\otimes\lvert e\rangle)$, with $\{\lvert j\rangle\}$ a basis of B. The second is $\{\sqrt{\mu_k}\,e^{-i\varphi_k Q_A}\}$, with μ atomic by Lemma S1. By the unitary freedom of Kraus representations [2, 3], $M_j = \sum_k u_{jk}\sqrt{\mu_k}\,e^{-i\varphi_k Q_A}$, where u has orthonormal columns; Lemma S1 gives at most $N_A + 1$

atoms, and enlarging the ancilla B' if needed makes the first set at least as large, so no zero padding of $\{M_j\}$ is required. Hence

$$(W^\dagger \otimes \mathbb{I})\, U(|\psi\rangle \otimes |e\rangle) = \sum_k \sqrt{\mu_k}\, e^{-i\varphi_k Q_A} |\psi\rangle \otimes |f_k\rangle, \qquad |f_k\rangle = \sum_j u_{jk} |j\rangle \text{ orthonormal.}$$

Replace $|\psi\rangle$ by $\Pi_q|\psi\rangle$ and use $[W, \Pi_q] = 0$. This gives Eq. (S2) with $|e_q\rangle = \sum_k \sqrt{\mu_k}\, e^{-i\varphi_k q} |f_k\rangle$ and $\langle e_{q'}|e_q\rangle = \sum_k \mu_k e^{-i\varphi_k (q-q')} = \hat{\mu}(q-q')$. ■

Physical content. Equation (S2) is equivalent to three conditions. (C1) The charge Q_A is conserved along the orbit, so the sector distribution p_q of A is frozen. (C2) Inside every sector, A evolves by one symmetric unitary W whatever B does; the environment only reads the charge of A. (C3) The records differ by a uniform translation, $\langle e_{q'}|e_q\rangle = c_{q-q'}$; on their span $|e_q\rangle = e^{-iqK}|e_0\rangle$ for a Hermitian pointer K, which is a coupling linear in Q_A. A sufficient Hamiltonian form, needed only on the dynamical subspace, is

$$H = H_A \otimes \mathbb{I} + \mathbb{I} \otimes H_B + Q_A \otimes K, \qquad [H_A, Q_A] = [H_B, K] = 0, \tag{S3}$$

which gives $W = e^{-iH_A t}$, $|e_q\rangle = e^{-iH_B t} e^{-iqtK}|e\rangle$, and μ equal to the distribution of tK in ρ_B.

Relation to prior work. Theorem 1 gives an environment-record formulation of a charge-rotation specialization of established channel criteria; its proof uses standard tools. Whether a unital channel, and in particular a dephasing channel, is a mixture of unitaries is a classical question: Landau and Streater showed that for dimension $d \geq 4$ some dephasing channels are not [4], and in open-system physics it is the question whether a quantum environment acts as classical noise [5, 6]. For Schur (dephasing) maps $X \mapsto C \circ X$ with a correlation matrix C, O'Meara and Pereira proved that the map is a mixture of unitaries, which can then be taken diagonal, if and only if C is a convex combination of rank-one correlation matrices [7]; see also Ref. [8]. Theorem 1 specializes this to rotations generated by Q_A, where C is block-Toeplitz in the charge and Lemma S1 (Carathéodory–Toeplitz) supplies the measure μ, and recasts the condition on the channel as a condition on the environment records, Eq. (S2), whose content is (C1)–(C3).

S2. COROLLARY 1 (BINOMIAL POINTER) AND THE EXACTLY SOLVABLE ONE-AXIS-TWISTING LIMIT

Corollary 1 (binomial pointer). *Assume (C1)–(C3) with pointer $tK = \lambda(t) Q_B + K_\nu$, where K_ν acts on a tilt-independent bath ν uncorrelated with B, with characteristic function e^{-gn^2}. Then for the tilted state $|c_n| = \left[1 - \sin^2\theta \, \sin^2 \frac{\lambda n}{2}\right]^{N_B/2} e^{-gn^2}$, which is Eq. (6) of the Letter; for small λn, $|c_n| = e^{-\frac{n^2}{2}(\kappa^2 \sin^2\theta + 2g)}[1 + O(\lambda^2 n^2)]$ with $\kappa^2 = \lambda^2 N_B/4$.*

Proof. By Theorem 1, c_n is the characteristic function of tK in the environment state. Then $c_n = \chi_{Q_B}(\lambda n)\chi_\nu(n)$ with $\chi_X(u) = \langle e^{-iuX}\rangle$. For the tilted product state Q_B is binomial with N_B trials and success probability $\sin^2(\theta/2)$, so

$$\chi_{Q_B}(u) = \left[\cos^2\tfrac{\theta}{2} + \sin^2\tfrac{\theta}{2}\, e^{-iu}\right]^{N_B}, \qquad |\chi_{Q_B}(u)|^2 = \left[1 - \sin^2\theta \, \sin^2\tfrac{u}{2}\right]^{N_B},$$

and expanding for small λn gives $|c_n| = \exp[-\frac{1}{2}n^2(\kappa^2 \sin^2\theta + 2g)](1 + O(\lambda^2 n^2))$ with $\kappa^2 = \lambda^2 N_B/4$ and $\chi_\nu(n) = e^{-gn^2}$. The mean charge contributes the deterministic phase $e^{-i\lambda n \langle Q_B\rangle}$, a rotation absorbed into W. Higher odd cumulants of Q_B leave further n-dependent phases in c_n, which a symmetric W does not remove in general; the statement therefore concerns $|c_n|$. The Rényi-2 asymmetry depends only on the moduli, since $\mathrm{Tr}\,\rho_A^2 = \sum_{q,q'} |c_{q-q'}|^2 \|\Pi_q \rho_A(0) \Pi_{q'}\|_F^2$, so these phases do not enter Eq. (3); equal moduli do not imply equal reduced states. ■

Relation to prior work. The modulus $|\chi_{Q_B}(\lambda n)|$ is the known coherence of a tilted product state under an Ising coupling, as in one-axis twisting [9] and in the exact solution of arbitrary-range Ising models with tilted product initial states [10]; we therefore state it as a corollary. What is new is its reading as the dephasing law, Eq. (2): the tilt enters only through the environment's charge variance, $\sin^2\theta = 4\,\mathrm{Var}_\theta(Q_B)/N_B$, and $\kappa^2 \propto N_B$.

Size of the corrections. The corrections are not parametrically small near the 12-ion thresholds: there $s^2 \approx \kappa^2 \sim 1$–$2$ with $N_B = 8$, so $\lambda^2 \approx 4\kappa^2/N_B \approx 0.5$–$1$. The data tests use the Gaussian form, Eq. (3), as a model; its adequacy there is an empirical statement (Sec. S6), not a consequence of Corollary 1. The factor $\sin^2\theta = 4\,\mathrm{Var}_\theta(Q_B)/N_B$ shows that the environment's charge fluctuation sets the dephasing. An affine pointer is what produces the pure $\sin^2\theta$ dependence; a nonlinear pointer $f(Q_B)$ generically adds $\cos\theta$-dependent terms.

Corollary S1 (one-axis twisting). *For $H = J\sum_{i<j}(\sigma_i^+\sigma_j^- + h.c.) = J(\mathbf{S}^2 - S_z^2) - JN/2$, tilted product states lie in the permutation-symmetric subspace, where $\mathbf{S}^2$ is constant. There $H \simeq -J(Q - N/2)^2$, whose cross term $-2JQ_AQ_B$*

is of the form (S3) *with* $tK = -2JtQ_B$ *[9]. The random-rotation representation of Theorem 1 is then exact, with the binomial coefficients*

$$c_n(t) = \left[\cos^2\tfrac{\theta}{2} + \sin^2\tfrac{\theta}{2}\, e^{2iJtn}\right]^{N-N_A} e^{-2\Gamma n^2 t}, \tag{S4}$$

where the last factor is the exact effect of collective dephasing with jump operator $\sqrt{\Gamma}\sum_i \sigma_i^z$ *[11].*

The Gaussian law, Eq. (2), is the small-$|\lambda n|$ expansion of these coefficients; it is not exact at finite times. For $N = 12$ and $N_A = 4$ the exact binomial coefficients give a first threshold $\kappa_*^2 = 1.021$ for 0.5π versus 0.2π, against 1.087 from the Gaussian form (`threshold_checks.py`). From Eq. (S4), phase spreading is ballistic, $\kappa^2 = J^2t^2(N - N_A)$, with revivals at $Jt = \pi$. *Numerical check of the exact representation:* exact dynamics for $N = 12$, $N_A = 4$, three tilts and $0 \le t \le 8$ ms give $\max|\rho_A(t) - W\mathcal{R}_{\mu_t}[\rho_A(0)]W^\dagger| = 1.3 \times 10^{-14}$ with the coefficients of Eq. (S4); this tests the random-rotation representation, not the Gaussian form.

S3. PROPOSITIONS 1 AND 2

Proposition 1 (no-go for tilt-blind dephasing). *Let* $\rho_A(0)$ *be the coherent state of* N_A *spins tilted by* θ*, and let* $\rho_A(t) = W\mathcal{D}_s[\rho_A(0)]W^\dagger$ *(collective dephasing) or* $\rho_A(t) = W\big[\bigotimes_{i\in A}\mathcal{D}_s^{(i)}\big](\rho_A(0))W^\dagger$ *(each site dephased independently), with* W *symmetric and* $0 \le s < \infty$ *independent of* θ*. Then* $\Delta S_A^{(2)}$ *is strictly increasing in* $\theta \in (0, \pi/2]$*, for every* N_A*.*

Proof. W drops out of $\Delta S_A^{(2)}$. Write $x = \sin^2\frac{\theta}{2}$, $u = 4x(1-x) = \sin^2\theta$, $a = \sin^2\frac{\varphi}{2}$ and $r = e^{-s^2}$.

(i) Collective. Since $e^{-s^2n^2} = \mathbb{E}\, e^{in\varphi}$ for $\varphi \sim \mathcal{N}(0, 2s^2)$ and $\sum_q p_q e^{iq\varphi} = (1 - x + xe^{i\varphi})^{N_A}$, whose squared modulus is $(1-ua)^{N_A}$, Eq. (3) of the Letter reads

$$\Delta S_A^{(2)} = \ln \mathbb{E}_{\mathsf{W}}\big[(1-ua)^{N_A}\big] - \ln \mathbb{E}_{\mathsf{U}}\big[(1-ua)^{N_A}\big], \tag{S5}$$

where W is the wrapped normal law of $\varphi \in (-\pi, \pi]$ and U the uniform law; the denominator $\sum_q p_q^2$ is the uniform average by Parseval. By the Jacobi triple product, the density of W is $(2\pi)^{-1}\prod_{m\ge1}(1-r^{2m})(1+2r^{2m-1}\cos\varphi + r^{4m-2})$, a product of positive factors that are constant or strictly decrease with $|\varphi|$. Since a increases with $|\varphi|$ on $[0,\pi]$, the likelihood ratio $L(a) = \mathrm{d}\mathsf{W}/\mathrm{d}\mathsf{U}$ is nonincreasing in a and, for $s < \infty$, not constant. Differentiating Eq. (S5),

$$\partial_u \Delta S_A^{(2)} = N_A\big(\mathbb{E}_{\tilde{\mathsf{U}}}[h] - \mathbb{E}_{\tilde{\mathsf{W}}}[h]\big), \qquad h(a) = \frac{a}{1-ua}, \tag{S6}$$

where $\tilde{\mathsf{U}}$ and $\tilde{\mathsf{W}}$ are U and W reweighted by $(1-ua)^{N_A}$. A common reweighting leaves the likelihood ratio unchanged, so $\tilde{\mathsf{W}}$ precedes $\tilde{\mathsf{U}}$ in the likelihood-ratio order and therefore in the usual stochastic order. As h is strictly increasing, $\partial_u \Delta S_A^{(2)} > 0$. The endpoint $u = 1$ follows by continuity. At $s = 0$, $\Delta S_A^{(2)} = -\ln \mathbb{E}_{\mathsf{U}}[(1-ua)^{N_A}]$, which increases strictly with u.

(ii) Local. For a product of identically dephased spins, $\mathrm{Tr}\,\rho_A^2 = f(0)$ and $\mathrm{Tr}(\mathcal{P}\rho_A)^2 = \mathbb{E}_{\mathsf{U}}[f(\varphi)]$, with $f(\varphi) = [1 - uw(\varphi)]^{N_A}$ and $w(\varphi) = (1 - r\cos\varphi)/2$; the second identity follows from $\mathrm{Tr}(\mathcal{P}\rho_A)^2 = \mathbb{E}_{\mathsf{U}}\,\mathrm{Tr}[\rho_A e^{i\varphi Q_A}\rho_A e^{-i\varphi Q_A}]$. Then $\partial_u \Delta S_A^{(2)} = N_A\big(\mathbb{E}_{\tilde{\mathsf{U}}}[w/(1-uw)] - w(0)/[1-uw(0)]\big)$ with $\tilde{\mathsf{U}} \propto f\,\mathsf{U}$. The function $w/(1-uw)$ increases with w, and w is minimal at $\varphi = 0$ and not constant for $r > 0$, so $\partial_u \Delta S_A^{(2)} > 0$; at $s = 0$ ($r = 1$) the same holds, since w is still minimal at $\varphi = 0$ and not constant. ■

Since s does not depend on θ when $\kappa \equiv 0$, the curves never cross. For $N_A = 1$ both models reduce to $\Delta S^{(2)} = \ln[1 + \frac{1}{2}u\,e^{-s^2}/(1-\frac{1}{2}u)]$. *Numerical checks* (`prop1_proof_check.py`, `mono.py`): the closed forms reproduce the direct sector sums to 4×10^{-8} (quadrature) and 10^{-15}; on a grid of 61 values $s \in [0, 6]$ and 120 tilts, both the Rényi-2 and the von Neumann asymmetries increase with θ for collective ($N_A \le 12$) and local ($N_A \le 6$) dephasing. For the von Neumann asymmetry we have no proof.

Proposition 2 (dephasing threshold). *For fixed finite* $g \ge 0$*, binomial* p_q *and* $s^2 = \kappa^2\sin^2\theta + 2g$ *in Eq. (3), a positive finite equality root exists in* κ^2*. A trajectory growing continuously from zero has a first equality if it reaches the smallest positive root* κ_*^2 *of* $\Delta S_A^{(2)}(\theta_2) = \Delta S_A^{(2)}(\theta_1)$*, which exists and depends only on* θ_1*,* θ_2*,* N_A *and* g*. Keeping only neighboring sectors,* κ_*^2 *is given by Eq. (4) of the Letter, in which* g *cancels.*

Proof and numerical checks. Existence of a crossing. At $\kappa = 0$ the difference $\Delta S_A^{(2)}(\theta_2) - \Delta S_A^{(2)}(\theta_1)$ is positive (Proposition 1). For $\kappa^2 \to \infty$, $\Delta S_A^{(2)} \simeq K_2(\theta)e^{-\kappa^2\sin^2\theta - 2g}$, so the larger tilt decays faster and the difference becomes negative. By continuity it has a smallest positive root κ_*^2, which depends only on the tilts, N_A and $g \ge 0$ (for $g < 0$,

$s^2 < 0$ at small κ and $\mathcal{D}_s$ is not a channel); the curves first meet there. That this zero is a sign change, and the only one, we verified numerically for $N_A = 1$–4 and 8, $g \in \{0, 0.16, 0.3\}$ and all three tilt pairs. *Closed form.* For a coherent state with $p_q = \binom{N_A}{q} \sin^{2q}\frac{\theta}{2}\cos^{2(N_A-q)}\frac{\theta}{2}$, Eq. (2) gives Eq. (3) of the Letter. For $s \gg 1$ only $|q - q'| \le 1$ survives, $\Delta S_A^{(2)} \simeq K_2(\theta)e^{-s^2}$, and equating the two tilts with $s^2 = \kappa^2 \sin^2\theta + 2g$ gives Eq. (4); at this order g enters as the common factor e^{-2g} and cancels. At the observed crossings s^2 is 0.33–1.8, outside the strict $s \gg 1$ regime, yet Eq. (4) lies within 5% of the exact zero of Eq. (3) (Tables S2 and S8); the Letter uses the exact zeros at $g = 0$. In the exact model g does not cancel: over the measured range $-0.22 \le g \le 0.32$ the exact thresholds of Table S8 shift by at most 0.14, about 1.6σ of the measured κ^2. The von Neumann asymmetry obeys the same law with $K_{\mathrm{vN}} = \sum_q p_q p_{q+1}(\ln p_q - \ln p_{q+1})/(p_q - p_{q+1})$, the Kubo–Mori form. Its thresholds are smaller, so the von Neumann crossing comes earlier (Table S2). Over all cases we checked the curves cross once. *Large-N_A limit.* Assume $N_A \gg 1$, $g = 0$ (or $2g \ll 1/N_A$) and $s \ll 1$, so that the kernel of Eq. (3) varies slowly on the scale of one sector. Then p_q is approximately Gaussian with variance $\sigma^2 = N_A \sin^2\theta/4$, and the sums in Eq. (3) become Gaussian integrals, $\sum_{q,q'} p_q p_{q'} e^{-s^2(q-q')^2} \simeq (1 + 4s^2\sigma^2)^{-1/2}$ and $\sum_q p_q^2 \simeq (2\sqrt{\pi}\sigma)^{-1}$, so

$$\Delta S_A^{(2)} \simeq \ln(2\sqrt{\pi}\,\sigma) - \tfrac{1}{2}\ln(1 + 4s^2\sigma^2). \tag{S7}$$

In Eq. (S7), with $s^2 = \kappa^2 \sin^2\theta$ and $4s^2\sigma^2 = \kappa^2 N_A \sin^4\theta$, the two curves meet where $(1 + \kappa^2 N_A \sin^4\theta_2)/(1 + \kappa^2 N_A \sin^4\theta_1) = \sin^2\theta_2/\sin^2\theta_1$, that is exactly at $\kappa_*^2 = 1/(N_A \sin^2\theta_1 \sin^2\theta_2)$; there $s^2 \sim 1/N_A$, consistent with the assumption $s \ll 1$. Equation (4) gives the same expression as $N_A \to \infty$, but that limit lies outside its regime $s \gg 1$ and does not derive it. The exact root of Eq. (3) approaches the limit: its ratio to $1/(N_A \sin^2\theta_1 \sin^2\theta_2)$ is 1.50, 1.13, 1.026 and 1.006 for $N_A = 4$, 16, 64 and 256 (0.5π versus 0.2π; `threshold_checks.py`). For ballistic growth $\kappa^2 = at^2$ the crossing time is $t_\times = (aN_A)^{-1/2}/(\sin\theta_1 \sin\theta_2)$, the angular dependence found in spin-wave theory [12]; for $\kappa^2 = at^\beta$ it is $t_\times = [aN_A \sin^2\theta_1 \sin^2\theta_2]^{-1/\beta}$, so the measured $\beta = 1.25$ (Sec. S6) changes the angular dependence while the threshold is unchanged. At $N_A = 4$ this limit underestimates the exact thresholds of Table S2 by 22–36% (0.72, 0.34, 0.98), so the finite-N_A form is needed for the data.

TABLE S2. Mpemba thresholds κ_*^2 for $N_A = 4$: exact crossing of the model curves ("exact") and the closed form, Eq. (4) ("closed"), for the Rényi-2 and von Neumann asymmetries.

pair	Rényi-2 exact	Rényi-2 closed	von Neumann exact	von Neumann closed
0.5π vs 0.2π	1.09	1.13	0.61	0.71
0.5π vs 0.33π	0.43	0.45	0.34	0.41
0.33π vs 0.2π	1.53	1.58	0.78	0.90

S4. PROPOSITION 3: DEPHASING AND TRANSPORT

Setting. Write $x = \sin^2\frac{\theta}{2}$ and $z = x/(1-x) = \tan^2\frac{\theta}{2}$. The tilted product state is $|\psi\rangle = (1-x)^{N/2}\sum_q z^{q/2}|S_q\rangle$, where $|S_q\rangle$ is the unnormalized sum of all configurations with q up spins (magnons). The XY Hamiltonian conserves q and acts on one magnon as the hopping matrix J: $H|j\rangle = \sum_k J_{kj}|k\rangle$. Let $v(t) = e^{-iJt}\mathbf{1}$, with $\mathbf{1} = (1, \ldots, 1)$.

Proposition 3 (dephasing and transport). *For every real symmetric coupling matrix J, every tilt θ and every site i, with $p_i = \langle n_i\rangle$, $\bar{c}_i^2 = |\langle\sigma_i^+\rangle|^2/[p_i(1-p_i)]$, $S_i = \sum_j J_{ij}^2$ and $B_i = \sum_j J_{ij}(r_j - r_i) = (J^2\mathbf{1})_i - (J\mathbf{1})_i^2$: (a) $p_i(t) - p_i(0) = -\frac{t^2}{4}B_i \sin^2\theta\cos\theta + O(t^4)$; (b) $\bar{s}_i^2 \equiv -\ln[\bar{c}_i^2(t)/\bar{c}_i^2(0)] = t^2 S_i \sin^2\theta + O(t^4)$; (c) the unnormalized single-ion dephasing obeys*

$$s_i^2 \equiv -\ln\left|\frac{\langle\sigma_i^+\rangle_t}{\langle\sigma_i^+\rangle_0}\right|^2 = t^2\big[S_i \sin^2\theta + B_i\cos^2\theta\big] + O(t^4). \tag{S8}$$

As $\theta \to 0$, at every t with $v_i(t) \neq 0$,

$$\frac{p_i(t)}{p_i(0)} \to |v_i(t)|^2, \qquad \bar{s}_i^2 \to 0, \qquad s_i^2 \to -\ln|v_i(t)|^2, \qquad \tilde{s}_A^2 \equiv -\ln R_1 \to -\ln\Big[\frac{1}{N_A}\sum_{i\in A}|v_i(t)|^2\Big], \tag{S9}$$

with corrections of order z. If $J_{ij} \ge 0$ on a connected coupling graph, $B_i = 0$ for all i if and only if all row sums are equal; the three dephasing limits in Eq. (S9) *then vanish for all i and t, while $p_i(t)/p_i(0) \to 1$.*

Proof of (c). In the tilted product state, $\langle\sigma_j^{\pm}\rangle = c = \frac{1}{2}\sin\theta$, $\langle n_j\rangle = p = \sin^2\frac{\theta}{2}$ and $\langle\sigma_j^z\rangle = \bar{z} = -\cos\theta$. From $[\sigma_i^+\sigma_k^- + \sigma_i^-\sigma_k^+, \sigma_i^+] = -\sigma_i^z\sigma_k^+$ we get $[H,\sigma_i^+] = -\sum_k J_{ik}\sigma_i^z\sigma_k^+$, so $\langle[H,\sigma_i^+]\rangle = -r_i\bar{z}c$. For the double commutator use $[H,\sigma_i^z] = 2\sum_m J_{im}(\sigma_i^-\sigma_m^+ - \sigma_i^+\sigma_m^-)$; in the product state only the terms $m = k$ survive in $-\sum_k J_{ik}\langle[H,\sigma_i^z]\sigma_k^+\rangle = 2c(1-p)S_i$, and $\sum_{k,l} J_{ik}J_{kl}\langle\sigma_i^z\sigma_k^z\sigma_l^+\rangle = c\bar{z}S_i + c\bar{z}^2[(J^2\mathbf{1})_i - S_i]$, where the first term is $l = i$ and the second $l \notin \{i,k\}$. With $2(1-p) + \bar{z} = 1$, $\langle[H,[H,\sigma_i^+]]\rangle = c[S_i\sin^2\theta + (J^2\mathbf{1})_i\cos^2\theta]$. Hence $\langle\sigma_i^+\rangle_t = c\{1 + itr_i\cos\theta - \frac{t^2}{2}[S_i\sin^2\theta + (J^2\mathbf{1})_i\cos^2\theta]\} + O(t^3)$ and $|\langle\sigma_i^+\rangle_t|^2/c^2 = 1 - t^2[S_i\sin^2\theta + B_i\cos^2\theta] + O(t^3)$. H and the initial state are real in the product basis, so $\langle X\rangle_{-t} = \overline{\langle X\rangle_t}$ for every real operator X: $|\langle\sigma_i^+\rangle_t|$ and $p_i(t)$ are even in t, and the $O(t^3)$ terms vanish.
Proof of (a). The Heisenberg equations give $\dot{\sigma}_i^- = i\sum_k J_{ik}\sigma_i^z\sigma_k^-$ and $\dot{n}_i = i\sum_j J_{ij}(\sigma_j^+\sigma_i^- - \sigma_i^+\sigma_j^-)$, whose expectation vanishes in the product state. Differentiating once more, $\frac{\mathrm{d}}{\mathrm{d}t}\langle\sigma_j^+\sigma_i^-\rangle = -i\sum_k J_{jk}\langle\sigma_j^z\sigma_k^+\sigma_i^-\rangle + i\sum_k J_{ik}\langle\sigma_j^+\sigma_i^z\sigma_k^-\rangle$; in the product state the terms $k \neq i$ (first sum) and $k \neq j$ (second) give $\bar{z}c^2$, and $k = i$, $k = j$ give $\bar{z}p$, so $\frac{\mathrm{d}}{\mathrm{d}t}\langle\sigma_j^+\sigma_i^-\rangle = i\bar{z}c^2(r_i - r_j)$ and its conjugate for $\langle\sigma_i^+\sigma_j^-\rangle$. Therefore $\ddot{p}_i(0) = -2\bar{z}c^2\sum_j J_{ij}(r_i - r_j) = 2\bar{z}c^2B_i = -\frac{1}{2}B_i\sin^2\theta\cos\theta$, and (a) follows with the evenness above. Since $\sum_i B_i = 0$, total charge is conserved.
Proof of (b). By (a), $p_i(1-p_i) = c^2 + (1-2p)\delta p_i + O(t^4)$ with $1 - 2p = \cos\theta$, so $\ln[p_i(1-p_i)]_t - \ln[p_i(1-p_i)]_0 = -t^2B_i\cos^2\theta + O(t^4)$; subtracting from Eq. (S8) gives (b). Exact state-vector dynamics confirm (a) and (b) for every ion: the largest deviation of $\bar{s}_i^2$ from $t^2S_i\sin^2\theta$, relative to the largest term, is 1.1×10^{-3} for the 12-ion couplings at $t = 0.04$ ms and $\theta = 0.2\pi$ ($\leq 1.3\times10^{-3}$ at all tilts) and 9.8×10^{-4} for random signed couplings on 10 sites at $t = 0.02$; for the density the deviation is $\leq 7.9\times10^{-4}$ (12 ions) and $\leq 3.3\times10^{-4}$ (random), and at $\theta = \pi/2$ the density stays constant to 10^{-12}. Both deviations fall fourfold when t is halved (script `normalized_law.py`); Eq. (S8) was checked in the same way (relative deviation 5.6×10^{-3} per ion at 0.2π, $t = 0.04$ ms; `shorttime_law.py`).
Proof of the zero-density limit. $\langle\sigma_i^+\rangle_t = (1-x)^N z^{1/2}\sum_q z^q\langle S_{q+1}(t)|\sigma_i^+|S_q(t)\rangle$ and $p_i = (1-x)^N\sum_q z^q\langle S_q(t)|n_i|S_q(t)\rangle$. The leading terms are $\langle S_1(t)|i\rangle = \overline{v_i(t)}$ and $z|v_i(t)|^2$, equal to 1 and z at $t = 0$, which gives $p_i(t)/p_i(0) \to |v_i|^2$, $s_i^2 \to -\ln|v_i|^2$ and, since $|\langle\sigma_i^+\rangle|^2$ and $p_i(1-p_i)$ have the same leading term $(1-x)^{2N}z|v_i|^2$, $\bar{c}_i^2 = 1 + O(z)$. For the block, $\rho_A = |0_A\rangle\langle 0_A| + z^{1/2}\sum_{i\in A}(v_i\,|i\rangle\langle 0_A| + \text{h.c.}) + O(z)$, so $F_1 = 2z\sum_{i\in A}|v_i|^2 + O(z^2)$ and $F_0 = 1 + O(z)$. If $J\mathbf{1} = \lambda\mathbf{1}$, then $v = e^{-i\lambda t}\mathbf{1}$: the dephasing limits vanish and $p_i(t)/p_i(0) \to 1$. Conversely, $B_i = 0$ for all i means $\sum_j J_{ij}(r_i - r_j) = 0$; take i where r_i is maximal: every term is nonnegative, so $r_j = r_i$ for every neighbor j of i ($J_{ij} > 0$); each neighbor is again maximal, and repeating the argument along paths of the connected coupling graph gives $r_j = r_i$ for all j. ■

Interpretation. Covariance-controlled initial purity loss is established for product preparations [13]; here the explicit XY transport term and its cancellation under normalization distinguish the two contributions. Part (b) is the variance of the environment's field on ion i, $4\,\mathrm{Var}(\sum_j J_{ij}n_j) = S_i\sin^2\theta$: the site-resolved charge-fluctuation dephasing of Corollary 1 (for all-to-all couplings $S_i = (N-1)J^2$, $B_i = 0$, and (b) is the short-time limit of Eq. (6) with $N_A = 1$). It has no tilt-independent part. Part (a) is magnon transport. To first order spin i precesses at the mean-field rate $r_i\cos\theta$ [the phase $tr_i\cos\theta$ of $\langle\sigma_i^+\rangle_t$ above]; differences of these rates between coupled sites drive the second-order density change. To second order in t, charge flows from site i when its neighbours have larger row sums ($B_i > 0$) if $\theta < \pi/2$, where the carriers are magnons, and in the opposite direction if $\theta > \pi/2$, where they are holes; at $\theta = \pi/2$ particle–hole symmetry forbids it. The uniform one-magnon superposition is stationary only for equal row sums (all-to-all or periodic couplings), which is why transport is absent there. In the unnormalized coherence, transport appears as the term $B_i\cos^2\theta$ of Eq. (S8), tilt independent as $\theta \to 0$: this is the g of Eq. (2) found in the data. It violates (C1) and lies outside Theorem 1 and Corollary 1: it can be negative, and $\mathcal{D}_s$ with $s^2 < 0$ is a Schur multiplier on the sector blocks, not a channel. The normalization by $p_i(1-p_i)$ removes it exactly at order t^2 and, at zero density, at all times. In an open long-range chain the row sums peak at the centre, so charge flows from the ends to the centre at small tilt. For the 12-ion couplings $S_i/J_0^2 = 1.56$ at the ends and 2.95 at the centre, while $B_i/J_0^2 = 3.78$ and -1.46.

Test on the 12-ion data. The measured intercept is a three-tilt quantity, and the data average $|\langle\sigma_i^+\rangle|$ over ions 4–9 (Sec. S6), so we compare it with $g_0(t) = -\ln\left[\frac{1}{6}\sum_{i=4}^{9}|v_i(t)|\right]$ for the published 12-ion couplings $J_{ij} = J_0/|i-j|$, $J_0 = 560$ rad/s, with no parameter (Table S4). The proper comparator of the measured three-tilt intercept is the three-tilt g of noiseless exact dynamics, which agrees with g_0 within 0.02 up to 1.8 ms and then leaves it (by 0.10 at 2.55 ms), because the order-z terms make the dephasing nonlinear in $\sin^2\theta$. Up to 1.8 ms the measured g agrees with both ($\chi^2 = 7.8$ against g_0 and 6.2 against exact dynamics, 5 times). Up to 2.6 ms, $\chi^2 = 9.6$ against g_0 but 16.5 against exact dynamics (7 times): the later agreement with g_0 is partly a cancellation between this nonlinearity and technical dephasing, which makes the measured g positive after 2.6 ms while the exact one stays negative. We therefore claim agreement only up to 1.8 ms. *Normalized intercept.* If the intercept is transport, it must disappear from the normalized coherence. A three-tilt fit of $\bar{s}_i^2 = \bar{\kappa}^2\sin^2\theta + 2\bar{g}$, with $|\langle\sigma_i^+\rangle|^2$ and p_i of ions 4–9 from the same shadows (U-statistic for $|\langle\sigma_i^+\rangle|^2$, 20-group jackknife), gives $\bar{g}$ consistent with zero at every time up to 2.9 ms (within 1.6σ), while the unnormalized fit of the same ions gives $g = -0.194 \pm 0.060$ at 1.09 ms and -0.235 ± 0.065 at 1.45 ms (Table S3;

script `ion_norm_g.py`). After 1.5 ms $\bar{g}$ trends positive (0.13–0.26), as tilt-blind technical dephasing would make it.

TABLE S3. Three-tilt fits of the single-ion dephasing of ions 4–9 in the 12-ion data: unnormalized (s_i^2, intercept g, slope κ^2) and normalized ($\bar{s}_i^2$, intercept $\bar{g}$, slope $\bar{\kappa}^2$). Errors: 20-group jackknife over unitaries.

t (ms)	g	$\bar{g}$	κ^2	$\bar{\kappa}^2$
0.36	-0.103 ± 0.039	-0.019 ± 0.048	0.32	0.15
0.73	-0.037 ± 0.056	$+0.070 \pm 0.079$	0.45	0.26
1.09	-0.194 ± 0.060	$+0.025 \pm 0.099$	1.22	0.77
1.45	-0.235 ± 0.065	$+0.058 \pm 0.109$	1.76	1.17
1.82	-0.156 ± 0.073	$+0.132 \pm 0.117$	2.08	1.51
2.18	-0.132 ± 0.082	$+0.159 \pm 0.129$	2.68	2.10
2.55	-0.126 ± 0.093	$+0.130 \pm 0.138$	3.46	2.95
2.91	$+0.093 \pm 0.114$	$+0.255 \pm 0.160$	4.05	3.73

TABLE S4. Intercept g of Eq. (7) in the 12-ion data: measured (three-tilt fit), from exact noiseless dynamics (same fit), and the zero-density prediction g_0 of Proposition 3.

t (ms)	g measured	g exact dynamics	g_0 (Prop. 3)
0.36	-0.099 ± 0.035	-0.031	-0.025
0.73	-0.069 ± 0.034	-0.086	-0.085
1.09	-0.193 ± 0.031	-0.161	-0.148
1.45	-0.223 ± 0.042	-0.200	-0.188
1.82	-0.166 ± 0.051	-0.211	-0.193
2.18	-0.112 ± 0.061	-0.212	-0.160
2.55	-0.028 ± 0.061	-0.197	-0.097
2.91	$+0.074 \pm 0.099$	-0.165	-0.031
3.27	$+0.296 \pm 0.121$	-0.216	$+0.004$
3.64	$+0.317 \pm 0.165$	-0.366	-0.019

Low-density expansion. Because H conserves q, the coefficients of z^k in s_i^2 and $\tilde{s}_A^2$ follow exactly from the dynamics of at most $k+2$ magnons: we evolve $|S_q\rangle$ in the q-magnon sectors ($q \le Q$; dimension $\binom{N}{q}$), form $\sum_q z^q \langle S_{q+1}(t)|\sigma_i^+|S_q(t)\rangle$ and ρ_A as power series, and take logarithms and ratios order by order (script `lowdens2.py`). With $Q = 5$ the series reproduces exact 12-ion dynamics at $\theta = 0.2\pi$ ($z = 0.106$) within 0.003 for single ions and 0.02 for blocks up to 2.5 ms (Table S5); at 0.33π ($z = 0.33$) it does not converge. For $N = 51$ ($Q = 4$, sectors up to 2.5×10^5 states) the series is controlled at 0.2π up to about 2.5 ms. Its leading term shows the position dependence directly: at 3 ms, $-\ln|v_i|^2 = -0.41$ on the central ions 16–35 that form the blocks of Fig. 4, +0.47 on ions 6–10, and −0.13 on average over ions 6–46.

TABLE S5. Low-density series at $\theta = 0.2\pi$ for the 12-ion chain, truncated at $Q = 3, 4, 5$ magnons, against exact dynamics: single-ion s_i^2 (ions 4–9) and block $\tilde{s}_A^2$ (15 blocks of four of these ions).

	single ion s_i^2				block $\tilde{s}_A^2$			
t (ms)	exact	$Q = 3$	$Q = 4$	$Q = 5$	exact	$Q = 3$	$Q = 4$	$Q = 5$
0.5	0.010	0.007	0.010	0.010	-0.037	-0.034	-0.031	-0.037
1.0	0.045	0.040	0.045	0.045	-0.054	-0.030	-0.037	-0.057
1.5	0.183	0.180	0.183	0.182	0.027	0.088	0.058	0.013
2.0	0.477	0.462	0.484	0.474	0.221	0.272	0.256	0.210
2.5	0.932	0.915	0.924	0.935	0.582	0.591	0.601	0.581

S5. TRANSPORT AND THE POPULATION-TRACKED ASYMMETRY, EQ. (9)

Exact rewriting. For $\rho \geq 0$ and orthogonal projectors, $\|\Pi_q \rho \Pi_{q'}\|_F^2 \leq \|\Pi_q \rho \Pi_q\|_F \, \|\Pi_{q'} \rho \Pi_{q'}\|_F$. Proof: write $\rho = MM^\dagger$, $X = \Pi_q M$, $Y = \Pi_{q'} M$; then $\|XY^\dagger\|_F^2 = \mathrm{Tr}(X^\dagger X Y^\dagger Y) \leq \|X^\dagger X\|_F \|Y^\dagger Y\|_F = \|XX^\dagger\|_F \|YY^\dagger\|_F$ by the Cauchy–Schwarz inequality for the Hilbert–Schmidt product, with equality for pure ρ. Hence $\gamma_{qq'} = \|\Pi_q \rho_A \Pi_{q'}\|_F^2/(w_q w_{q'}) \in [0,1]$, with $w_q = \|\Pi_q \rho_A \Pi_q\|_F$, and, since the blocks $\Pi_q \rho_A \Pi_{q'}$ are Frobenius-orthogonal,

$$\Delta S_A^{(2)} = \ln \frac{\sum_{q,q'} w_q w_{q'} \gamma_{qq'}}{\sum_q w_q^2} \tag{S10}$$

exactly. A symmetric W preserves every w_q and $\gamma_{qq'}$. The sector weight is $w_q = p_q \, (\mathrm{Tr}\, \hat{\rho}_q^2)^{1/2}$, with $p_q = \mathrm{Tr}\, \Pi_q \rho_A$ and $\hat{\rho}_q$ the normalized sector state, so $w_q = p_q$ when the sector states are pure. Equation (3) is the case $w_q = p_q(0)$, $\gamma_{qq'} = e^{-s^2(q-q')^2}$; Eq. (9) keeps the Gaussian γ and lets the populations move, replacing w_q by the measurable $p_q(t)$. In the 51-ion simulation $w_q/p_q \geq 0.996$ for all sectors and tilts at 3 ms.

Site aggregation in the rule. As specified in `FROZEN_RULE_SPEC.md`, the operational rule first averages the normalized coherences, $C_A(t) = N_A^{-1} \sum_{i \in A} \bar{c}_i^{\,2}(t)$, then forms $-\ln[C_A(t)/C_A(0)]$ and fits its slope and intercept across the three calibration tilts. This is a logarithm of the site mean, not a mean of the site logarithms. The same ordering is used in the experimental, exact-dynamics and 51-ion evaluation scripts.

Environment factor. By Corollary 1, $\kappa^2 \propto N_B$ for collective dephasing, so a block's normalized dephasing is then $(N - N_A)/(N-1)$ times that of a single ion. This is a collective-limit statement; for nonuniform XY couplings we check the factor numerically and do not derive it. At short times the phases of the ions in A are not yet collective, and the ratio is smaller: it starts near the coupling-weighted fraction $f_J = \sum_{i \in A} \sum_{j \notin A} J_{ij}^2 / \sum_{i \in A} S_i$ (numerically) and approaches $(N - N_A)/(N-1)$ as the phase correlations spread (Table S6; script `envfactor.py`). For bulk blocks of the 12-ion chain it is within 15% of $(N - N_A)/(N-1)$ from 1 ms on; for end blocks it reaches it later (at 0.5π, 0.51 at 1 ms for $N_A = 4$). In the 51-ion chain the ratio is 0.69–0.71 at 1 ms, 0.92–0.96 at 2 ms and 0.92–0.93 at 3 ms (medians over 1–3.6 ms: 0.915, 0.933 and 0.934 at 0.2π, 0.33π and 0.5π), against 0.94; the crossings lie at 2.2–3.7 ms. Equation (9) uses $(N - N_A)/(N-1)$ without adjustment.

TABLE S6. Ratio of block to single-ion normalized dephasing, $\bar{s}_A^2/\bar{s}_i^2$ (block: $-\ln \bar{G}_1$; ions: $-\ln[C_A(t)/C_A(0)]$ as defined above), in exact 12-ion dynamics, against the collective value $(N - N_A)/(N-1)$ and the short-time fraction f_J.

block, tilt	$(N - N_A)/(N-1)$	f_J	0.2 ms	0.7 ms	1.0 ms	1.5 ms	2.0 ms	2.5 ms
ions 6–7, 0.2π	0.91	0.66	0.64	0.83	0.90	0.89	0.89	0.90
ions 6–8, 0.2π	0.82	0.49	0.45	0.67	0.78	0.78	0.77	0.80
ions 5–8, 0.2π	0.73	0.39	0.34	0.53	0.64	0.66	0.64	0.68
ions 1–4, 0.2π	0.73	0.26	0.24	0.45	0.61	0.73	0.73	0.70
ions 6–7, 0.5π	0.91	0.66	0.63	0.83	0.92	0.93	0.91	0.93
ions 6–8, 0.5π	0.82	0.49	0.45	0.68	0.83	0.86	0.81	0.84
ions 5–8, 0.5π	0.73	0.39	0.34	0.55	0.72	0.79	0.72	0.75
ions 1–4, 0.5π	0.73	0.26	0.23	0.36	0.51	0.69	0.68	0.58

Population changes alone produce no crossing. Setting $\gamma_{qq'} = 1$ in Eq. (S10), with the block populations $p_q(t)$ of exact 12-ion dynamics (all 19 connected blocks of 3 and 4 ions, three tilt pairs, 0–4 ms) or of the 51-ion TDVP (five central 4-ion blocks), no pair of curves crosses in any of the 57 and 15 cases; the smallest gaps are 0.085 and 0.08 (script `transport_only.py`). Population changes shift the crossings but do not produce them here. We have no proof that this holds for all chains.

Test in exact 12-ion dynamics. For all 57 crossings of connected 3- and 4-ion blocks, we compare four rules built from single-ion quantities of each block's own ions with the exact crossing times (Table S7; script `transport12_exact.py`). Eq. (9) with the environment factor is accurate to 0.10 ms in the bulk; the rule of Proposition 2 with the unnormalized slope, the form tested on the data in Fig. 2, errs by up to 0.41 ms. Without the environment factor, Eq. (9) predicts the crossings too early by 0.12–0.16 ms on average. At the end blocks all rules are late by about 0.2 ms, where the factor is reached later (Table S6).

TABLE S7. Crossing-time errors (ms; exact minus predicted) of single-ion rules in exact 12-ion dynamics, 57 crossings of connected 3- and 4-ion blocks for three tilt pairs; "end": blocks containing ion 1 or 12.

rule	bulk mean	bulk max	end mean	end max
Prop. 2, unnormalized slope κ^2, binomial p_q	-0.02	0.41	-0.24	0.51
Eq. (9), per tilt, factor $(N-N_A)/(N-1)$	$+0.02$	0.10	-0.21	0.33
Eq. (9), one slope $\bar{\kappa}^2 \sin^2\theta$, factor	$+0.05$	0.19	-0.21	0.25
Eq. (9), per tilt, no factor	-0.15	0.55	-0.41	0.50
Eq. (9), one slope, no factor	-0.12	0.54	-0.43	0.55

S6. ANALYSIS OF THE 12-ION DATA

Data. Zenodo 10390690 (CC-BY), associated with Ref. [14]: 12-bit single-shot outcomes for 500 local random unitaries × 50 shots at 16 times (0–8 ms) for $\theta \in \{0.2, 0.33, 0.5\}\pi$, with the applied unitaries. Controls: pure dephasing (interactions off) and 10 disorder realizations, each with 300 unitaries × 30 shots at 9 times. Files were read with `python3 -I`; no downloaded code was executed.

Conventions and estimators. Bits are least-significant-first, $P(b) = \langle b|U\rho U^\dagger|b\rangle$, and the single-qubit shadow is $3U^\dagger|b\rangle\langle b|U - \mathbb{I}$ [15, 16]. These were fixed by the $t = 0$ Bloch vectors, which have $|\vec{r}| = 1.00$. Purities are estimated with the U-statistic over pairs of distinct unitaries [17], which removes shot-noise bias. *Validation:* the estimator reproduces all 48 published values of $\Delta S_A^{(2)}$ (averaged over the 15 four-site subsystems of the central six ions) within 1σ; the largest deviation is 0.95σ and the median 0.29σ.

$\kappa^2(t)$ and $g(t)$. The single-site $m_\perp(t)$ is averaged over the central ions; jackknife errors over unitaries are used. At each time, Eq. (7) is fitted to the three tilts by weighted least squares, giving $\kappa^2(t)$, $g(t)$ and their covariance. Weighted residuals are at the noise level (χ^2 per time with one degree of freedom is below 3 except at 0.73 and 2.55 ms). Between 1 and 3.6 ms, $\kappa^2 \propto t^{1.25\pm0.06}$. Beyond 3.6 ms, $m_\perp$ at $\theta = \pi/2$ is below 4% of its initial value and within 3σ of zero after 5 ms, so κ^2 is limited by noise; the measured g lies between -0.22 and 0.32 up to 3.6 ms. Its negative values at 1–2 ms (up to 6σ) cannot be a dephasing variance, but they are intrinsic: the same three-tilt fit applied to noiseless exact dynamics of the 12-ion model ($J_0 = 560$ rad/s, $\alpha = 1$) gives $g = -0.15$, -0.20, -0.21 and -0.20 at 1.0, 1.5, 2.0 and 2.5 ms, with residuals below 0.02. The coherent dynamics thus add a negative, tilt-independent offset to the linear $\sin^2\theta$ form: by Proposition 3 it is magnon transport, and it disappears from the normalized coherence (Table S3). The threshold test of Fig. 2 sets $g = 0$ in Eq. (3).

Crossings. Asymmetry differences are interpolated linearly in t at their sign change, and κ^2 at that time is interpolated from the fit. The crossing time and $\kappa^2(t)$ come from the same shots, so their errors are not independent. We therefore resample them jointly: every jackknife replicate (20 unitary groups) recomputes the asymmetries, the crossing time, $m_\perp(t)$ and the weighted fit (weights fixed at their full-sample values), and the error of the residual $\kappa^2(t_\times) - \kappa_*^2$ is the jackknife error of that residual (scripts `groupstats12.py`, `stats12.py`, which reproduce the separate jackknife estimates to 3×10^{-15}). With these errors (0.07–0.22) all nine residuals lie within 1.6σ and six within 1σ; their χ^2 is 7.8 for nine points, descriptive because the nine crossings share shots. The crossing-time errors are 0.04–0.19 ms. Errors from the fit covariance of κ^2 alone give five within 1σ, all within 2.3σ and $\chi^2 = 18.8$; that statistic omits the crossing-time uncertainty and the covariance. Linear interpolation on the 0.36-ms grid shifts crossings by at most 0.04 ms in exact dynamics. Table S8 lists the nine crossings.

Block sector weights. Let $F_n = \sum_{|q-q'|=n} \|\Pi_q \rho_A \Pi_{q'}\|_F^2$. The blocks $\Pi_q \rho_A \Pi_{q'}$ are Frobenius-orthogonal, so $\mathrm{Tr}\,\rho_A^2 = \sum_n F_n$, $\mathrm{Tr}(\mathcal{P}\rho_A)^2 = F_0$ and $\Delta S_A^{(2)} = \ln \sum_n F_n/F_0$ exactly; a symmetric W preserves every F_n. For any pure initial state $F_n(0)/F_0(0) = \sum_{|q-q'|=n} p_q p_{q'} / \sum_q p_q^2$. Hence, if $R_n \equiv [F_n/F_0]_t/[F_n/F_0]_0 = e^{-n^2\tilde{s}^2}$, Eq. (3) holds with $s \to \tilde{s}$ whether or not F_0 is conserved, and so does Proposition 2 if $\tilde{s}^2 = \tilde{\kappa}_A^2 \sin^2\theta + 2\tilde{g}_A$ with one $\tilde{\kappa}_A$ for both tilts. This condition is sufficient, not necessary, and concerns the Rényi-2 asymmetry only. We estimate F_0, F_1, F_2 for all blocks of $N_A = 2, 3, 4$ of the central six ions with the U-statistic over unitaries (10-group jackknife) and fit $-\ln R_1 = \tilde{\kappa}_A^2 \sin^2\theta + 2\tilde{g}_A$ across the three tilts at each time (scripts `block_sectors.py`, `block_sectors_fit.py`, `block_sectors_summary.py`). Sectors with $n \geq 3$ are not estimated; in the model they carry at most 0.3% of $\sum_n F_n$ at the $N_A = 4$ thresholds. The normalization uses the measured $t = 0$ state, which lies 3–5% below the pure-state asymmetries. Results (Table S9):

(i) F_0 is not conserved. At fixed p_q, Cauchy–Schwarz gives $\|\Pi_q \rho_A \Pi_q\|_F^2 \geq p_q^2/\binom{N_A}{q}$, so decoherence within sectors alone can lower F_0 at $\theta = 0.2\pi$ only to 0.98 ($N_A = 2$), 0.94 ($N_A = 3$) and 0.88 ($N_A = 4$) of its initial value. The

TABLE S8. The nine Mpemba crossings in the 12-ion data. $t_\times$: observed crossing time, with its jackknife error; $\kappa^2(t_\times)$: measured (error from the fit covariance alone); κ^2_*: prediction of Proposition 2 from the exact model curves and from Eq. (4); z: residual $\kappa^2(t_\times) - \kappa^2_*$ (exact) divided by its joint jackknife error, which resamples $\kappa^2(t)$ and the crossing time together; $\tilde\kappa^2_A(t_\times)$: the block's own dephasing from the sector ratio F_1/F_0, interpolated to $t_\times$. With the joint errors all nine crossings lie within 1.6σ of the exact threshold and six within 1σ ($\chi^2 = 7.8$ for 9 points, descriptive). With $\tilde\kappa^2_A$, five within 1σ and eight within 2σ (maximum 2.4σ); the ratio $\tilde\kappa^2_A/\kappa^2_*$ is 0.64–1.09, mean 0.92. $t_\times^{\rm sec}$: crossing of Eq. (3) evaluated with the block's own per-tilt $\tilde s^2 = -\ln R_1$, no fit; it agrees with $t_\times$ within 0.07 ms (mean −0.02 ms; jackknife errors 0.01–0.26 ms).

N_A	pair	$t_\times$ (ms)	$\kappa^2(t_\times)$	κ^2_* exact	κ^2_* closed	z (joint)	$\tilde\kappa^2_A(t_\times)$	$t_\times^{\rm sec}$ (ms)
2	0.5π vs 0.2π	1.50 ± 0.08	1.77 ± 0.10	1.80	1.81	−0.28	1.84 ± 0.09	1.43
2	0.5π vs 0.33π	0.93 ± 0.18	0.90 ± 0.08	1.08	1.10	−0.55	0.91 ± 0.13	0.92
2	0.33π vs 0.2π	1.88 ± 0.11	2.20 ± 0.12	2.26	2.27	−0.40	2.30 ± 0.09	1.81
3	0.5π vs 0.2π	1.27 ± 0.04	1.47 ± 0.09	1.39	1.41	+0.72	1.46 ± 0.10	1.27
3	0.5π vs 0.33π	0.68 ± 0.05	0.49 ± 0.08	0.64	0.67	−1.59	0.41 ± 0.15	0.69
3	0.33π vs 0.2π	1.41 ± 0.08	1.67 ± 0.10	1.88	1.91	−1.43	1.65 ± 0.10	1.38
4	0.5π vs 0.2π	1.12 ± 0.05	1.25 ± 0.08	1.09	1.13	+1.37	1.19 ± 0.12	1.15
4	0.5π vs 0.33π	0.61 ± 0.06	0.45 ± 0.08	0.43	0.45	+0.21	0.37 ± 0.14	0.58
4	0.33π vs 0.2π	1.27 ± 0.07	1.47 ± 0.09	1.53	1.58	−0.48	1.37 ± 0.12	1.28

measured minima are lower (Table S9), so most of the loss is a drift of the charge distribution p_q: charge exchange across the boundary, which violates (C1), or population errors. A per-tilt trace of $\langle n_i\rangle(t)$ would separate the two. Exact dynamics (0.86 at 0.2π, $N_A = 4$) also require some drift of p_q.

(ii) The ratios are close to Gaussian in n. Over the 32 tilt–time–block-size points with $0.2 < R_1 < 0.8$, $\ln R_2/\ln R_1$ has mean 4.08, median 3.82 and standard deviation 1.3 (range 1.8–8.3); per block size the means are 4.6, 3.8 and 3.9 for $N_A = 2, 3, 4$. Eq. (2) gives 4. The points share ions and shots, so we quote no error on the mean. At 0.2π the ratio drifts from 6–8 at $R_1 > 0.6$ to 2–3 later.

(iii) The three-tilt form holds only approximately for blocks: the intercepts are $\tilde g_A = -0.26 \pm 0.02$, -0.25 ± 0.02 and -0.24 ± 0.02 (1.1–2.2 ms, $N_A = 2, 3, 4$), negative like the single-site g and therefore not a variance, and $\sum\chi^2 = 10.6$, 16.0 and 16.1 for 7 degrees of freedom over 1.1–3.3 ms (maximum 5.5 at one time). $\tilde\kappa^2_A$ is thus an effective slope.

(iv) The block slope $\tilde\kappa^2_A$ equals the single-ion κ^2 (same estimator, $N_A = 1$) within 6%, while the absolute weight F_1 alone gives ratios close to the environment-size factor $(N - N_A)/(N - 1)$ of Eq. (6). Exactly, $\tilde\kappa^2_A - \kappa^2_{A,F_1}$ is the $\sin^2\theta$ slope of $-\ln[F_0(t)/F_0(0)]$: the tilt-dependent loss of F_0 offsets the smaller environment of the block. The identity explains which quantity sets the asymmetry. Section S5 separates the two effects: the smaller environment is the factor $(N - N_A)/(N - 1)$ of the normalized dephasing, and the loss of F_0 is the transport-driven drift of p_q (Proposition 3); that they nearly cancel in the unnormalized slope for 12 ions is not general, and it fails at 51 ions (Sec. S11). Exact dynamics of the 12-ion model (Sec. S10, benchmark) show the same compensation: $\tilde\kappa^2_A/\kappa^2 = 0.89$ and $\kappa^2_{A,F_1}/\kappa^2 = 0.75$ for $N_A = 4$ over 0.9–2.6 ms, and F_0 falls to 0.86, 0.97 and 1.00 of its initial value at 0.2π, 0.33π and 0.5π. In exact dynamics the threshold rule with the single-ion κ^2 reproduces the three $N_A = 4$ crossing times within 0.12 ms.

(v) What sets the crossing. Evaluating Eq. (3) of the Letter with the measured $\tilde s^2(\theta, t) = -\ln R_1$ of each block and tilt, without any fit, gives the nine crossing times of Table S8 within 0.07 ms (column $t_\times^{\rm sec}$; script `sector_model_crossings.py`); the ratio F_1/F_0 alone, through $\ln(1 + F_1/F_0)$, gives them within 0.05 ms, and in exact 12-ion dynamics within 0.06 ms. At these times the asymmetry is dominated by the $n = 1$ sector, so this agreement is close to an identity: it shows that the crossing is fixed by the block's own F_1/F_0, but it tests neither the n^2 law nor a threshold. The threshold content of Proposition 2 is that one slope $\tilde\kappa^2_A$ describes all tilts; for 12 ions it does (Table S8, eight of nine within 2σ), and the single-ion κ^2 is a good proxy for it because $\tilde\kappa^2_A \approx \kappa^2$.

Controls (Fig. S1). Under pure dephasing $\kappa^2 = 0.0 \pm 0.2$ at all times up to 8 ms, and the three tilts decay at the same rate ($\ln m_\perp$ ratios −0.35, −0.36, −0.38 at 8 ms). The 10 disorder realizations split into two groups by decay rate, which we identify with the weak and strong disorder of Ref. [14]. The files carry no labels, so this assignment is provisional: it uses the decay rate, which is part of what is being interpreted, and we have no independent label source. Disorder runs exist at two tilts (0.2π, 0.5π), so κ^2 and g are determined without a third-tilt test of Eq. (7). Weak disorder: κ^2 exceeds 3 after 3 ms (maximum 4.9 ± 0.5) and the curves cross between 1 and 2 ms. Strong disorder: $\kappa^2 \le 1.8 \pm 0.6$ up to 8 ms; it reaches the threshold 1.09 from about 2 ms on, yet the curves do not cross within 8 ms. This is within errors (1.2σ) but in mild tension with Proposition 2, and it is not a sharp test of it.

TABLE S9. Block sector weights in the 12-ion data. $F_0^{\min}$: minimum of $F_0(t)/F_0(0)$ for $t \le 2.2$ ms at $\theta = 0.2\pi$, 0.33π, 0.5π (lower bound at fixed p_q for 0.2π: 0.98, 0.94, 0.88 for $N_A = 2, 3, 4$). $\tilde{\kappa}_A^2/\kappa^2$: block dephasing from F_1/F_0 over the single-ion value; $\kappa_{A,F_1}^2/\kappa^2$: same from F_1 alone; both weighted means over 1.1–3.3 ms. Last column: environment-size factor of Eq. (6).

N_A	$F_0^{\min}$ $(0.2\pi/0.33\pi/0.5\pi)$	$\tilde{\kappa}_A^2/\kappa^2$	$\kappa_{A,F_1}^2/\kappa^2$	$(N-N_A)/(N-1)$
2	0.81/0.89/0.98	1.04 ± 0.03	0.93 ± 0.03	0.91
3	0.76/0.89/0.97	0.99 ± 0.03	0.85 ± 0.03	0.82
4	0.73/0.90/0.97	0.94 ± 0.03	0.76 ± 0.04	0.73

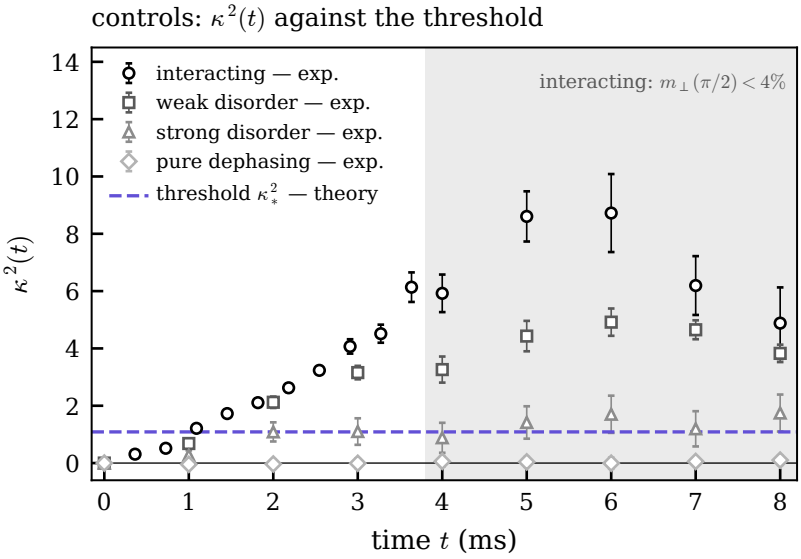


FIG. S1. Controls of the 12-ion experiment [14] (raw data): $\kappa^2(t)$ from Eq. (7) for the interacting runs (three tilts), weak and strong disorder (two tilts each) and pure dephasing (interactions off). Dashed: $N_A = 4$ threshold for 0.5π versus 0.2π. Shaded: interacting $m_\perp(\pi/2) < 4\%$ of its initial value, where κ^2 is noise-limited.

How well (C1)–(C3) hold. (C1): the total-variation drift of the 4-site charge distribution $p_q(t)$ from $p_q(0)$ stays below 0.10 in exact dynamics of the 12-ion XY model ($J_0 = 560$ rad/s, $\alpha = 1$) and below 0.16 in the raw data, a value that still contains shot noise. Overall: the fidelity of Eq. (2) to the exact reduced states is 0.89–0.99 up to 5 ms. Phase spreading: the measured κ^2 grows as $t^{1.25}$ after 1 ms (exact dynamics: $t^{1.63}$), slower than the ballistic growth of Corollary S1. Because Eq. (2) keeps the block-diagonal part of ρ_A fixed, it underestimates the magnitude of $\Delta S_A^{(2)}$ by 10–30% at intermediate times; the crossing condition is much less sensitive (Table S8). The measured $t = 0$ asymmetries lie 3–5% below the pure-state values used in Eq. (3).

S7. POSITION-RESOLVED ANALYSIS OF THE 12-ION DATA

Estimators. For every ion, $|\langle\sigma_i^+\rangle|^2$ is estimated without noise bias by the U-statistic over the 500 random unitaries of the single-ion shadows, $m_i^2 = (|\sum_r \vec{v}_r|^2 - \sum_r |\vec{v}_r|^2)/[N_U(N_U-1)]$ with $\vec{v}_r$ the shot-averaged $(\langle\sigma^x\rangle, \langle\sigma^y\rangle)$ of unitary r, and $s_i^2 = -\ln[m_i^2(t)/m_i^2(0)]$. The Rényi-2 asymmetries of all connected blocks of 3 and 4 ions use the U-statistic purities of Sec. S6. Errors are 20-group jackknife errors over unitaries, propagated through every derived quantity, including crossing times (scripts `ion_resolved.py`, `ion_jack.py`). Exact noiseless dynamics use $J_{ij} = J_0/|i-j|$, $J_0 = 560$ rad/s, for all 12 ions (`ion_theory.py`).

Edge-bulk contrast. Table S10 and Fig. 3(b): the end ions dephase more than the bulk ions at 0.2π and 0.33π and less at 0.5π, as Eq. (S8) predicts (crossover near $\sin^2\theta \approx 0.8$). Eq. (S8) agrees with exact dynamics up to about 0.7 ms. At 0.2π the measured contrast exceeds the exact one by 2.5σ at 1.09 ms: the end ions of the experiment dephase faster than the ideal model. The individual ions also show a left–right asymmetry (ions 3 and 4 dephase faster than ions 9 and 10 at 0.2π), which the model cannot produce; we therefore average the two ends and the four central ions

TABLE S10. Edge-minus-bulk single-ion dephasing in the 12-ion data, $s^2_{\rm edge} - s^2_{\rm bulk}$ (ions 1, 12 minus ions 5–8): experiment (raw data, jackknife error), exact noiseless dynamics and the short-time law, Eq. (S8); no fit parameter.

	$t = 0.36$ ms			$t = 0.73$ ms			$t = 1.09$ ms			$t = 1.45$ ms		
θ	exp.	exact	(S8)	exp.	exact	(S8)	exp.	exact	(S8)	exp.	exact	(S8)
0.2π	$+0.31 \pm 0.07$	$+0.12$	$+0.12$	$+0.64 \pm 0.11$	$+0.49$	$+0.48$	$+1.47 \pm 0.17$	$+1.05$	$+1.09$	$+2.24 \pm 0.30$	$+1.50$	$+1.93$
0.33π	$+0.05 \pm 0.03$	$+0.02$	$+0.01$	$+0.09 \pm 0.06$	$+0.11$	$+0.05$	$+0.38 \pm 0.08$	$+0.30$	$+0.12$	$+0.81 \pm 0.08$	$+0.54$	$+0.21$
0.5π	-0.07 ± 0.02	-0.05	-0.06	-0.19 ± 0.03	-0.14	-0.23	-0.21 ± 0.03	-0.17	-0.52	-0.18 ± 0.05	-0.12	-0.92

(script `ion_profile.py`). Whether the extra edge dephasing and the left–right asymmetry come from the real coupling matrix, which is not published beyond the power-law form, or from position-dependent technical noise remains open.

Transport, ion by ion. The single-ion density $p_i = \langle n_i \rangle$ comes from the same shadows (unbiased; 20-group jackknife; scripts `ion_P.py`, `ion_density.py`). At 1.09 ms the end ions (1, 12) keep $p_i/p_i(0) = 0.51 \pm 0.07$, 0.70 ± 0.02 and 0.92 ± 0.01 at 0.2π, 0.33π and 0.5π, and the central ions 5–8 reach 1.44 ± 0.11, 1.17 ± 0.03 and 1.02 ± 0.01; exact dynamics give 0.40, 0.66, 1.00 and 1.26, 1.12, 1.00 [Fig. 3(a)]. The loss of the end ions at 0.5π, where Proposition 3 forbids transport, is a technical effect; it is also present before 1 ms (0.98 ± 0.01 at 0.73 ms). Removing transport by normalization removes most of the edge excess of the dephasing [Fig. 3(b)]: at 1.09 ms the edge-minus-bulk $\bar{s}^2$ is $+0.54 \pm 0.28$, $+0.02 \pm 0.09$ and -0.22 ± 0.03 at the three tilts, against s^2 of $+1.47 \pm 0.17$, $+0.38 \pm 0.08$ and -0.21 ± 0.03 (exact: $\bar{s}^2$ $+0.03$, -0.07, -0.17; s^2 $+1.08$, $+0.31$, -0.17). The residual $+0.54 \pm 0.28$ at 0.2π (1.9σ) is the excess edge dephasing of the experiment beyond the model (script `fig3_transport.py` prints these numbers). *Technical effects against transport.* Transport changes the density in proportion to $(1 - p_0)\cos\theta$ at short times, and it vanishes at $\pi/2$. A weighted fit of the measured relative density change at 1.09 ms over the three tilts to $a\,\Delta_{\rm exact}(\theta) + c$ gives, for the end ions, $a = 0.67 \pm 0.06$ and $c = -0.080 \pm 0.010$ ($\chi^2 = 0.05$, one degree of freedom), and for the central ions $a = 1.34 \pm 0.23$ and $c = +0.019 \pm 0.010$ ($\chi^2 = 0.6$). The tilt dependence is that of transport, but its amplitude deviates from the ideal model in a position-dependent way (weaker at the ends, stronger at the centre), on top of a tilt-blind loss at the ends. Together with the excess normalized dephasing of the end ions, these are position-dependent effects of the experiment that the model lacks. Already at 0.36 ms the central ions gain more than in the model (1.15 ± 0.04 against 1.03 at 0.2π).

Crossing times by position. For each connected block, the three-tilt fit of Eq. (7) to the mean $m_\perp$ of the block's own ions gives $\kappa^2_A(t)$; times at which any tilt has $m_\perp < 0.08$ are excluded. The predicted crossing is the time at which κ^2_A reaches the exact root κ^2_* of Proposition 2 for that block size and tilt pair, with $g = 0$ (scripts `ion_predict.py`, `ion_stats.py`). Tables S13 and S14 list all 56 crossings. A prediction exists when κ^2_A reaches the threshold while all three tilts are above the floor; for one end block ($0.33\pi/0.2\pi$, ions 1–3) it does not, and for its neighbour one jackknife replicate does not, so 54 points enter the statistics: $\chi^2 = 60.7$ (38 within 1σ, 50 within 2σ). In the bulk (44 points), $\chi^2 = 43.9$ and the mean deviation is 0.00 ms; at the end blocks (10 points) the measured crossings lie on average 0.7 ms later than predicted, 9 within 2σ, so the rule captures most but not all of the edge delay (for the 3-ion pair $0.5\pi/0.2\pi$, edge-to-centre ratio 3.0 measured, 2.3 predicted, 1.9 exact). The floor matters little: with $m_\perp > 0.05$ all 56 points have predictions and $\chi^2 = 61.3$; with $m_\perp > 0.12$, 52 points give $\chi^2 = 56.4$. Exact noiseless dynamics, compared with the data errors only, give $\chi^2 = 206$ for 56 points ($\chi^2 = 145$ for the 11 end blocks, mean deviation 0.9 ms). Using Eq. (3) with the per-tilt dephasing of the block's own ions instead gives $\chi^2 = 74.3$ for 55 points. These χ^2 add the errors of prediction and measurement in quadrature. The points are correlated: overlapping blocks share ions, and prediction and measurement come from the same shots; with the joint resampling of the paragraph "Statistics with shared shots" below, $\chi^2 = 86.2$ for the same 54 points. Both are descriptive. The rule uses no parameter fitted to the asymmetries; it is a test of Proposition 2 with position-resolved κ^2.

Population-tracked prediction, Eq. (9). With the measured block populations $p_q(t)$ (diagonal of the block shadows) and $\bar{s}^2_A = \bar{s}^2_i (N - N_A)/(N - 1)$, $\bar{s}^2_i$ the normalized dephasing of the block's own ions per tilt (same floor $m_\perp > 0.08$), Eq. (9) gives the rows "Eq. (9)" of Tables S13 and S14 (script `ion_transport.py`). With one three-tilt slope and no intercept ($\bar{s}^2_i = \bar{\kappa}^2 \sin^2\theta$), the predicted crossings come early ($\chi^2 = 174$ for 56 points; bulk $+0.21$ ms, end blocks $+1.28$ ms): the normalized dephasing of the data acquires a positive tilt-blind intercept after 1.5 ms (Table S3), which a slope without intercept absorbs. The statistics of all rules are in the paragraph "Statistics with shared shots".

Threshold form with intercept. The law, Eq. (2), has a tilt-blind intercept, and Proposition 2 allows a fixed $g \geq 0$. With a three-tilt fit $\bar{s}^2_i = \bar{\kappa}^2 \sin^2\theta + 2\bar{g}$ per time and block, used as $\bar{s}^2_A = (\bar{\kappa}^2 \sin^2\theta + 2\bar{g})(N - N_A)/(N - 1)$ in Eq. (9), we obtain the rule of the Letter, which the held-out validation (Sec. S12) tests with this specification frozen (script `ion_transport_c9.py`). Its inputs are measured block populations and single-ion coherences; its slope and intercept

are fitted to the single-ion data, not to asymmetries or crossing times.

Statistics with shared shots. The measured crossings and all predictions are computed from the same shots. We therefore rebuild every estimator (block asymmetries, block populations, single-ion coherences and densities) from sums over the 20 groups of random unitaries (script `groupstats12.py`), which reproduces the separate estimates and their jackknife replicates to 3×10^{-15}, and resample measurement and prediction together (script `stats12.py`). Table S11 summarizes the results. (i) For each point the error of the difference (measured minus predicted crossing time) is the jackknife error of that difference. Adding the separate errors in quadrature ignores their positive covariance and understates the scatter: the threshold form gives $\chi^2 = 53.6$ for 51 points with quadrature errors and 82.6 with joint errors; Eq. (9) per tilt 59.2 and 91.9 (51 points); the simplest rule 60.7 and 86.2 (54 points). Overlapping blocks share ions and shots, so these χ^2 are descriptive. (ii) Stratum means of the difference, with the jackknife error of the stratum mean, which keeps the dependence between points: threshold form $+0.09 \pm 0.11$ ms in the bulk (44 points) and $+0.79 \pm 0.49$ ms at the end blocks (7); per tilt $+0.15 \pm 0.09$ and $+0.54 \pm 0.38$; simplest rule 0.00 ± 0.07 and $+0.74 \pm 0.37$ (10). Stratified by tilt pair and block size (Table S11), bulk biases range from -0.21 ± 0.07 ms (simplest rule, 3-ion blocks, $0.5\pi/0.33\pi$) to $+0.30 \pm 0.10$ ms (threshold form, 4-ion blocks, $0.33\pi/0.2\pi$). (iii) On the 50 points defined for both, the mean $|\Delta t|$ of the threshold form exceeds that of the simplest rule by 0.01 ± 0.05 ms (bulk 0.03 ± 0.05, end blocks -0.11 ± 0.24): the 12-ion data do not distinguish the rules. (iv) Censoring. All 57 intended crossings (19 blocks, three pairs) exist in the full sample for the measurement and both forms of Eq. (9); the simplest rule gives no crossing for the end block of ions 1–3 at $0.33\pi/0.2\pi$ (56 points). Six points have jackknife replicates without a predicted crossing for the threshold form (20 replicates in all), and two for the simplest rule (3 replicates); all but one are end blocks, the measurement lacks a crossing in 2 replicates of one end block. Stratum statistics use the points defined in every replicate (51 and 54), so 5 of the 12 end blocks drop out of the threshold-form end stratum; its mean is the least reliable number of the table. (v) Cross-fit. With all inputs (block populations, single-ion coherences and densities) from the even-numbered unitary groups and the asymmetries from the odd ones, and vice versa, the threshold form gives bulk mean deviations of $+0.28$ and -0.06 ms (median $|\Delta t| = 0.30$ and 0.28 ms, against 0.23 and 0.20 ms with inputs and asymmetries from the same half) and end-block lags of $+0.88$ and $+0.66$ ms. A split-sample test of the simplest rule alone gives bulk $+0.02$ ms and median $|\Delta t| = 0.21$ ms.

TABLE S11. Measured minus predicted crossing times (ms) in the raw 12-ion data, by block size N_A, tilt pair and position, with jackknife errors of the stratum mean (20 unitary groups; measurement and prediction resampled together) and the number of points (defined in every replicate). Threshold form: Eq. (9) with a three-tilt slope and intercept (the rule of the Letter); per tilt: Eq. (9) with the per-tilt dephasing; simplest: Proposition 2 with the unnormalized slope of the block's own ions. Last row: χ^2 with errors in quadrature and with joint errors (number of points); both descriptive.

N_A	pair	position	threshold form	per tilt	simplest
3	$0.5\pi/0.2\pi$	bulk	$+0.08 \pm 0.29$ (8)	$+0.08 \pm 0.30$ (8)	$+0.14 \pm 0.12$ (8)
3	$0.5\pi/0.2\pi$	end	$+0.40 \pm 0.29$ (1)	$+0.35 \pm 0.25$ (1)	$+0.61 \pm 0.17$ (2)
3	$0.5\pi/0.33\pi$	bulk	-0.14 ± 0.16 (8)	$+0.03 \pm 0.10$ (8)	-0.21 ± 0.07 (8)
3	$0.5\pi/0.33\pi$	end	$+1.32 \pm 1.31$ (2)	$+0.10 \pm 1.96$ (1)	$+1.26 \pm 1.51$ (2)
3	$0.33\pi/0.2\pi$	bulk	$+0.13 \pm 0.10$ (7)	$+0.20 \pm 0.10$ (7)	-0.11 ± 0.13 (7)
3	$0.33\pi/0.2\pi$	end	—	$+0.66 \pm 0.14$ (1)	$+0.30 \pm 0.26$ (1)
4	$0.5\pi/0.2\pi$	bulk	$+0.21 \pm 0.15$ (7)	$+0.21 \pm 0.15$ (7)	$+0.18 \pm 0.13$ (7)
4	$0.5\pi/0.2\pi$	end	$+0.34 \pm 0.26$ (2)	$+0.32 \pm 0.27$ (2)	$+0.59 \pm 0.26$ (2)
4	$0.5\pi/0.33\pi$	bulk	-0.01 ± 0.18 (7)	$+0.07 \pm 0.11$ (7)	-0.07 ± 0.12 (7)
4	$0.5\pi/0.33\pi$	end	$+1.26 \pm 1.26$ (1)	$+1.23 \pm 1.88$ (1)	$+1.42 \pm 1.27$ (1)
4	$0.33\pi/0.2\pi$	bulk	$+0.30 \pm 0.10$ (7)	$+0.31 \pm 0.12$ (7)	$+0.08 \pm 0.10$ (7)
4	$0.33\pi/0.2\pi$	end	$+0.56 \pm 0.71$ (1)	$+0.77 \pm 0.70$ (1)	$+0.40 \pm 0.33$ (2)
all	all	bulk	$+0.09 \pm 0.11$ (44)	$+0.15 \pm 0.09$ (44)	-0.00 ± 0.07 (44)
all	all	end	$+0.79 \pm 0.49$ (7)	$+0.54 \pm 0.38$ (7)	$+0.74 \pm 0.37$ (10)
all	all	all	$+0.19 \pm 0.09$ (51)	$+0.20 \pm 0.10$ (51)	$+0.14 \pm 0.09$ (54)
χ^2 quadrature / joint			53.6 / 82.6 (51)	59.2 / 91.9 (51)	60.7 / 86.2 (54)

Biases and robustness. A near-zero pooled mean can hide tilt-pair biases (Table S11). The end-block deviations of the simplest rule are all positive (10 of 10; a sign test would give $p \approx 0.002$ only for independent points, which overlapping blocks are not). Linear interpolation on the 0.36-ms time grid shifts crossing times by 0.01 ms (median) and at most 0.04 ms, from exact curves sampled on the experimental grid; the floor $m_\perp > 0.08$ changes the simplest-rule

χ^2 (quadrature convention) between 56.4 and 61.3 for floors 0.12 and 0.05.

Null models. Rules that use the single-ion decay without its tilt structure, with one constant per block size and tilt pair calibrated on the central blocks (ions 3–10), do not reproduce the edge delay: (N1) the time at which the single-ion dephasing at the higher tilt reaches the calibrated value, and (N2) the same for the dephasing averaged over the three tilts, give edge-to-centre ratios 1.0 and 0.7 (measured 3.0) and $\chi^2 = 1087$ and 1240 for 56 points (script `ion_null.py`). The edge delay requires the tilt structure of the single-ion decay, which carries the transport term of Proposition 3.

Causal check of transport. With an on-site field $\sum_i h_i n_i$, the computation in the proof of Proposition 3(a) gives $\ddot{p}_i(0) \propto \sum_j J_{ij}[\cos\theta(r_i - r_j) + (h_i - h_j)]$: in mean field, spin i precesses at the rate $r_i \cos\theta + h_i$, and transport is driven by differences of these rates. Two interventions follow. The tilt-matched field $h_i = -r_i \cos\theta$ removes transport at order t^2 for each tilt and keeps S_i, but it differs between the two preparations, which then evolve under different Hamiltonians. The single-Hamiltonian field $h_i = -r_i$, the same for both preparations, overcompensates at finite tilt and reverses transport (end-ion densities 1.17, 1.36 and 1.43 at 1.09 ms for the three tilts). In exact 12-ion dynamics (script `field_check.py`, Table S12): the tilt-matched field keeps the end and central densities within 0.1% and 0.6% of their initial values at 1.09 ms, and the 3-ion crossings at $0.5\pi/0.2\pi$ move from 2.28 to 1.66 ms at the ends and from 1.19 to 1.56 ms at the centre; with the single-Hamiltonian field the end blocks cross first for $0.5\pi/0.2\pi$ (1.48 ms against 1.66 ms at the centre); for $0.33\pi/0.2\pi$ they remain later (2.10 ms against 2.00 ms). Keeping S_i fixes the dephasing only at order t^2. At finite times the tilt-matched field also lowers the normalized dephasing of the end ions at 0.2π by 23% (central ions 12%) over 1–2.5 ms, and the single-Hamiltonian field by 28% (13%). To separate the two effects we evaluate the exact-coherence level of Eq. (9) (block populations and the Gaussian kernel with the block's own $\bar{s}_b^2$, which reproduces the exact crossings within 0.01 ms) with populations from one run and dephasing from the other. For the end block at $0.5\pi/0.2\pi$, the tilt-matched populations alone move the crossing by -0.43 ms, the tilt-matched dephasing alone by -0.16 ms, both by -0.63 ms; the populations alone remove 74% of the model's end-minus-centre delay (0.28 of 1.08 ms remains), the dephasing change alone 16%. For $0.33\pi/0.2\pi$: 70% and 7%. With the single-Hamiltonian field the populations alone reverse the delay (end block 1.64 ms, centre 1.70 ms). Transport therefore causes about three quarters of the ideal-model edge delay, and the finite-time change of the dephasing most of the rest; we do not assign a larger fraction. The model's edge delay is about half of the measured one (Sec. S7, Tables S13 and S14), so these fractions refer to the model, not to the measured delay.

TABLE S12. Compensating fields in exact 12-ion dynamics: crossing times (ms) of the end (ions 1–3) and central (ions 5–7) 3-ion blocks and their difference, from the exact-coherence level of Eq. (9) (block populations, Gaussian kernel with the block's own $\bar{s}_b^2$) with populations and dephasing taken from the run with or without the field. "populations only": field-run populations, field-free dephasing; "dephasing only": the reverse.

field	field effect kept	$0.5\pi/0.2\pi$: end	centre	delay	$0.33\pi/0.2\pi$: end	centre	delay
$h_i = -r_i \cos\theta$	none	2.28	1.20	+1.08	2.45	1.47	+0.98
	dephasing only	2.11	1.21	+0.91	2.40	1.48	+0.92
	populations only	1.85	1.57	+0.28	2.20	1.91	+0.30
	both	1.65	1.56	+0.09	2.11	1.94	+0.18
$h_i = -r_i$	none	2.28	1.20	+1.08	2.45	1.47	+0.98
	dephasing only	1.97	1.21	+0.76	2.43	1.50	+0.93
	populations only	1.64	1.70	-0.06	2.11	1.94	+0.17
	both	1.47	1.66	-0.19	2.09	2.01	+0.08

S8. SITE-RESOLVED RECORDS: THEOREM S1 AND GAUSSIAN CLOSURE

Let A be a block of k sites with local charges $n_i \in \{0, 1\}$ and extremal configurations $|0_A\rangle$, $|1_A\rangle$ (all down, all up), which span the $\Delta q = k$ coherence. The top-order coherence is $c_A(t) = |\langle 1_A|\rho_A(t)|0_A\rangle|/|\langle 1_A|\rho_A(0)|0_A\rangle| = |\langle \prod_{i\in A} \sigma_i^+\rangle_t|/|\langle \prod_{i\in A} \sigma_i^+\rangle_0|$; single sites give $c_{\{i\}} = m_\perp^{(i)}(t)/m_\perp^{(i)}(0)$.

Theorem S1. *Assume (C1′): U maps $|x_A\rangle \otimes \mathcal{H}_B$ into itself for $x = 0, 1$, so that $U(|0_A\rangle \otimes |e\rangle) = |0_A\rangle \otimes |e_\downarrow\rangle$ and $U(|1_A\rangle \otimes |e\rangle) = |1_A\rangle \otimes |e_\uparrow\rangle$. Then exactly $c_A(t) = |\langle e_\downarrow|e_\uparrow\rangle|$. If moreover $H = H_A + H_B + \sum_{i\in A} n_i \otimes K_i$ with $[H_A, Q_A] = [K_i, K_j] = [K_i, H_B] = 0$, then $\langle e_\downarrow|e_\uparrow\rangle = \langle e^{-i\Phi_A}\rangle_{\rho_B}$ with $\Phi_A = t\sum_{i\in A} K_i$, up to a phase. For jointly*

TABLE S13. Crossing times (ms) of the Rényi-2 asymmetry of connected 3-ion blocks in the 12-ion data, by block (ions). "exp.": measured from the raw data (classical shadows; jackknife error in units of the last digits); "Prop. 2": predicted from the three-tilt $\kappa^2(t)$ of the block's own ions with the threshold of Proposition 2, no fit to asymmetries; "Eq. (9)": Eq. (9) with the measured block populations and the per-tilt normalized dephasing of the block's own ions; "one slope": the same with one three-tilt slope and intercept (threshold form); no fit to asymmetries; "exact": noiseless dynamics. "—": no crossing before 4 ms; values without parentheses have undefined jackknife errors (a replicate without a crossing).

block	1–3	2–4	3–5	4–6	5–7	6–8	7–9	8–10	9–11	10–12
$0.5\pi/0.2\pi$, exp.	3.21(13)	2.59(61)	1.40(6)	1.12(7)	1.08(7)	1.07(4)	1.26(13)	1.31(12)	2.06(80)	3.05(20)
Prop. 2	2.57(34)	2.28(16)	1.38(9)	1.17(8)	1.08(9)	1.14(12)	1.24(14)	1.13(16)	1.32(15)	2.47(13)
exact	2.28	1.65	1.29	1.22	1.19	1.19	1.22	1.29	1.65	2.28
Eq. (9)	2.76	2.31(89)	1.17(12)	1.00(9)	1.06(13)	1.05(13)	1.15(22)	1.01(14)	2.51(239)	2.70(24)
Eq. (9), one slope	2.67	2.28(86)	1.18(12)	1.01(9)	1.06(12)	1.05(13)	1.15(22)	1.01(14)	2.48(232)	2.65(28)
$0.5\pi/0.33\pi$, exp.	3.43(158)	0.67(16)	0.67(10)	0.64(10)	0.68(9)	0.67(14)	0.67(7)	0.67(6)	0.69(10)	2.84(221)
Prop. 2	2.29(14)	1.23(12)	0.95(7)	0.76(8)	0.76(8)	0.81(7)	0.86(9)	0.77(10)	0.90(10)	1.45(176)
exact	1.27	0.79	0.75	0.73	0.72	0.72	0.73	0.75	0.79	1.27
Eq. (9)	1.07	0.59(13)	0.60(11)	0.58(10)	0.90(25)	0.74(24)	0.62(12)	0.42(10)	0.70(51)	2.74(223)
Eq. (9), one slope	2.30(28)	1.00(26)	0.89(18)	0.67(18)	0.80(22)	0.83(22)	0.81(24)	0.40(20)	1.12(29)	1.34(24)
$0.33\pi/0.2\pi$, exp.	3.15(11)	2.51(33)	1.62(50)	1.26(11)	1.26(12)	1.28(16)	1.34(12)	1.68(27)	2.40(16)	3.01(11)
Prop. 2	> 2.91	2.60	1.96(12)	1.52(26)	1.38(11)	1.45(15)	1.62(17)	1.46(27)	2.25(16)	2.71(25)
exact	2.45	2.31	1.78	1.51	1.46	1.46	1.51	1.78	2.31	2.45
Eq. (9)	2.48(15)	2.36(19)	1.31(12)	1.12(14)	1.11(19)	1.13(24)	1.30(17)	1.19(17)	2.69	2.52
Eq. (9), one slope	2.88	2.71(32)	1.33(8)	1.11(9)	1.22(15)	1.18(17)	1.31(13)	1.18(14)	2.88	2.91

TABLE S14. Crossing times (ms) of the Rényi-2 asymmetry of connected 4-ion blocks in the 12-ion data, by block (ions). "exp.": measured from the raw data (classical shadows; jackknife error in units of the last digits); "Prop. 2": predicted from the three-tilt $\kappa^2(t)$ of the block's own ions with the threshold of Proposition 2, no fit to asymmetries; "Eq. (9)": Eq. (9) with the measured block populations and the per-tilt normalized dephasing of the block's own ions; "one slope": the same with one three-tilt slope and intercept (threshold form); no fit to asymmetries; "exact": noiseless dynamics. "—": no crossing before 4 ms; values without parentheses have undefined jackknife errors (a replicate without a crossing).

block	1–4	2–5	3–6	4–7	5–8	6–9	7–10	8–11	9–12
$0.5\pi/0.2\pi$, exp.	3.04(52)	1.88(92)	1.19(9)	1.08(5)	1.00(5)	1.08(3)	1.16(12)	1.42(24)	2.48(14)
Prop. 2	2.24(10)	1.32(10)	1.10(7)	1.04(7)	0.96(7)	1.00(7)	1.03(8)	1.10(14)	2.11(25)
exact	2.05	1.25	1.12	1.08	1.07	1.08	1.12	1.25	2.05
Eq. (9)	2.35(16)	1.18(16)	0.99(10)	1.06(13)	0.98(12)	0.98(11)	1.03(15)	1.14(26)	2.54(26)
Eq. (9), one slope	2.34(17)	1.19(16)	1.00(9)	1.06(13)	0.98(12)	0.98(11)	1.03(15)	1.15(27)	2.51(25)
$0.5\pi/0.33\pi$, exp.	2.75	0.72(9)	0.59(6)	0.58(8)	0.60(9)	0.71(19)	0.63(5)	0.71(12)	2.47(135)
Prop. 2	1.42(82)	0.88(10)	0.75(13)	0.70(21)	0.52(21)	0.71(21)	0.74(12)	0.76(10)	1.06(17)
exact	1.12	0.76	0.72	0.71	0.70	0.71	0.72	0.76	1.12
Eq. (9)	0.72(35)	0.53(14)	0.55(11)	0.90(29)	0.62(12)	0.49(10)	0.51(7)	0.42(15)	1.24(126)
Eq. (9), one slope	1.94(83)	0.70(30)	0.66(15)	0.97(20)	0.65(20)	0.55(15)	0.56(14)	0.50(38)	1.22(18)
$0.33\pi/0.2\pi$, exp.	3.06(77)	1.96(17)	1.34(9)	1.19(8)	1.27(12)	1.24(11)	1.28(11)	2.06(27)	2.49(23)
Prop. 2	2.41(11)	2.05(18)	1.35(8)	1.30(9)	1.18(10)	1.25(11)	1.28(13)	1.38(16)	2.33(12)
exact	2.39	2.00	1.41	1.31	1.28	1.31	1.41	2.00	2.39
Eq. (9)	2.29(17)	1.39(64)	1.13(11)	1.09(15)	1.04(11)	1.08(13)	1.12(17)	1.31(16)	2.54
Eq. (9), one slope	2.50(19)	1.37(12)	1.11(9)	1.11(12)	1.07(9)	1.10(11)	1.14(14)	1.30(17)	2.83

Gaussian site phases $\varphi_i = tK_i$ with covariance C_{ij},

$$c_A = \exp\Big[-\tfrac{1}{2}\textstyle\sum_{i,j\in A} C_{ij}\Big]. \tag{S11}$$

Theorem 1 is the case $K_i \equiv K$, where C_{ij} does not depend on i, j. Spin-wave theories give such Gaussian phases [18],

and the structure is shared with correlated-noise spectroscopy [19–21] and multiple-quantum coherences [22, 23].

Proof. By unitarity, (C1′) also leaves the orthogonal complement of the two extremal sectors invariant, so no other configuration of A feeds $|0_A\rangle$ or $|1_A\rangle$. Hence $\langle 1_A|\rho_A(t)|0_A\rangle = \langle 1_A|\rho_A(0)|0_A\rangle\langle e_\downarrow|e_\uparrow\rangle$. In the pointer form, $|0_A\rangle$ and $|1_A\rangle$ are the unique states of charge 0 and k, so they are eigenstates of the symmetric H_A and of every n_i; (C1′) holds, $|e_\downarrow\rangle = e^{-iH_B t}|e\rangle$ and $|e_\uparrow\rangle = e^{-iH_B t}e^{-it\sum_{i\in A}K_i}|e\rangle$ up to phases. For a Gaussian variable, $|\langle e^{-i\Phi}\rangle| = e^{-\operatorname{Var}\Phi/2}$. □

Corollary S2 (closure and its tests). *Under Eq.* (S11)*, define* $C_{ii} = -2\ln c_{\{i\}}$ *and* $C_{ij} = -\ln c_{\{i,j\}} - \frac{1}{2}(C_{ii}+C_{jj})$*. Then every* c_A *with* $k \geq 3$ *equals* $\exp[-\frac{1}{2}\sum_{i,j\in A} C_{ij}]$ *with no free parameter. Three consequences can falsify it: (i)* $|r_{ij}| \leq 1$ *for* $r_{ij} = C_{ij}/\sqrt{C_{ii}C_{jj}}$ *(Cauchy–Schwarz); (ii) the third-order Möbius difference* $D_3 = \ln c_{ijl} - \ln c_{ij} - \ln c_{jl} - \ln c_{il} + \ln c_i + \ln c_j + \ln c_l$ *vanishes; its leading term is* $\frac{1}{24}$ *times the fourth-order joint cumulants of the phases supported exactly on* $\{i,j,l\}$*, so it measures non-Gaussianity; (iii) if* $C_{ij} = C_c + C_\ell\delta_{ij}$ *on the region considered,* $\ln c_k = -\frac{1}{2}(k^2 C_c + kC_\ell)$*, which interpolates between the* k^2 *law of collective dephasing [24, 25] and the* k *law of independent dephasing. For random blocks drawn from a pool,* $\ln c_k/\ln c_1 = k + k(k-1)\bar{r}$ *to leading order, with* $\bar{r}$ *the pair average.*

Rotor part. For a U(1) magnet whose dynamics stays near the permutation-symmetric manifold, the projection of $H = \sum_{i<j} J_{ij}(\sigma_i^+\sigma_j^- + \text{h.c.})$ onto that manifold is a one-axis twister with strength $\bar{J} = \sum_{i\neq j} J_{ij}/[N(N-1)]$ [26–29]. Its cross term gives each site the pointer $K_i = -2\bar{J}S_{\bar{i}}^z$, where $\bar{i}$ is the complement of i. Two distant ions i, j then share the phase generated by the $N-2$ other spins,

$$C_\infty \equiv \operatorname{Cov}(\varphi_i,\varphi_j) = 4\bar{J}^2t^2\operatorname{Var}_\theta(S_{\bar{i}\bar{j}}^z) = \bar{J}^2t^2(N-2)\sin^2\theta, \tag{S12}$$

the rotor limit. The site-resolved spin-wave part adds a short-ranged contribution. Equation (S12) is therefore a limit, not a fit: at 1.5–3.3 ms it exceeds the measured C_∞ by factors 1.4–2.5, and in DTWA with the reconstructed coupling profile C_∞ rises from 0.35 to 0.80 of it between 1.5 and 3.3 ms. The prediction $C_\infty(\theta)/C_\infty(\pi/2) = \sin^2\theta$ (Q2) requires the remaining spin-wave admixture to scale with the tilt in the same way.

S9. ANALYSIS OF THE 51-ION DATA

Overview. Reference [30] squeezed [31, 32] chains of up to 51 ions [33] with the Hamiltonian of the Letter, $J_0 = 216$ rad/s and $\alpha \approx 0.9$ for $N = 51$, and published single-shot bit strings for five data sets with $N = 12$, 25 and 51, with the analysis axis scanned in azimuth ϕ at $\theta = \pi/2$. The k-th harmonic in ϕ of $\langle\prod_{i\in A}\sigma_i^\phi\rangle$ gives the top-order coherence c_A. The coherences of k-ion blocks decay neither by the k law nor by the k^2 law: at 1.8 ms, $\ln c_k/\ln c_1 = 3.0$, 6.0 and 10.1 for $k = 2, 3, 4$ [Fig. S2(a)]. Equation (S11) explains the hierarchy: from the measured one- and two-ion coherences it predicts all three- and four-ion coherences in all five data sets with a joint-residual $\chi^2/n = 1.44$ for $n = 55$ points and no fitted parameter [Fig. S2(d)]; prediction and measurement are resampled jointly from the same shots. The pair correlation $r(d,t)$ shows how the collective structure assumed by Theorem 1 forms [Fig. S2(b)], spreading as correlations do in long-range chains [34–36]: at 0.9 ms it falls from 1.2 ± 0.2 at $d = 1$ to 0.14 beyond $d = 20$; by 3.3 ms it averages 0.54 beyond $d = 20$. The far-field covariance C_∞ stays within 0.02 of zero up to 1.2 ms and reaches 0.38 ± 0.06 at 3.3 ms [Fig. S2(c)], below the rotor limit, Eq. (S12), by a factor 1.4–2.5. DTWA with the reconstructed coupling profile reproduces c_1 within 0.03 and C_∞ within about 2σ up to 3.3 ms, and c_2–c_4 up to about 2 ms; at 3.9 ms it misses C_∞ by 3σ. A power law fitting the near-neighbor couplings equally well overestimates C_∞ up to twofold. In a U(1) magnet the pointer splits into a collective rotor and site-resolved spin waves [26–29, 37, 38]; only the rotor contributes to C_∞.

Data. Zenodo 8124375 (CC-BY), associated with Ref. [30]. Records with the analysis axis scanned in azimuth at $\theta_a = \pi/2$: "Fig. 1c" records for $N = 12$ (10 times, 0–1.8 ms) and $N = 51$ (12 times, 0–3.9 ms), with 21 phases × 200 shots; "collective vector length" records for $N = 4, 8, 12, 25, 51$ (21 phases × 50–100 shots, up to 3.9 or 6.3 ms). Each shot is an integer whose least-significant bit is ion 1, with bit 0 meaning spin up. Analysis angles are in units of π.

Estimator. For a block A of k ions, $\langle\prod_{i\in A}\sigma_i^\phi\rangle$ has a k-th Fourier harmonic in the analysis azimuth ϕ of amplitude $2|\langle\prod_{i\in A}\sigma_i^+\rangle|$. We fit harmonics $0, \ldots, k$ by least squares to the 21 phases. The shots at each phase are split into 10 disjoint groups; the U-statistic $\big(|\sum_g A_g|^2 - \sum_g |A_g|^2\big)/[10\cdot 9]$ of the group amplitudes A_g is an unbiased estimator of $|A|^2$. We average it over blocks before normalizing by its $t = 0$ value. Errors are leave-one-group-out jackknife errors. For $N = 51$ we use the bulk ions 6–46 and 1500 random blocks per k; for $N = 25$ and 12 the bulk ions 4–22 and 2–11.

Validation. From the same files we recompute 39 published numbers: the total spin $\langle\mathbf{S}^2\rangle/S(S+1)$ versus time for $N = 51$ (12 values) and versus N at 1.8 ms (5 values), from the x, y and z settings; and the Wineland squeezing

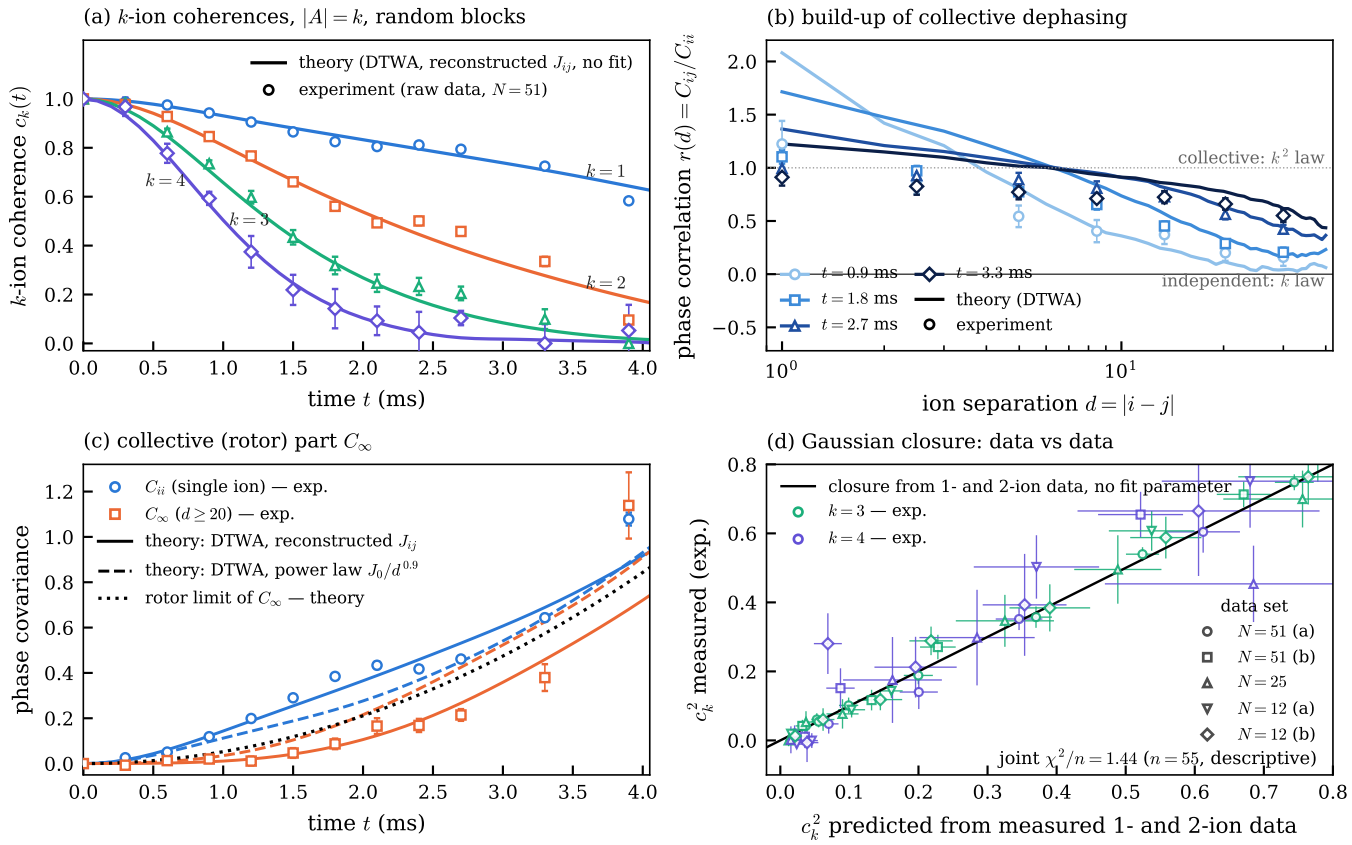


FIG. S2. Raw data of the 51-ion chain of Ref. [30] ($\theta = \pi/2$; open symbols). (a) Top-order coherence c_k of random k-ion blocks; lines: DTWA with the reconstructed coupling profile, no fit parameter. (b) Pair phase correlation $r(d)$, averaged over pairs at distance d, at four times; under the Gaussian reading, $r = 1$ is collective and $r = 0$ independent dephasing, while $r > 1$ rejects that reading; lines: DTWA. (c) Single-ion phase variance $C_{ii} = -2 \ln c_1$ and far-field covariance C_∞ ($d \geq 20$). Solid: DTWA as in (a); dashed: DTWA with the power-law fit of Ref. [30]; dotted: rotor limit, Eq. (S12). (d) Measured c_3^2 and c_4^2 against Eq. (S11) evaluated with measured one- and two-ion coherences (five data sets, $N = 12$, 25, 51).

parameter for $N = 12$ (10 values) and $N = 51$ (12 values) [39], using a sinusoidal fit of the variance against the rotation angle. All 39 agree within 2σ (median 0.54σ, maximum 1.67σ; Table S15).

Exponents and non-Gaussianity. Table S16 gives $\ln c_k / \ln c_1$ for the 200-shot $N = 51$ record, the prediction $k + k(k-1)\bar{r}$ of Corollary S2(iii) with $\bar{r}$ from random pairs, and the Möbius difference D_3 evaluated on block averages. D_3 is consistent with zero at every time ($|D_3| < 1\sigma$). In the 100-shot $N = 51$ record, $D_3 = 0.08 \pm 0.02$ at 1.2 ms and 0.03 ± 0.02 at 0.6 ms; other times are consistent with zero.

Closure test of Fig. S2(d). For each of the five data sets (200-shot $N = 12$ and $N = 51$ records, labelled (a); 50–100-shot collective-vector-length records for $N = 12$, 25, 51, labelled (b) or by N), C_{ii} and C_{ij} are formed from the measured one- and two-ion coherences of the sampled blocks, and c_A^2 for $k = 3, 4$ is predicted from Eq. (S11) and averaged over the same blocks. Points with predicted $c_k^2 < 0.01$ and $t = 0$ are excluded. Prediction and measurement use the same shots and the same 10 shot groups, so every jackknife replicate gives both, and the error of the residual $y - x$ is the jackknife error of that residual (script `closure_joint.py`). The covariance is positive for 49 of the 55 points, and the joint error is a median 0.61 of the quadrature error $(\sigma_y^2 + \sigma_x^2)^{1/2}$. With the joint errors $\chi^2/n = 1.44$ for $n = 55$ (quadrature: 0.57, which omits the covariance). By data set: 0.43 ($N = 51$ (a), 15 points), 3.03 ($N = 51$ (b), 7), 0.53 ($N = 25$, 12), 3.45 ($N = 12$ (a), 9) and 1.18 ($N = 12$ (b), 12); the mean residual is $+0.009$. Points of one data set share their $t = 0$ normalization, so this χ^2 is descriptive, not a calibrated goodness of fit: the closure describes the three- and four-ion coherences to about 1.2σ rms, with residuals up to 3σ in two of the five data sets.

Pair correlations above the Gaussian bound. A Gaussian phase field requires $|r_{ij}| \leq 1$ (Corollary S2(i)). DTWA gives $r(d) > 1$ for $d \leq 3$ at 0.9 ms ($r(1) = 2.08$) and for $d \leq 5$ at 2–3.3 ms; the data give $r(1) = 1.2 \pm 0.2$ at 0.9 ms. Values above 1 reject the Gaussian phase-covariance interpretation, but do not identify charge exchange by themselves. A charge-preserving collective rotation with phase $\varphi = \pm a$ equally likely gives $c_1 = \cos a$, $c_2 = \cos 2a$ and

TABLE S15. Recomputed versus published values for the 51-ion experiment [30]. Left: total spin $\langle \mathbf{S}^2 \rangle / S(S+1)$ for $N = 51$ versus time and versus N at 1.8 ms. Right: squeezing parameter in dB. Errors: ours by bootstrap over shots; published as given.

	total spin				squeezing (dB)		
setting	ours	published	dev.	setting	ours	published	dev.
N=51, 0.0 ms	0.999(6)	0.996(8)	$+0.3\sigma$	N=12, 0.2 ms	−1.41(10)	−1.49(12)	$+0.5\sigma$
N=51, 0.6 ms	0.962(10)	0.940(12)	$+1.5\sigma$	N=12, 0.6 ms	−3.38(22)	−3.31(15)	-0.3σ
N=51, 1.2 ms	0.847(22)	0.830(22)	$+0.5\sigma$	N=12, 1.0 ms	−3.70(52)	−3.85(27)	$+0.3\sigma$
N=51, 2.4 ms	0.815(35)	0.790(35)	$+0.5\sigma$	N=12, 1.8 ms	4.38(42)	4.16(36)	$+0.4\sigma$
N=51, 3.9 ms	0.790(38)	0.755(40)	$+0.6\sigma$	N=51, 0.6 ms	−1.91(28)	−2.10(23)	$+0.5\sigma$
N=51, 6.3 ms	0.672(35)	0.640(35)	$+0.6\sigma$	N=51, 1.2 ms	−4.9(10)	−3.08(36)	-1.7σ
N=4, 1.8 ms	1.002(44)	1.032(37)	-0.5σ	N=51, 2.1 ms	−1.9(13)	−3.76(52)	$+1.4\sigma$
N=25, 1.8 ms	0.871(45)	0.851(46)	$+0.3\sigma$	N=51, 3.9 ms	−0.4(17)	1.04(39)	-0.8σ

Sixteen of the 39 comparisons are shown; the remaining 23 are in `data/validation_franke.json`.

TABLE S16. Coherence-order exponents for $N = 51$ (200-shot record): measured $\gamma_k = \ln c_k / \ln c_1$, prediction $k + k(k-1)\bar{r}$ from pairs, and third-order Möbius difference.

t (ms)	γ_2	$\bar{r}$	γ_3 meas.	γ_3 pred.	γ_4 meas.	γ_4 pred.	D_3
0.6	2.94	0.47	5.71	5.83	9.90	9.65	$+0.003 \pm 0.016$
0.9	2.82	0.41	5.20	5.46	8.80	8.92	$+0.016 \pm 0.017$
1.2	2.67	0.34	5.17	5.02	9.88	8.03	-0.016 ± 0.022
1.5	2.86	0.43	5.75	5.57	10.47	9.13	-0.027 ± 0.033
1.8	3.01	0.50	5.95	6.03	10.14	10.06	$+0.015 \pm 0.074$
2.1	3.26	0.63	6.46	6.79	10.98	11.57	$+0.071 \pm 0.083$
2.7	3.39	0.69	6.88	7.16	9.82	12.32	$+0.065 \pm 0.092$

$r = (-\ln c_2 + 2\ln c_1)/(-2\ln c_1) = 1.10$ at $a = 0.3$. Non-Gaussian phases or estimator effects can therefore also produce such values. In the XY model, magnon exchange changes the pair populations and supports a transport contribution of the (C1)-violating type discussed in Proposition 3; this model interpretation is not uniquely identified by $r > 1$. The closure relation tested in Fig. S2(d) can hold without the extracted C_{ij} forming a positive covariance matrix. At large d we use the phase-covariance interpretation as the tested Gaussian approximation and evaluate C_∞ there.

Far-field covariance. C_∞ is evaluated from pairs with separation $d \geq 20$ inside the bulk, weighted by the number of pairs at each d: $C_\infty = -\frac{1}{2}\ln \overline{c_{ij}^2} - C_{ii}$, with $C_{ii} = -2\ln c_1$.

S10. DISCRETE TRUNCATED WIGNER SIMULATIONS

Model. $H = \sum_{i<j} J_{ij}(\sigma_i^+\sigma_j^- + \text{h.c.})$ with $N = 51$ and $J_0 = 216$ rad/s [30]. "Reconstructed coupling profile": built from the simulated rows $J_{10,j}$, $J_{26,j}$, $J_{42,j}$ given in the source-data files of Ref. [30] (Zenodo 8124375; read as numbers, not digitized), averaged over rows and sides at each distance d (six values per distance for $d \leq 9$, four up to $d = 25$, two up to $d = 41$), continued exponentially beyond $d = 41$ (0.02% of $\sum J_{ij}$), normalized to unit nearest-neighbor coupling and scaled to J_0; translation invariance is assumed. "Power-law fit": $J_{ij} = J_0|i-j|^{-0.9}$. The resulting one-axis-twisting strength is $\bar{J} = 0.033$ rad/ms (profile) and 0.035 rad/ms (power law); at $d = 20$ the two couplings differ threefold ($J_{ij}/J_0 = 0.022$ and 0.068).

Method. Discrete truncated Wigner approximation [40, 41]: each spin starts as $\vec{s} = \vec{n} + a\,\vec{e}_1 + b\,\vec{e}_2$ with $a, b = \pm 1$ equiprobable, where $\vec{n}$ is the initial direction and $\vec{e}_{1,2}$ are orthogonal to it. Classical equations $\dot{\vec{s}}_i = 2\vec{h}_i \times \vec{s}_i$ with $\vec{h}_i = \sum_j J_{ij}(s_j^x, s_j^y, 0)/2$ are integrated with fourth-order Runge–Kutta, step 0.02 ms, in single precision. Observables use the Weyl symbol $s^x + is^y$ of $2\sigma^+$: c_A is the modulus of the trajectory average of $\prod_{i\in A}(s_i^x + is_i^y)$, with the same split-half unbiased estimator and block sampling as the data. Seeds are fixed in the scripts.

Convergence. With the profile couplings, c_1 at 1.2, 2.4 and 3.3 ms changes by less than 0.005 between 8×10^3, 1.6×10^4 and 3.2×10^4 trajectories, and the $d = 20$ covariance by less than 10% (0.25–0.28 at 2.4 ms, 0.54–0.60 at 3.3 ms). Halving the time step changes no digit shown. Figures use 1.6×10^4 trajectories (2.4×10^4 for Fig. 4).

Prediction of Fig. 4. Tilted initial states use $\vec{n} = (\sin\theta, 0, -\cos\theta)$. For each of five bulk blocks of four adjacent ions (starting at ions 16, 20, 24, 28, 32), the 256 Pauli expectation values are trajectory averages of products of $(1, s^x, s^y, s^z)$ components, from which ρ_A is assembled. Purities $\mathrm{Tr}\,\rho_A^2$ and $\mathrm{Tr}(\mathcal{P}\rho_A)^2$ use two independent halves of the trajectories to avoid noise bias. At $t = 0$ the method gives $\Delta S_A^{(2)} = 0.640$, 1.115 and 1.299 for the three tilts, against the exact 0.635, 1.117 and 1.297. Figure 4 shows the TDVP asymmetries of Sec. S11 and marks the DTWA crossings. DTWA is approximate for four-body correlators, and the crossings at 3.3–4.0 ms lie at the end of the recorded window: at 3.9 ms DTWA gives c_1 0.06 above and C_∞ 3.1σ below the data. There the data give $C_\infty = 1.14 \pm 0.15 > C_{ii} = 1.08 \pm 0.03$, i.e. a far-field correlation above 1, which a Gaussian phase field forbids; the miss may partly be an estimator effect at this last time.

Benchmark on 12 ions. For the 12-ion chain of Sec. S6 ($J_{ij} = J_0/|i-j|$, $J_0 = 560$ rad/s) we ran the same DTWA code (3.2×10^4 trajectories, step 0.01 ms, all 15 four-ion blocks of the central six ions) and compared with exact dynamics. Crossing times of the Rényi-2 asymmetry (exact / DTWA / threshold rule with the exact single-ion κ^2 / threshold rule with the DTWA single-ion κ^2): 0.5π vs 0.2π: 1.13 / 1.24 / 1.09 / 1.18 ms; 0.5π vs 0.33π: 0.73 / 0.74 / 0.61 / 0.64 ms; 0.33π vs 0.2π: 1.37 / 1.53 / 1.39 / 1.50 ms. DTWA and the rule are each within 0.16 ms of the exact crossings here, but the exact crossing lies outside the interval between DTWA and the rule with the DTWA κ^2 for two of the three pairs, so the two estimates do not bound the true crossing.

S11. TENSOR-NETWORK CHECK AND ORIGIN OF THE 51-ION GAP

Method. We simulated the 51-ion chain with the two-site time-dependent variational principle (TDVP) for matrix product states [42], implemented in TeNPy 1.1.1 [43] without charge conservation (the tilted state breaks it). The long-range couplings enter through a matrix-product operator built from a fit of the published profile $J(d)$, $d = 1, \ldots, 50$, by eight exponentials (bond dimension 18); the fit reproduces $J(d)$ within 0.5% for $d \le 10$ and within $0.003J_0$ beyond, and $\bar{J}$ to three digits. With this fit the zero-density limit of Proposition 3 and the low-density series at 0.2π change by at most 0.005. Time step 0.1 ms, bond dimension $\chi = 64$; four-ion density matrices of the five blocks of Fig. 4 (ions 16–19, …, 32–35) and $\langle\sigma_i^+\rangle$ of ions 6–46 are recorded every 0.2 ms (scripts `mps_xy_exp.py`, `mps_analysis.py`, `mps_pertilt.py`; outputs in `data/tdvp`). At $t = 0$ the asymmetries are exact (0.6350, 1.1168, 1.2967).

Convergence and benchmark. (i) Truncation: the discarded weight per step stays below 4×10^{-7} (0.2π) and 3×10^{-5} (0.33π) up to 5 ms; at 0.5π it reaches 8×10^{-6} at 3.4 ms and 1.8×10^{-4} at 5 ms. Raising χ to 96 changes the block asymmetry by at most 2×10^{-7} (0.2π, up to 4 ms), 9×10^{-7} (0.33π, up to 4 ms) and 1.4×10^{-5} (0.5π, up to 3.6 ms), and the three crossing times by less than 10^{-4} ms (script `conv_chi.py`). (ii) Time step: halving it to 0.05 ms changes the block asymmetry by at most 4.8×10^{-4} (0.2π, up to 4 ms), 1.1×10^{-3} (0.33π, up to 4 ms) and 1.6×10^{-3} (0.5π, up to 3.4 ms), and the three crossing times by 0.013, 0.005 and 0.005 ms (scripts `conv_check.py`, `conv_cross.py`). (iii) Exact benchmark: the same code and settings on the 12-ion chain ($J_{ij} = J_0/|i-j|$, fitted the same way) agree with exact state-vector dynamics for the same couplings within 1.5×10^{-3} in the central-block asymmetry and 8×10^{-4} in $|\langle\sigma_i^+\rangle|$ up to 3 ms at all three tilts, also with $\chi = 16$ (script `tdvp_vs_exact12.py`). (iv) At 0.2π the single-ion dephasing agrees with the exact low-density series of Sec. S4 within the size of its last term (0.004 up to 2.5 ms).

Block spread and edge effect. The five blocks cross at 2.12–2.21, 3.24–3.33 and 3.64–3.86 ms (bars in Fig. 4); the outer blocks (ions 16–19 and 32–35) cross latest for the pairs involving 0.2π, as Joshi *et al.* observed for edge subsystems [14] and as transport (Proposition 3) implies. Script `sector51.py`.

DTWA against TDVP. DTWA reproduces the TDVP crossing times within 0.31 ms (Table S17). It underestimates all three asymmetries by 0.02–0.06 between 1 and 3 ms, and it is late for the pairs involving 0.2π, where it puts the block dephasing at $+0.045$ at 3 ms against -0.04 in TDVP.

Robustness and resolvability. A tilt-blind collective dephasing of the blocks, $F_n \to F_n e^{-n^2 s_t^2}$ with s_t^2 growing linearly to 0.1, 0.3 or 1.0 at 3 ms, shifts the crossings by at most 0.03, 0.06 and 0.08 ms, respectively (script `tech_dephasing.py`), as Proposition 2 anticipates (g cancels at leading order). The time resolution of a crossing is $\sigma/|\partial_t(\Delta S_> - \Delta S_<)|$ for an asymmetry error σ: the slopes at the crossings are 0.034, 0.134 and 0.081 ms^{-1}, so $\sigma = 0.02$ (as in the 12-ion data) resolves the pairs involving 0.2π to 0.15 and 0.25 ms, while the $0.5\pi/0.33\pi$ pair, whose curves stay within 0.008 of each other for ± 0.3 ms, needs $\sigma \lesssim 0.01$ for 0.3 ms.

Rules that ignore transport fail in the 51-ion chain. No single unnormalized slope fixes the three crossings (Table S17): the three-tilt single-ion κ^2 of ions 6–46 misses the pairs involving 0.2π by 0.8 ms or more; that of the blocks' own ions 16–35 misses two pairs by 0.46 and 0.82 ms; and the block slope $\tilde{\kappa}_A^2$ misses two pairs by 0.96 and 0.68 ms. Even Eq. (3) with each block's own per-tilt sector dephasing $\tilde{s}^2 = -\ln R_1$ misses by up to 0.42 ms. Two features accompany the failure: position (by Proposition 3 the end ions lose charge and the central ions gain it) and non-Gaussian unnormalized

sectors at 0.2π, where $R_1 = 1.04$–1.05 while R_2 falls to 0.57, so that $\ln R_2/\ln R_1 = -5$ to -14, F_0 falls by 13–16% and p_q drifts by 0.10–0.12 in total variation.

Why: transport. Both effects are the transport of Proposition 3. At 0.2π the central blocks gain charge, which broadens p_q, lowers F_0 and raises the unnormalized ratios F_n/F_0 through the populations, not through the coherences. Separating the two with Eq. (S10) (script `transport51.py`): (i) The normalized coherences are Gaussian in $|q-q'|$ at all tilts: with $\bar{G}_n$ the $w_q w_{q'}$-weighted mean of $\gamma_{qq'}$ over $|q-q'| = n$, normalized at $t = 0$, $\ln \bar{G}_2/\ln \bar{G}_1 = 3.97$, 3.71, 3.86 at 1, 2, 3 ms (0.2π), 4.00, 3.92, 4.00 (0.33π) and 4.04, 3.98, 4.01 (0.5π); the Gaussian value is 4. (ii) The block's normalized dephasing $-\ln \bar{G}_1$ is 0.915–0.934 times its site-aggregate dephasing $-\ln[C_A(t)/C_A(0)]$ (median over 1–3.6 ms), against $(N-N_A)/(N-1) = 0.94$. (iii) Equation (S10) with the exact w_q and Gaussian γ from the block's own $\bar{G}_1$ reproduces the TDVP crossings within 0.02 ms; replacing the block quantities by measurable ones keeps the accuracy (Table S17): Eq. (9) with the blocks' $p_q(t)$ and the per-tilt $\bar{s}_i^2$ of their ions gives 2.25, 3.30 and 3.78 ms with the environment factor (2.16, 3.20, 3.66 without it), within 0.08 ms of the block-averaged TDVP crossings. With one three-tilt slope, $\bar{s}_i^2 = \bar{\kappa}^2 \sin^2\theta$ (the threshold form of Proposition 2 with moving populations), it gives 1.92, 3.05 and 3.57 ms, within 0.26 ms; the single-ion $\bar{s}_i^2$ deviates from a line through the origin in $\sin^2\theta$ by at most 0.069 up to 4 ms. Using only single-site densities, with p_q approximated by the Poisson-binomial law of the block's site densities, gives 2.29, 3.51 and 4.01 ms (within 0.29 ms): the correlations of the block populations matter at this level. (iv) With one three-tilt slope and a tilt-blind intercept, $\bar{s}_i^2 = \bar{\kappa}^2 \sin^2\theta + 2\bar{g}$ (the threshold form of Proposition 2 at fixed g, with moving populations), Eq. (9) gives 2.07, 3.29 and 3.92 ms (within about 0.20 ms in the three-tilt form); the fitted $\bar{g}$ is 0.001, 0.013 and 0.035 at 1, 2 and 3 ms, so the normalized dephasing has a small, nonzero fitted intercept over this window (script `transport51_c9.py`). (v) Which part of the population change matters (script `transport51_drift.py`; per-tilt $\bar{s}_i^2$ with the factor 0.94): with frozen binomial p_q the crossings are at 2.99 ms, none and none before 5 ms; with p_q replaced by the Poisson-binomial law of the measured site densities (mean shift by transport, no correlations) at 2.39, 3.62 and 4.13 ms; with the full $p_q(t)$ at 2.25, 3.30 and 3.78 ms. Both parts matter: transport raises the mean charge of the central blocks at 0.2π from 0.38 to 0.40 (1 ms) and 0.50 (3 ms), and correlations narrow the block charge distribution below the Poisson-binomial width at every tilt (variance 0.80 against 1.00 at 0.5π, 1 ms), a number squeezing that transport does not produce. In this chain the dephasing threshold alone, with frozen populations, does not produce the crossings with 0.2π before 5 ms; with the populations it does. Population changes alone produce no crossing (Sec. S5). All transport-separated rules were formulated after the TDVP crossings were known; they contain no parameter adjusted to the crossings, and the environment factor is fixed by Corollary 1. Table S17 lists every variant we evaluated.

S12. HELD-OUT VALIDATION OF EQ. (9), ERROR BUDGET AND COUPLING SENSITIVITY

Frozen specification. The threshold form of Eq. (9) was formulated after the 51-ion crossings of Sec. S11 were known. Before any further simulation was run, we wrote its complete specification (inputs, three-tilt slope and intercept of the normalized single-ion dephasing of the block's own ions fitted on the tilts $\{0.2, 0.33, 0.5\}\pi$, environment factor $(N-N_A)/(N-1)$, crossing extraction, treatment of absent crossings, test sets and metrics) to `validation_v008/FROZEN_RULE_SPEC.md`, SHA-256 `9e01dc2629eec0c562d064f6dde2d7f6eb934eca00b38b20e08bf41a108a5eb9`, 2026-10-31 21:45:54 UTC. Three rules are evaluated on every test crossing: P, the threshold form (the rule of the Letter); T, Eq. (9) per tilt; S, the simplest form (Eq. (3) with binomial populations and the unnormalized three-tilt slope, $g = 0$). The truth is the exact Rényi-2 asymmetry from the full block state. A crossing is the first sign change from positive to non-positive of $\Delta S_A^{(2)}(\theta_2) - \Delta S_A^{(2)}(\theta_1)$ after $t = 0$, linearly interpolated; an absent crossing is recorded as such. The rules use no parameter fitted to asymmetries or crossings; they do require the block populations at the test tilt, a many-body input that is measured, not predicted.

Test sets. H1: the 12-ion chain of the experiment ($J_{ij} = J_0/|i-j|$, $J_0 = 560$ rad/s) at the new tilts 0.25π and 0.4π, all 7 tilt pairs that involve a new tilt, all 19 connected blocks of 3 and 4 ions. H2: 12-ion chains with the new exponents $\alpha = 0.5$ and 1.5, all 10 pairs of the five tilts. H3: the 12-ion chain with independent random couplings $J_{ij}(1+\varepsilon_{ij})$, ε_{ij} uniform in $[-0.1, 0.1]$ (two realizations), all 10 pairs. H4: the 51-ion chain with the reconstructed profile at the new tilts (TDVP, $\chi = 64$, $dt = 0.1$ ms, Sec. S11), the 7 pairs that involve a new tilt. H5: the 51-ion chain with the alternative, power-law reconstruction $J_0|i-j|^{-0.9}$ (TDVP as H4), all 10 pairs. Calibration always uses the tilts $\{0.2, 0.33, 0.5\}\pi$ of the same system. Exact dynamics (scripts `heldout12.py`, `eval12.py`) reproduce the exact 12-ion dynamics of Table S7 to 3×10^{-14}; the 51-ion evaluation (`eval51.py`) reproduces the crossings of Table S17.

Results. No rule misses or invents a crossing in the 893 exact 12-ion test crossings (Table S18). For the experiment's chain at new tilts (H1), rule P has median errors of 0.04 ms in the bulk (90th percentile 0.09 ms) and 0.15 ms at the end blocks, against 0.09 and 0.35 ms for the simplest form; with random couplings (H3) the numbers are almost

TABLE S17. Crossing times (ms) of the four-ion Rényi-2 asymmetry in the 51-ion chain. Simulations: TDVP ($\chi = 64$, $dt = 0.1$ ms; range over the five blocks; $dt = 0.05$ ms) and DTWA. Single-slope rules (Proposition 2 with a three-tilt slope): single-ion κ^2 of ions 6–46 or of the blocks' own ions 16–35, and the block slope $\tilde{\kappa}_A^2$ from $-\ln R_1$. Per-tilt rules (Eq. (3) with the per-tilt dephasing): single-ion s^2 of ions 6–46, single-ion s^2 of the blocks' own ions (identified after the simulation), and the blocks' own sector dephasing $\tilde{s}^2 = -\ln R_1$. Transport-separated rules (Sec. S11): Eq. (S10) with the exact sector weights and Gaussian normalized coherences, and Eq. (9) with the blocks' populations and the normalized dephasing of their ions 16–35. "—": not reached before 5 ms.

	0.5π vs 0.33π	0.5π vs 0.2π	0.33π vs 0.2π
TDVP	2.18	3.28	3.72
TDVP, range over blocks	2.12–2.21	3.24–3.33	3.64–3.86
TDVP, $dt = 0.05$ ms	2.16	3.27	3.72
DTWA	2.19	3.53	4.03
Prop. 2, κ^2 of ions 6–46	1.78	4.06	—
Prop. 2, κ^2 of ions 16–35	1.72	3.44	4.54
Prop. 2, block slope $\tilde{\kappa}_A^2$	1.22	3.18	4.40
Eq. (3), s^2 of ions 6–46	1.86	4.03	—
Eq. (3), s^2 of ions 16–35	1.82	3.28	3.99
Eq. (3), block $\tilde{s}^2$	2.04	2.99	3.30
Eq. (S10), exact w_q, block $\bar{G}_1$	2.20	3.29	3.74
Eq. (9), per-tilt $\bar{s}_i^2$, factor 0.94	2.25	3.30	3.78
Eq. (9), per-tilt $\bar{s}_i^2$, no factor	2.16	3.20	3.66
Eq. (9), one slope $\bar{\kappa}^2 \sin^2\theta$, factor 0.94	1.92	3.05	3.57
Eq. (9), site densities only (Poisson-binomial p_q)	2.29	3.51	4.01
Eq. (9), site densities only, one slope, no factor	1.96	3.21	3.76
Eq. (9), one slope, no factor	1.83	2.97	3.47
Eq. (9), one slope and intercept, factor 0.94	2.07	3.29	3.92
Eq. (9), per-tilt $\bar{s}_i^2$, factor 0.94, frozen binomial p_q	2.99	—	—
Eq. (9), per-tilt $\bar{s}_i^2$, factor 0.94, mean drift only	2.39	3.62	4.13

the same (0.06 and 0.16 ms, simplest 0.08 and 0.35 ms), and for the longer-range chain $\alpha = 0.5$ they are smaller (0.04 and 0.06 ms, maximum 0.08 ms). For the shorter-range chain $\alpha = 1.5$ the rule degrades: bulk median 0.13 ms, worse than the simplest form (0.10 ms), and end blocks 0.66 ms (simplest form 0.68 ms), with errors up to 1.0 ms, all predicted early. The error budget (Table S19) locates the failure in the block-to-site conversion, which alone shifts the end-block crossings of this chain by 0.57 ms (median): with shorter-range couplings the phases of the ions in a block do not become collective before the crossings, which come late (median 2.4 ms at the end blocks), and the conversion overestimates the block's dephasing. These tests support the rule for the sampled $\alpha = 0.5, 1$ chains and reconstructed 51-ion models; they do not establish validity for every $\alpha \leq 1$. The $\alpha = 1.5$ chain fails at the end blocks. In the 12-ion sets the per-tilt rule T performs like P (medians within 0.02 ms), so fitting one slope and intercept across tilts costs little there. In TDVP of the 51-ion chain at the new tilts (H4) the block-averaged crossings of rule P deviate by a median 0.07 ms (maximum 0.40 ms, 7 pairs), per block 0.07 ms; the simplest form, by 0.38 ms (maximum 0.50 ms). Existence errors: rule P 0 missed and 0 invented, rule S 1 and 0. The largest error, +0.40 ms, is for the closest pair of tilts, 0.25π vs 0.2π, whose true crossing is the latest (4.46 ms); the simplest form finds none for 0.25π vs 0.2π before 5 ms. With the power-law couplings (H5), rule P deviates by a median 0.06 ms (maximum 0.10 ms, 9 pairs; per block 0.06 ms) and the simplest form by 0.41 ms (maximum 0.70 ms). No rule misses or invents a block-averaged crossing; 0.25π vs 0.2π does not cross before 5 ms, and neither rule predicts a crossing.

Headline aggregation. The pooled statistic in the abstract combines 703 exact 12-ion evaluations in H1, H2 at $\alpha = 0.5$, and H3 with 7 block-averaged H4 crossings and 9 block-averaged H5 crossings: 719 evaluations, with median absolute error 0.056 ms (0.06 ms rounded). This pooling is a descriptive summary across the specified systems; overlapping blocks, shared tilts and reused Hamiltonians do not constitute independent trials. The boundary strata and largest errors remain those of Table S18.

Scope of use. The interaction exponent is not an applicability diagnostic. These tests concern the specified sizes, preparations, blocks and time windows; the sampled successes and the failure at $\alpha = 1.5$ do not locate a sharp validity boundary. Outside these settings, Eq. (9) is an empirical estimate whose collective conversion must be checked

TABLE S18. Held-out validation of the frozen rules (crossing times, ms). n: crossings found by both the truth and rule P; $|\Delta t|$: rule minus truth, median and 90th percentile; mean Δt (negative: predicted early); T, S: medians of rules T and S on their own crossings; last column: crossings whose existence the rule gets wrong (rule P / rule S). End: blocks that contain ion 1 or ion N. 51 ions: asymmetries averaged over the five central blocks ("block avg.") or per block.

set	stratum	n	P med.	P 90%	P mean	T med.	S med.	S 90%	existence errors
H1, $\alpha = 1$, new tilts	bulk	105	0.04	0.09	−0.01	0.04	0.09	0.26	0/0
	end	28	0.15	0.31	−0.21	0.16	0.35	0.52	0/0
H2, $\alpha = 0.5$	bulk	150	0.04	0.06	+0.02	0.03	0.04	0.17	0/0
	end	40	0.06	0.07	−0.06	0.06	0.17	0.25	0/0
H2, $\alpha = 1.5$	bulk	150	0.13	0.22	−0.17	0.14	0.10	0.22	0/0
	end	40	0.66	0.74	−0.58	0.64	0.68	0.96	0/0
H3, ±10% couplings	bulk	300	0.06	0.09	0.00	0.06	0.08	0.22	0/0
	end	80	0.16	0.29	−0.19	0.16	0.35	0.55	0/0
H4, new tilts	block avg.	7	0.07	0.24	+0.02	0.04	0.38	0.45	0/1
	per block	33	0.07	0.13	0.00	0.03	0.36	0.48	2/5
51 ions, in-sample	block avg.	3	0.11	0.18	+0.03	0.06	0.45	0.75	0/0
	per block	15	0.11	0.22	+0.04	0.06	0.46	0.84	0/0
H5, power law	block avg.	9	0.06	0.07	−0.02	0.03	0.41	0.60	0/0
	per block	45	0.06	0.09	−0.02	0.03	0.39	0.65	0/0

TABLE S19. Error budget of Eq. (9): median shift of the crossing time (ms; 90th percentile in parentheses) caused by each approximation, introduced in the order shown, and the population-weighted sector purity $\mathrm{Tr}\,\hat{\rho}_q^2$ at the true crossing (median; minimum). Sets as in Table S18; the 51-ion rows use all evaluated pairs of the block-averaged asymmetry.

set	stratum	purity ($w_q \to p_q$)	Gaussian γ	block-to-site	one slope	sector purity
H1, $\alpha = 1$, new tilts	bulk	0.007 (0.01)	0.010 (0.01)	0.045 (0.08)	0.011 (0.04)	0.981 (0.96)
	end	0.010 (0.03)	0.008 (0.02)	0.157 (0.33)	0.022 (0.06)	0.981 (0.97)
H2, $\alpha = 0.5$	bulk	0.001 (0.00)	0.010 (0.01)	0.022 (0.05)	0.006 (0.02)	0.998 (0.99)
	end	0.001 (0.00)	0.006 (0.01)	0.061 (0.08)	0.003 (0.01)	0.997 (0.99)
H2, $\alpha = 1.5$	bulk	0.019 (0.03)	0.004 (0.01)	0.127 (0.19)	0.021 (0.07)	0.946 (0.90)
	end	0.036 (0.07)	0.012 (0.02)	0.572 (0.76)	0.042 (0.10)	0.945 (0.91)
H3, ±10% couplings	bulk	0.007 (0.01)	0.009 (0.01)	0.060 (0.09)	0.012 (0.04)	0.981 (0.96)
	end	0.010 (0.03)	0.007 (0.02)	0.161 (0.33)	0.028 (0.06)	0.980 (0.97)
51 ions, profile	block avg.	0.006 (0.01)	0.015 (0.02)	0.034 (0.06)	0.105 (0.27)	0.995 (0.99)
51 ions, power law	block avg.	0.003 (0.00)	0.004 (0.01)	0.023 (0.06)	0.020 (0.06)	0.997 (0.99)

independently. We do not establish a single-site criterion that guarantees its accuracy.

Error budget of Eq. (9). Starting from the exact rewriting, Eq. (S10), we introduce the approximations one at a time and record how far each moves the crossing (Table S19): L1, sector purity ($w_q \to p_q$; $w_q = p_q(\mathrm{Tr}\,\hat{\rho}_q^2)^{1/2}$ with $\hat{\rho}_q$ the normalized sector state); L2, Gaussian normalized coherences with the block's own $\bar{s}_b^2 = -\ln \bar{G}_1$; T, the block-to-site conversion $\bar{s}_A^2 = \bar{s}_i^2(N - N_A)/(N - 1)$ per tilt; P, one three-tilt slope and intercept. For the tested $\alpha \le 1$ cases, sector purity and Gaussianity each move the crossings by about 0.01 ms (90th percentiles ≤ 0.03 ms), and the sector purity at the true crossings is 0.98–1.00 (median). The block-to-site conversion dominates: 0.02–0.06 ms in the bulk and 0.06–0.16 ms (median) at the end blocks, where the phase correlations within the block are not yet collective (Table S6); for $\alpha = 1.5$ it reaches 0.13 ms in the bulk and 0.57 ms at the end blocks, and the purity falls to 0.95 (median; minimum 0.90). The single slope and intercept adds about 0.01 ms (up to 0.04 ms at $\alpha = 1.5$) at 12 ions; at 51 ions with the reconstructed profile it is the largest item (median 0.10 ms, 90th percentile 0.27 ms), because there the per-tilt normalized single-site dephasing departs from the three-tilt linear form (Sec. S11); with power-law couplings it is 0.02 ms. The order of the substitutions matters little because the first two steps are small.

Coupling reconstruction. The 51-ion couplings are reconstructed from three published simulated rows, $J_{10,j}$, $J_{26,j}$ and $J_{42,j}$ (Sec. S10; read as numbers from the source-data file `Fig1b.mat`). These reconstructions probe physical-model

sensitivity, distinct from the numerical convergence of TDVP for a given matrix (Sec. S11). The comparison has three parts (script `coupling_sensitivity.py`, Table S20): (i) the published rows scatter at a given distance by a relative standard deviation of 0.00–0.36 (0.03–0.13 for $d \leq 6$), so the chain is not translation invariant; (ii) the 8-exponential fit used by the TDVP matrix-product operator reproduces the profile within 6.7% for $d \leq 20$ and within 0.2% of J_0 in absolute terms everywhere (relative error up to 36% at $d = 38$, where J_{ij} is tiny); (iii) the power-law alternative used by Ref. [30]. Transport depends on the row-sum gradient B_i, and B_i is small and negative in the bulk: the MPO fit changes it there by up to $0.15J_0^2$, the inhomogeneous row-interpolated matrix by up to $0.80J_0^2$, and the power law by up to $1.53J_0^2$, nearly doubling it; S_i changes by at most 14%, and the end-ion B_i by 10–20%. The power law therefore brackets the inhomogeneous variant in B_i. Its TDVP crossings (H5) are later than the profile ones by 0.00 to 0.56 ms over 9 pairs (0.12, 0.04, 0.56 ms for the ordered pairs $0.5\pi/0.33\pi$, $0.5\pi/0.2\pi$, $0.33\pi/0.2\pi$ of Fig. 4; the crossing of 0.25π vs 0.2π moves beyond 5 ms). This spread measures sensitivity to the chosen reconstructions, not a calibrated uncertainty interval for the actual Hamiltonian. Bracketing the interpolated matrix in B_i does not establish bounds on its crossing times; the agreement of Eq. (9) with TDVP is a statement about the chosen reconstructed model, and both reconstructions give a comparable accuracy of rule P (Table S18). The 12-ion test H3 shows that $\pm 10\%$ random inhomogeneity leaves the accuracy of rule P unchanged.

TABLE S20. Row-sum coefficients of the 51-ion coupling variants (units of J_0^2, $J_0 = 216$ rad/s): S_i and B_i averaged over the ions of the five central blocks (16–35), the range of B_i there, and B_i at the two first ions of the chain.

variant	$\bar{S}_i$ (bulk)	$\bar{B}_i$ (bulk)	B_i range (bulk)	B_1, B_2
profile (used above)	4.12	−1.22	[−1.46, −0.99]	10.11, 6.27
profile, 8-exponential MPO fit	4.12	−1.24	[−1.41, −1.14]	10.07, 6.24
power law $J_0\lvert i-j\rvert^{-0.9}$	3.57	−2.32	[−2.52, −1.88]	12.24, 6.98
row-interpolated (inhomogeneous)	4.16	−1.59	[−1.93, −0.94]	9.59, 6.03

S13. PROTOCOLS FOR THE PREDICTED TESTS

(Q1) Prepare the tilted product state with a global rotation, evolve with the 51-ion XY Hamiltonian including the spin echo of Ref. [30], and apply local random unitaries to blocks of four ions [16, 44]; about 10^2 unitaries $\times$ 10^2 shots per time resolve the crossings, by comparison with the 12-ion experiment [14]. Simultaneously record $m_\perp$ of every ion for the three tilts, and the block ratio F_1/F_0 from the same randomized measurements. The asymmetry error should be $\sigma \lesssim 0.02$ to time the crossings involving 0.2π to 0.15–0.25 ms, and $\sigma \lesssim 0.01$ for the near-tangent $0.5\pi/0.33\pi$ pair (Sec. S11). The test of Eq. (9) needs no tomography: the block charge populations $p_q(t)$ from z-basis snapshots and, for every ion, $|\langle\sigma_i^+\rangle|$ and p_i for the three tilts. In the simulation, the per-tilt variant gives block-averaged crossings within 0.08 ms of TDVP, and the selected three-tilt slope-and-intercept form within about 0.20 ms; rules that ignore transport miss them by up to 0.8 ms (Table S17). Transport itself is visible in $p_i(t)$: at 0.2π the central ions gain and the ions near the ends lose charge, as in the 12-ion data [Fig. 3(a)]. (Q2) Repeat the azimuthal scans of Ref. [30] at two tilts and evaluate C_∞ as in Sec. S9; Eq. (S12) predicts the ratio $\sin^2\theta$ if the spin-wave admixture of C_∞ scales with the tilt in the same way (Sec. S8). (Q3) Measure ion i along an equatorial axis and all other ions along z in the same shot. Grouping shots by the measured $S_{\bar{i}}^z$ gives a conditional phase of ion i that should be linear in $S_{\bar{i}}^z$ with slope $-2\bar{J}t$. Conditioning removes the rotor part C_∞ of the phase variance; the site-resolved part, about $C_{ii} - C_\infty \approx 0.26$ at 3.3 ms [Fig. S2(c)], remains, so the conditional coherence is restored only partly, to about $e^{-(C_{ii}-C_\infty)/2}$ times the tilt-blind factor.

S14. DATA AND CODE AVAILABILITY

All inputs are public raw files (Zenodo 10390690 and 8124375); nothing was digitized from figures. The original archives are not redistributed; parsed copies of the 12-ion shots (CC-BY, Ref. [14]) are included as `qt/mp/raw_*.npz`. The reproducibility package keeps the working layout: `prl/` holds the manuscript, figure scripts, analysis scripts and the derived data behind every figure and table, and `qt/` holds the full pipelines (parsing, classical-shadow and sector estimators, fits, crossings, closure, DTWA, exact dynamics, low-density series, TDVP) with their helper

modules (`shadows.py`, `mono.py`, `dtwa.py`, `dtwa_fast.py`, `frlib.py`) and their small derived outputs. Scripts locate files through the environment variable `QME_ROOT`, the package root. Intermediate DTWA trajectory files larger than 5 MB are not included; the DTWA scripts regenerate them with fixed seeds. Position-resolved analysis: `ion_resolved.py`, `ion_jack.py`, `ion_theory.py`, `ion_predict.py`, `ion_stats.py`, `ion_profile.py` and `shorttime_law.py`, with outputs in `data/position`. Transport and dephasing: `normalized_law.py`, `envfactor.py`, `transport_only.py`, `transport12_exact.py`, `ion_P.py`, `ion_density.py`, `ion_norm_g.py`, `ion_transport.py` (`qt/mp`) and `transport51.py` (`qt/mps`); figure scripts `fig1_schematic.py`, `fig2_joshi.py`, `fig3_transport.py`, `fig4_prediction.py`. Earlier additions: `onemagnon.py`, `lowdens2.py` and `lowdens2_blockions.py` (Proposition 3 and the low-density series); `mps_xy_exp.py`, `mps_xy_exp_dt.py`, `mps_analysis.py`, `mps_pertilt.py`, `sector51.py`, `tech_dephasing.py`, `conv_check.py`, `conv_cross.py`, `conv_chi.py` and `tdvp_vs_exact12.py` (tensor-network simulations, analysis, convergence and the 12-ion benchmark), with outputs in `data/tdvp` and `data/lowdens`. The folder `qt/val` holds the validation: the frozen validation specification and its hash (`prl/validation_v008`), `heldout12.py` and `eval12.py` (sets H1–H3), `mps_xy_var.py`, `queue_tdvp.sh` and `eval51.py` (H4, H5), `threshold_checks.py` (one-axis-twisting and large-N_A thresholds), `field_check.py` (compensating fields), `coupling_sensitivity.py` (coupling reconstruction), `groupstats12.py` and `stats12.py` (joint resampling of the 12-ion tests) and `closure_joint.py` (closure test); `prl/scripts/analysis/make_validation_section.py` writes Sec. S12 from their outputs. The reviewer package includes `VERIFY_PACKAGE.py` and integrity manifests for checking the supplied files. The file `prl/TRACEABILITY.md` lists, for every figure and table, the generating command, its inputs and its outputs, and `prl/RUN.md` gives the environment and the order of execution.

[1] U. Grenander and G. Szegő, *Toeplitz Forms and Their Applications* (University of California Press, Berkeley, 1958).
[2] M.-D. Choi, Completely positive linear maps on complex matrices, Linear Algebra Appl. **10**, 285 (1975).
[3] M. A. Nielsen and I. L. Chuang, *Quantum Computation and Quantum Information*, 10th ed. (Cambridge University Press, Cambridge, England, 2010).
[4] L. J. Landau and R. F. Streater, On Birkhoff's theorem for doubly stochastic completely positive maps of matrix algebras, Linear Algebra Appl. **193**, 107 (1993).
[5] J. Helm and W. T. Strunz, Quantum decoherence of two qubits, Phys. Rev. A **80**, 042108 (2009).
[6] D. Crow and R. Joynt, Classical simulation of quantum dephasing and depolarizing noise, Phys. Rev. A **89**, 042123 (2014).
[7] C. O'Meara and R. Pereira, Self-dual maps and symmetric bistochastic matrices, Linear Multilinear Algebra **61**, 23 (2013).
[8] S. J. Harris, R. H. Levene, V. I. Paulsen, S. Plosker, and M. Rahaman, Schur multipliers and mixed unitary maps, J. Math. Phys. **59**, 112201 (2018).
[9] M. Kitagawa and M. Ueda, Squeezed spin states, Phys. Rev. A **47**, 5138 (1993).
[10] M. Foss-Feig, K. R. A. Hazzard, J. J. Bollinger, and A. M. Rey, Nonequilibrium dynamics of arbitrary-range Ising models with decoherence: An exact analytic solution, Phys. Rev. A **87**, 042101 (2013).
[11] G. Lindblad, On the generators of quantum dynamical semigroups, Commun. Math. Phys. **48**, 119 (1976).
[12] S. Yamashika and F. Ares, Quantum Mpemba effect in long-range spin systems, Phys. Rev. Lett. **136**, 090402 (2026).
[13] I.-S. Yang, The entanglement timescale, Phys. Rev. D **97**, 066008 (2018), arXiv:1707.05792 [hep-th].
[14] L. Kh. Joshi, J. Franke, A. Rath, F. Ares, S. Murciano, F. Kranzl, R. Blatt, P. Zoller, B. Vermersch, P. Calabrese, C. F. Roos, and M. K. Joshi, Observing the quantum Mpemba effect in quantum simulations, Phys. Rev. Lett. **133**, 010402 (2024).
[15] H.-Y. Huang, R. Kueng, and J. Preskill, Predicting many properties of a quantum system from very few measurements, Nat. Phys. **16**, 1050 (2020).
[16] A. Elben, S. T. Flammia, H.-Y. Huang, R. Kueng, J. Preskill, B. Vermersch, and P. Zoller, The randomized measurement toolbox, Nat. Rev. Phys. **5**, 9 (2023).
[17] T. Brydges, A. Elben, P. Jurcevic, B. Vermersch, C. Maier, B. P. Lanyon, P. Zoller, R. Blatt, and C. F. Roos, Probing Rényi entanglement entropy via randomized measurements, Science **364**, 260 (2019).
[18] R. Senese, J. H. Robertson, and F. H. L. Essler, Out-of-equilibrium full counting statistics in Gaussian theories of quantum magnets, SciPost Phys. **17**, 139 (2024).
[19] G. A. Paz-Silva, L. M. Norris, and L. Viola, Multiqubit spectroscopy of Gaussian quantum noise, Phys. Rev. A **95**, 022121 (2017).
[20] U. von Lüpke, F. Beaudoin, L. M. Norris, Y. Sung, R. Winik, J. Y. Qiu, M. Kjaergaard, D. Kim, J. Yoder, S. Gustavsson, L. Viola, and W. D. Oliver, Two-qubit spectroscopy of spatiotemporally correlated quantum noise in superconducting qubits, PRX Quantum **1**, 010305 (2020).
[21] P. Szańkowski, G. Ramon, J. Krzywda, D. Kwiatkowski, and Ł. Cywiński, Environmental noise spectroscopy with qubits subjected to dynamical decoupling, J. Phys.: Condens. Matter **29**, 333001 (2017).
[22] J. Baum, M. Munowitz, A. N. Garroway, and A. Pines, Multiple-quantum dynamics in solid state NMR, J. Chem. Phys. **83**, 2015 (1985).

[23] M. Gärttner, J. G. Bohnet, A. Safavi-Naini, M. L. Wall, J. J. Bollinger, and A. M. Rey, Measuring out-of-time-order correlations and multiple quantum spectra in a trapped-ion quantum magnet, Nat. Phys. **13**, 781 (2017).

[24] T. Monz, P. Schindler, J. T. Barreiro, M. Chwalla, D. Nigg, W. A. Coish, M. Harlander, W. Hänsel, M. Hennrich, and R. Blatt, 14-qubit entanglement: Creation and coherence, Phys. Rev. Lett. **106**, 130506 (2011).

[25] J. Kattemölle and J. van Wezel, Conditions for superdecoherence, Quantum **4**, 265 (2020).

[26] M. A. Perlin, C. Qu, and A. M. Rey, Spin squeezing with short-range spin-exchange interactions, Phys. Rev. Lett. **125**, 223401 (2020).

[27] T. Comparin, F. Mezzacapo, and T. Roscilde, Robust spin squeezing from the tower of states of U(1)-symmetric spin Hamiltonians, Phys. Rev. A **105**, 022625 (2022).

[28] T. Roscilde, T. Comparin, and F. Mezzacapo, Entangling dynamics from effective rotor–spin-wave separation in U(1)-symmetric quantum spin models, Phys. Rev. Lett. **131**, 160403 (2023).

[29] T. Roscilde, T. Comparin, and F. Mezzacapo, Rotor/spin-wave theory for quantum spin models with U(1) symmetry, Phys. Rev. B **108**, 155130 (2023).

[30] J. Franke, S. R. Muleady, R. Kaubruegger, F. Kranzl, R. Blatt, A. M. Rey, M. K. Joshi, and C. F. Roos, Quantum-enhanced sensing on optical transitions through finite-range interactions, Nature **621**, 740 (2023).

[31] J. Ma, X. Wang, C. P. Sun, and F. Nori, Quantum spin squeezing, Phys. Rep. **509**, 89 (2011).

[32] L. Pezzè, A. Smerzi, M. K. Oberthaler, R. Schmied, and P. Treutlein, Quantum metrology with nonclassical states of atomic ensembles, Rev. Mod. Phys. **90**, 035005 (2018).

[33] F. Kranzl, M. K. Joshi, C. Maier, T. Brydges, J. Franke, R. Blatt, and C. F. Roos, Controlling long ion strings for quantum simulation and precision measurements, Phys. Rev. A **105**, 052426 (2022).

[34] P. Hauke and L. Tagliacozzo, Spread of correlations in long-range interacting quantum systems, Phys. Rev. Lett. **111**, 207202 (2013).

[35] M. Foss-Feig, Z.-X. Gong, C. W. Clark, and A. V. Gorshkov, Nearly linear light cones in long-range interacting quantum systems, Phys. Rev. Lett. **114**, 157201 (2015).

[36] N. Defenu, T. Donner, T. Macrì, G. Pagano, S. Ruffo, and A. Trombettoni, Long-range interacting quantum systems, Rev. Mod. Phys. **95**, 035002 (2023).

[37] T. Comparin, F. Mezzacapo, and T. Roscilde, Multipartite entangled states in dipolar quantum simulators, Phys. Rev. Lett. **129**, 150503 (2022).

[38] A. Lerose and S. Pappalardi, Origin of the slow growth of entanglement entropy in long-range interacting spin systems, Phys. Rev. Res. **2**, 012041 (2020).

[39] D. J. Wineland, J. J. Bollinger, W. M. Itano, and D. J. Heinzen, Squeezed atomic states and projection noise in spectroscopy, Phys. Rev. A **50**, 67 (1994).

[40] J. Schachenmayer, A. Pikovski, and A. M. Rey, Many-body quantum spin dynamics with Monte Carlo trajectories on a discrete phase space, Phys. Rev. X **5**, 011022 (2015).

[41] A. Polkovnikov, Phase space representation of quantum dynamics, Ann. Phys. (N.Y.) **325**, 1790 (2010).

[42] J. Haegeman, C. Lubich, I. Oseledets, B. Vandereycken, and F. Verstraete, Unifying time evolution and optimization with matrix product states, Phys. Rev. B **94**, 165116 (2016).

[43] J. Hauschild and F. Pollmann, Efficient numerical simulations with tensor networks: Tensor network Python (TeNPy), SciPost Phys. Lect. Notes , 5 (2018).

[44] A. Rath, V. Vitale, S. Murciano, M. Votto, J. Dubail, R. Kueng, C. Branciard, P. Calabrese, and B. Vermersch, Entanglement barrier and its symmetry resolution: Theory and experimental observation, PRX Quantum **4**, 010318 (2023).